Numerical Modelling of Coupled Climate, Tectonics and Surface Processes on the Eastern Himalayan Syntaxis

Xueyun Lu[1], Jingtao Lai[2], Lining Wang[3], Jianqing Ji[1], and Dalai Zhong[4]

[1]Peking University
[2]Helmholtz Centre Potsdam GFZ German Research Centre for Geosciences
[3]Researth Institute of Petroleum Exploration & Development, PetroChina
[4]Institute of Geology and Geophysics, Chinese Academy of Sciences

December 10, 2023

Abstract

The interactions between climate, tectonics and surface processes have become a research hotspot in Earth science in recent years. Although various insights have been achieved, the relative importance of climatic and tectonic forcing in influencing the evolution of mountain belts still remains controversial. In order to investigate the tectonic and topographic evolution, as well as the formation mechanism of the eastern Himalayan syntaxis, we developed a comprehensive 2D climatic-geomorphological-thermomechanical numerical model and conducted over 200 experiments to test the influences of convergence rate, average precipitation and initial geothermal gradient on orogenic wedge. The results indicate that, for a specific orogenic wedge, its tectonic and topographic evolution primarily relies on the relative strength of tectonic and climatic forces, rather than their respective magnitudes. A syntaxis is the result of the combined effects of tectonic forces, climatic forces and geothermal field. In mountain belts, once the convergence rate and average precipitation fall within a Type D zone determined by the crustal thermal structure, a sustained, stationary, localized and relatively rapid erosion process will be established on the windward flank of the orogenic wedge. This will further induce sustained and rapid uplift of rocks, exhumation and deformation, ultimately forming a syntaxis. In this context, syntaxis is the inevitable system's outcome under various physical laws, including conservation of mass, momentum and energy, rheology, orographic precipitation, surface processes, etc. Orogens are best viewed as complex open systems controlled by multiple factors, none of which can be considered as the sole cause of the system's outcome.

Numerical Modelling of Coupled Climate, Tectonics and Surface Processes on the Eastern Himalayan Syntaxis

Xueyun Lu[1], Jingtao Lai[2], Lining Wang[3,4], Jianqing Ji[1], Dalai Zhong[5]

[1]Key Laboratory of Orogenic Belts and Crustal Evolution, School of Earth and Space Sciences, Peking University, Beijing 100871, China

[2]Earth Surface Process Modelling, GFZ German Research Centre for Geosciences, 14473 Potsdam, Germany

[3]Research Institute of Petroleum Exploration & Development, PetroChina, Beijing 100083, China

[4]Key Laboratory of Basin Structure & Hydrocarbon Accumulation, CNPC, Beijing 100083, China

[5]Institute of Geology and Geophysics, Chinese Academy of Sciences, Beijing 100029, China

Corresponding author: Jianqing Ji (grsange@pku.edu.cn)

Key Points:

- A climatic-geomorphological-thermomechanical modelling technique is developed to investigate the evolution of orogenic wedges.
- The evolution of a specific orogenic wedge primarily relies on the relative strength of tectonic and climatic forces.
- The formation of the eastern Himalayan syntaxis results from the cooperation of tectonic forces, climatic forces and geothermal field.

Abstract

The interactions between climate, tectonics and surface processes have become a research hotspot in Earth science in recent years. Although various insights have been achieved, the relative importance of climatic and tectonic forcing in influencing the evolution of mountain belts still remains controversial. In order to investigate the tectonic and topographic evolution, as well as the formation mechanism of the eastern Himalayan syntaxis, we developed a comprehensive 2D climatic-geomorphological-thermomechanical numerical model and conducted over 200 experiments to test the influences of convergence rate, average precipitation and initial geothermal gradient on orogenic wedge. The results indicate that, for a specific orogenic wedge, its tectonic and topographic evolution primarily relies on the relative strength of tectonic and climatic forces, rather than their respective magnitudes. A syntaxis is the result of the combined effects of tectonic forces, climatic forces and geothermal field. In mountain belts, once the convergence rate and average precipitation fall within a Type D zone determined by the crustal thermal structure, a sustained, stationary, localized and relatively rapid erosion process will be established on the windward flank of the orogenic wedge. This will further induce sustained and rapid uplift of rocks, exhumation and deformation, ultimately forming a syntaxis. In this context, syntaxis is the inevitable system's outcome under various physical laws, including conservation of mass, momentum and energy, rheology, orographic precipitation, surface processes, etc. Orogens are best viewed as complex open systems controlled by multiple factors, none of which can be considered as the sole cause of the system's outcome.

Plain Language Summary

The eastern Himalayan syntaxis is essentially a large-scale antiform, where extreme relief, deep exhumation, intense deformation, and a steepening near-surface thermal gradient coincide in core areas. Despite its significance, the formation mechanism of this antiform still remains controversial. To investigate its formation mechanism, we developed a numerical model that integrates rock deformation processes, surface processes, and topography-dependent precipitation. We designed and conducted numerical experiments to investigate the influences of convergence rate, average precipitation and initial geothermal gradient on the evolution of an orogenic wedge. The results show that the tectonic and topographic evolution of an orogenic wedge, as well as the formation of the eastern Himalayan syntaxis, is the result of cooperation of tectonic compression, precipitation and geothermal field.

1 Introduction

The topography of collisional mountain ranges is controlled by both tectonics and climate: crustal thickening generates topography, while climate modulates surface processes and lowers mountain heights (Champagnac et al., 2012; Champagnac et al., 2014; Molnar, 2003; Molnar & England, 1990; Valla et al., 2021; Whipple, 2009; Willett, 2006). Much effort has been made to understand the mechanisms of the interactions between climate, tectonics and surface processes through various methods, including analytical treatment (Dahlen, 1990; Dahlen et al., 1988; Hilley et al., 2004; Roe et al., 2006; Roe et al., 2008; Tomkin & Roe, 2007; Whipple & Meade, 2006), numerical modelling (Avouac & Burov, 1996; Bahadori et al., 2022; Beaumont et al., 2001; Beaumont et al., 2004; Cruz et al., 2010; Koons et al., 2002; Simpson, 2004; Stolar et al., 2006; Willett, 1999; Wolf et al., 2022)and field observation (Berger et al., 2008; Clift et al., 2020; Gong et al., 2015; Grujic et al., 2006; Molnar & England, 1990; Norton & Schlunegger, 2011; Peizhen et al., 2001; Reiners et al., 2003; Steer et al., 2014; Tu et al., 2015; Willett et al., 2006; Ye et al., 2022; Zeitler, Koons, et al., 2001; Zeitler et al., 2014), and many important insights have been achieved (e.g.,NASEM, 2020; Whipple, 2009). For instance, previous researchers have found that the width and relief of a steady-state critical wedge are quantitatively related to precipitation and accretionary flux (Roe et al., 2006; Tomkin & Roe, 2007). Surface processes can influence the tectonic evolution of mountain belts by altering the distribution of mass on the surface and influencing gravitational stresses (Willett, 2006). Numerical modelling studies have demonstrated that erosion can promote localized crustal shortening and contribute to mountain growth (Avouac & Burov, 1996). Additionally, asymmetric rainfall intensity and erosional efficiency can lead to asymmetric development of the topography, deformation and exhumation (Willett, 1999). In the case of large, hot orogens like the Himalayan-Tibetan system, rapid erosion along the plateau margin can facilitate the extrusion of low-viscosity material from beneath the plateau (Beaumont et al., 2001).However, the relative importance of climatic and tectonic forcings in influencing the evolution of mountain belts is still debated (Burbank et al., 2003; Dadson et al., 2003; Herman et al., 2013; King et al., 2016; Molnar, 2003, 2009; Molnar & England, 1990; Pinter & Brandon, 1997; Raymo & Ruddiman, 1992; Wang et al., 2014; Whipple, 2009, 2014; Zeitler et al., 2014).

In the eastern Himalayan syntaxis, the intense tectonism, heavy precipitation, and ultra-fast surface processes make it an ideal natural laboratory for investigating the interactions among tectonics, climate, and surface processes (Bracciali et al., 2016; Gong et al., 2015; Tu et al., 2015; Yu et al., 2011). On the whole, the eastern Himalayan syntaxis is a large-scale antiform, in the core areas of which, extreme relief, deep exhumation, intense deformation and steepening of the near-surface thermal gradient overlap spatially (Burg et al., 1998; Butler, 2019; Koons et al., 2013; Zeitler et al., 2014). Various models have been proposed to illustrate its formation mechanism and structural evolution (Butler et al., 2002; Ding et al., 2001; Koons, 1995; Mukhopadhyay et al., 2011; Whipp Jr et al., 2014; Zeitler, Koons, et al., 2001). Classical models include northward indentation of Indian plate (Ding et al., 2001; Koons, 1995; Zhang et al., 2004), crustal and lithospheric scale folding under continental shortening (Burg et al., 1998; Burg & Podladchikov, 1999; Burg et al., 1997) and tectonic aneurysm (Koons et al., 2013; Zeitler, Koons, et al., 2001; Zeitler, Meltzer, et al., 2001). Concretely, the indentation model posits that syntaxis results from the northward indentation of the Indian continental indenter, while the crustal and lithospheric scale folding model believes that the large-scale antiform arises from lithospheric buckling, which is considered as a basic response to large-scale continental shortening. The tectonic aneurysm model attributes the development of the syntaxis to the positive feedbacks among erosion, heat advection, rock strength, and deformation. These models focus on different factors. For instance, the indentation model highlights the influences of plate geometry and rock strength, while the crustal and lithospheric scale folding model emphasizes the role of tectonic forces. The tectonic aneurysm model assigns a crucial role to climate and surface processes. Nevertheless, extensive research has demonstrated that climatic forces, tectonic forces and rock strength (crustal thermal structure) all play crucial roles in influencing the evolution of an orogenic wedge (Avouac & Burov, 1996; Beaumont et al., 2001; Buiter, 2012; Royden et al., 2008; Ruh et al., 2012; Tapponnier et al., 2001; Vogt et al., 2017; Vogt et al., 2018; Willett, 1999) , and their respective roles (regardless of magnitude) persist throughout the whole course of orogenesis. When evaluating the impact of one specific factor, it is essential to consider the other relevant factors as preconditions or assumptions. These models have different preconditions and assumptions, making comparison and testing among them challenging. Thus, further quantitative research on the feedback mechanisms and the relative importance of climate and tectonics is required.

To quantitatively investigate the interactions between climate, tectonics and surface processes, as well as the formation conditions and mechanisms of the eastern Himalayan syntaxis, we developed a comprehensive 2D climatic-geomorphological-thermomechanical numerical model and conducted a set of experiments to investigate the evolution of orogenic wedges under varying climatic, tectonic and geothermal conditions. Our results indicate that the formation of the eastern Himalayan syntaxis is the consequence of the combined effects of climatic forcing, tectonic forcing and crustal thermal structure (or rock strength).

2 Background

Located at the eastern end of Himalayan arc, the eastern Himalayan syntaxis is part of the Himalayan orogenic belt and essentially a special orogenic wedge (Yin, 2006). Compared to the central Himalayan arc, the eastern Himalayan syntaxis exhibits the following characteristics: (1)The overall structure exhibits a large-scale antiform (Burg et al., 1998; Burg et al., 1997). (2)A broad upwarp of the Moho beneath the Namche Barwa, with the crustal thickness in the core area of the syntaxis (55 km) appearing notably lower than the regional background crustal thickness (~70 km) (Zeitler et al., 2014). (3) Steep thermal gradients in upper crust (>50 ℃/km) (Craw et al., 2005). (4) Strong "bull's-eye" spatial localization of deformation (< ~50 km in diameter) (Bendick & Ehlers, 2014; Koons et al., 2013). (5) The thermochronological ages generally become younger with proximity to the Namche Barwa Peak (NBP), the core area of the syntaxis (Gong et al., 2015; King et al., 2016; Tu et al., 2015). (6) Rapid exhumation rate (>5 mm/yr)(Burg et al., 1997; Enkelmann et al., 2011; King et al., 2016; Stewart et al., 2008). (7) Extreme relief, intense climate and surface processes overlap in local area within the orogenic belt (Bookhagen & Burbank, 2006; Koons et al., 2013; Yu et al., 2017). Although the collision of India with Asia has been widely acknowledged to have occurred over 50 million years ago, many of the significant structures associated with the formation of the eastern Himalayan syntaxis only formed within the past 10 Myr (Butler, 2019; Zeitler et al., 2014).

2.1 Geological setting

The eastern Himalayan syntaxis is Cored by the Namche Barwa-Gyala Peri massif (NBGPM) and surrounded by the Lhasa terrane to the east, north, and west (Figure 1). In this region, the Lhasa terrane is mainly composed of high-grade metamorphic rocks, Cambrian–Eocene unmetamorphosed strata and numerous plutons (Gangdese granites) (Zhang et al., 2010). The core metamorphic massif primarily consists of meta-sedimentary greenschist-facies schists and amphibolite- to granulite-facies gneisses. These include garnet biotite schist, biotite epidote schist, sillimanite garnet biotite gneiss, biotite hornblende plagioclase gneiss, and biotite plagioclase amphibolites (Tu et al., 2015). High-pressure granulite-facies metamorphic rocks are predominantly exposed in the core area of the syntaxis, particularly near NBP (Booth et al., 2009; Ding et al., 2001; Liu & Zhong, 1997; Tu et al., 2015). According to Booth et al. (2009)'s study, the peak metamorphic pressures and temperatures within the core of the massif are estimated to be 10~14 kbar and 700~900 °C, respectively. Meanwhile, abundant young granitoids distribute in the region with the youngest age of only 0.9 Ma being reported (Zeitler et al., 2014). Geochemical analysis suggests that these young granites within the core of the massif predominantly originate from rapid depression melting of parent rocks (Booth et al., 2004; Koons et al., 2013).

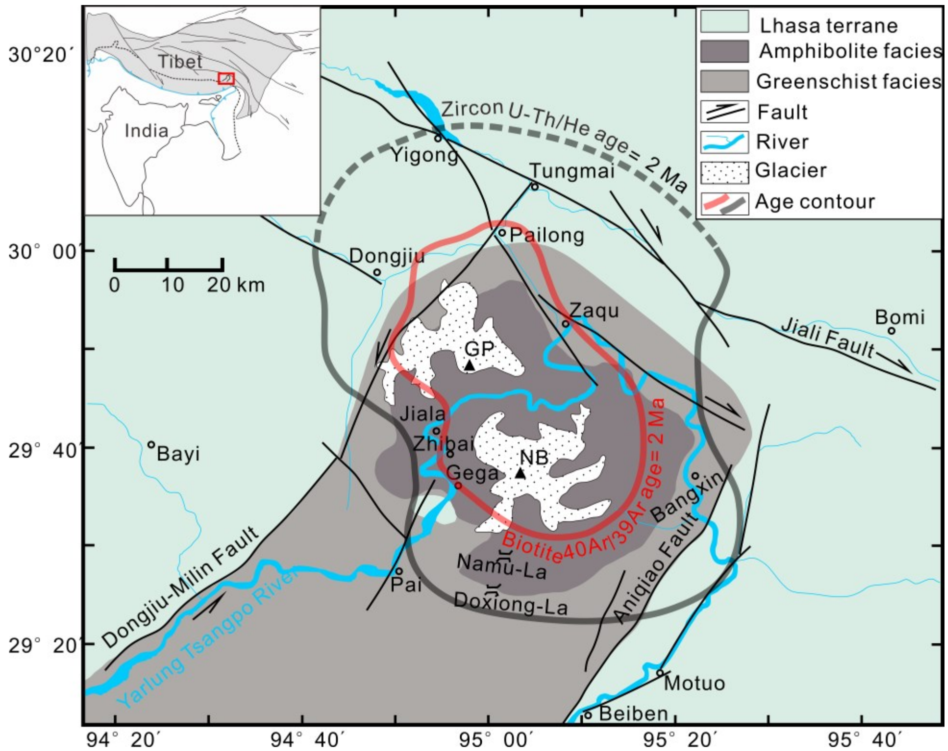

Figure 1. Geological sketch of the eastern Himalayan syntaxis showing the main geological units and structures (after Tu et al. (2015)). The inset in the top left corner illustrates the location of the eastern Himalayan syntaxis within the Himalayan-Tibetan orogenic belt. The bold black and red lines outline the areas with previously published young (<2 Ma) zircon U-Th/He and biotite 40Ar/39Ar ages, respectively (after Stewart et al. (2008)).

The overall structure of the eastern Himalayan syntaxis is a large NE-trending and N-plunging antiform (30 to 40 km wide), with its hinge lying near Doxiong-La (Burg et al., 1998; Burg et al., 1997; Ding et al., 2001). To the west of the syntaxis, the left-slip NE-trending Donjiu–Milin ductile fault zone defines its western boundary (Zhang et al., 2004), while the dip-slip NE-trending ductile Aniqiao fault zone is considered as its eastern bounding structure. To the north of the syntaxis lies the nearly E–W-trending Jiali ductile shear zone. The structural data suggests that this zone underwent a kinematic shift from left-slip to right-slip during its movement history (Lin et al., 2009). There are also a series of 290° - trending right-slip thrust fault zones and NE(or NW)-trending high-angle brittle normal faults in the syntaxis (Tu et al., 2015; Zhang et al., 2004).

2.2 Climate and geomorphology

Present climate data shows that the precipitation in the Tibetan Plateau is concentrated along the southern Himalayan topographic front, while the two ends of the Himalayan arc receive the highest amount of precipitation (Bookhagen & Burbank, 2006). According to the rainfall amounts estimated from TRMM (Tropical Rainfall Measurement Mission) satellite data, the annual average precipitation in the eastern Himalayan syntaxis region is currently around 2 m/yr, with maximum rainfall reaching up to 6 m/yr (Anders et al., 2006; Bookhagen & Burbank, 2006). In addition, the NBP and GPP (Gyala Peri Peak) are covered by massive modern glaciers, with the equilibrium line altitudes (ELAs) ranging between 4400 and 4500 m (Yao et al., 2010). The presence of abundant moraine deposits and outwash (with thickness ranging from 100 m to over 200 m) discovered at altitudes of 2900 to 4800 m at the foot of NBP also suggests that the eastern Himalayan syntaxis region has been subjected to significant glacial activities since Quaternary (Song et al., 2012).

The Yarlung Tsangpo River, the largest river in southern Tibet, flows parallel to the Himalayan orogenic belt for ~1700 km before entering the eastern Himalayan syntaxis, where it suddenly becomes narrow and deeply entrenched, creating one of the most spectacular gorges on the planet, the Yarlung Tsangpo Canyon. At the syntaxis, the river undergoes a rapid turn of ~180°, giving rise to a topographic relief of nearly 5 km within a horizontal distance of ~12 km. Then it flows southward, leaving the syntaxis (Finnegan et al., 2008; Yang et al., 2018). Under the influences of intense climate and tectonism, the eastern Himalayan syntaxis has developed distinct geomorphic features, including extreme local relief of over 4 km, steep topographic slopes and towering peak elevations that extend well above the ELA (Koons et al., 2013).

2.3 Thermochronology

The thermochronological ages in the eastern Himalayan syntaxis are relatively young (King et al., 2016). In this region, the published biotite 40Ar/39Ar are basically younger than 8 Ma (Gong et al., 2015; Stewart et al., 2008; Yu et al., 2011; Zhang et al., 2004). In the center of the metamorphic massif, some of the biotite 40Ar/39Ar ages can be as low as 0.2 and 0.4 Ma (Zeitler et al., 2014). The reported zircon fission track ages, zircon U-Th/He ages and apatite fission track ages are generally younger than 3 Ma (Burg et al., 1998; Stewart et al., 2008; Tu et al., 2015; Yu et al., 2011), while the youngest zircon fission track age and zircon U-Th/He age can be as low as 0.2 Ma and 0.2~0.3 Ma, respectively (Seward & Burg, 2008; Zeitler et al., 2014). In contrast, the thermochronological ages of the surrounding Lhasa terrane are relatively older (Gong et al., 2015; Zeitler et al., 2014). On the whole, the four types of thermochronological data mentioned above show a gradual decrease in age as they approach the core area of the syntaxis (Figure 1). All these data suggest rapid exhumation rates in this region. According to the P-T estimates , U-Pb and Th-Pb dating of metamorphic and anatectic phases, it is inferred that the long-term (since 5~10 Ma) exhumation rate in the core area of the syntaxis could reach 4~6 mm/yr or more, with total exhumation exceeding 20 km (Koons et al., 2013). Enkelmann et al. (2011) also reported decadal erosion rates of 5~17 mm/yr in the region based on the study of detrital zircon from the Brahmaputra River and tributaries.

3 Methodology

In this study, we use a coupled 2D climatic-geomorphological-thermomechanical modelling technique to simulate the crustal deformation, geothermal evolution, partial melting, fluvial erosion, sediment deposition, hillslope, and orographic precipitation in a compressional system.

3.1 Tectonic processes

In the thermomechanical model, the following continuity equation and stokes equation are employed to approximate the conservation of mass and momentum for 2D incompressible material in the gravitational field. The geothermal evolution of the system is modelled by solving the energy equations, which account for radioactive, shear, adiabatic and latent heat production.

Incompressible continuity equation:

$$\frac{\partial v_x}{\partial x} + \frac{\partial v_y}{\partial y} = 0 \quad (1)$$

where v_x and v_y are horizontal and vertical velocity components, respectively.

2D stokes equation:

$$\frac{\partial \sigma'_{ij}}{\partial x_j} - \frac{\partial P}{\partial x_i} + \rho(C, P, T, M) g_i = 0 \quad (2)$$

where i and j are coordinate indexes, x_j and x_i are spatial coordinates, σ'_{ij} is the deviatoric stress tensor, g_i is the ith component of the gravity vector, ρ is the density, which depends on the composition (C), pressure (P), temperature (T) and melt fraction (M).

Energy equations:

$$\rho C_p \frac{DT}{Dt} = -\frac{\partial q_i}{\partial x_i} + H_r + H_s + H_a + H_L \quad (3)$$

$$q_i = -k(C, T) \frac{\partial T}{\partial x_i} \quad (4)$$

$$H_a = T\alpha \frac{DP}{Dt} \quad (5)$$

$$H_s = \frac{{\sigma'_{xx}}^2}{\eta_{vp}} + \frac{{\sigma'_{xy}}^2}{\eta_{vp}} \quad (6)$$

where C_p is the effective isobaric heat capacity, $\frac{DT}{Dt}$ is the substantive time derivative of temperature, q_i is the heat flux components, H_r, H_s, H_a and $H_L$are the radioactive, shear, adiabatic and latent heat production, respectively. $k(C, T)$ is the composition- and temperature-dependent thermal conductivity, $\frac{DP}{Dt}$ is the substantive time derivative of pressure, α is the thermal expansion, η_{vp} is the effective visco-plastic viscosity. For details regarding the visco-elasto-plastic rheology of rocks, the partial melting model, and the material properties used in this study, readers are referred to Texts S1, S2, and Table S1 in Supporting Information S1.

3.2 Surface processes

Considering the code accessibility, feasibility and brevity, a landscape evolution model that accounts for the stream-power law (SPL) fluvial erosion, sediment deposition, hillslope, tectonic horizontal advection and vertical uplift is adopted (Barnhart et al., 2019; Culling, 1963; Davy & Lague, 2009):

$$\frac{\partial h}{\partial t} = \frac{VQ_s}{Q} - KQ^m S^n + K_s \nabla^2 h - \boldsymbol{v} \cdot \nabla h \quad (7)$$

where h is the topographic elevation, t is time, K_s is the 'topography diffusion' coefficient, K is the erodibility, m and n are the discharge and slope exponents, respectively. V is the effective settling velocity of the sediment particles, $\boldsymbol{v}$ is the material velocity vector at the surface. Q is volumetric water discharge, Q_s is volumetric sediment discharge. The volumetric sediment discharge at a specific downstream point ($Q_{s,out}$) is determined by integrating all the erosion minus deposition that has occurred upstream (Barnhart et al., 2019):

$$Q_{s,out} = \int_A \left([KQ^m S^n]_s - \left[\frac{VQ_{s,in}}{Q}\right]_s \right) dA \quad (8)$$

Here, the water discharge is calculated based on the orographic precipitation. It has been recognized that topography has a profound effect on the spatial patterns of precipitation (Roe, 2005; Roe et al., 2002; Smith & Barstad, 2004). Mountains can influence the flow of air and disturb the vertical stratification of the atmosphere by acting as physical barriers and sources or sinks of heat, thereby influencing the patterns of precipitation (Barros & Lettenmaier, 1994). At the space scale of mountain ranges (tens to hundreds of kilometers) and in the climatological average, the windward flank of the mountain range receives significantly higher precipitation compared to the leeward flank, forming the well-known rain shadow. Such precipitation localization effect is well observed in mountain ranges in today's climate across a wide range of latitudes, such as Southern Alps of New Zealand (Wratt et al., 2000), Himalayas (Bookhagen & Burbank, 2006; Burbank et al., 2003), Cascades mountains of Washington (Reiners et al., 2003) and St Elias Range of Alaska (Berger & Spotila, 2008). Here, following Anders et al. (2006)'s study, we assume that the precipitation in Himalayas is proportional to two factors. One is saturation vapor pressure at the surface, and the other is the saturation vapor pressure multiplied by the slope of the topography in the direction of the prevailing wind:

$$P = (\alpha_P + \beta_P S)e_{sat}(T) \quad (9)$$

where P is precipitation, α_P and β_P are constants, S is the topographic slope in the direction of the prevailing wind. $e_{sat}(T)$ is the saturation vapor pressure, and it can be estimated by the Clausius-Clapeyron relation (Emanuel, 1994):

$$e_{sat}(T) = 6.112 \exp\left(\frac{aT}{b+T}\right) \quad (10)$$

where $a = 17.67$, $b = 243.5$℃, T is the air temperature in degrees Celsius, and it is calculated using an average temperature at sea level (T_0, assumed to be 30℃) and a constant air temperature lapse rate (Γ, assumed to be -7 ℃/km), expressed as $T = T_0 + \Gamma h$.

Although its simplicity, this model captures the significant features of the pattern of the precipitation in Himalayas (Anders et al., 2006), and it's easy to implement and couple with landscape evolution models and thermomechanical models. According to the regression analysis by Anders et al. (2006), the values of α_P and β_P are approximately within the range of 0 to 1, and they are region-specific and scale-dependent, which indicates that there is no single set of values should be generally applicable. For details regarding the selection of these two parameters, readers are referred to Text S3 and Figure S1 in Supporting Information S1.

3.3 Numerical model design

The initial model domain extends 31 km in the Y direction and varies from 600 to 1000 km in the X direction depending on the total shortening amount (Figure 2a). To simulate the topographic evolution, the top 20 km of the model domain is set as "sticky air" layer with viscosity of 10^{18} $Pa\ s$ and density of 1 kg/m^3 (Crameri et al., 2012; Schmeling et al., 2008). Beneath the "sticky air" layer, the rightmost 100 km is set as a relatively rigid backstop, while the left part is composed of 11-km-thick undeformed visco-elasto-plastic rock sequence. Referring to the seismic reflection profile across Himalayas (Schulte-Pelkum et al., 2005) and some general profiles of fold-and-thrust belts or accretionary wedges on the planet (Buiter, 2012; Ruh et al., 2012), we assume that the initial thickness of the normal undeformed rock sequence is 10 km. Beneath this rock sequence, a 1-km-thick decollement layer is introduced to mimic the main decollement at the base of Himalayan orogenic wedge. This decollement layer is assumed to be frictional and has smaller compressive strength and internal friction coefficient compared to the normal rock sequence so that it's prone to plastic deformation (Ruh et al., 2012)(see material properties in Table S1 in Supporting Information S1). The model is solved by 401×81 non-uniform Eulerian nodes, with the finest initial resolution of 1 km×0.39 km in the proximity of the convergence center, and 8 million randomly distributed Lagrangian markers.

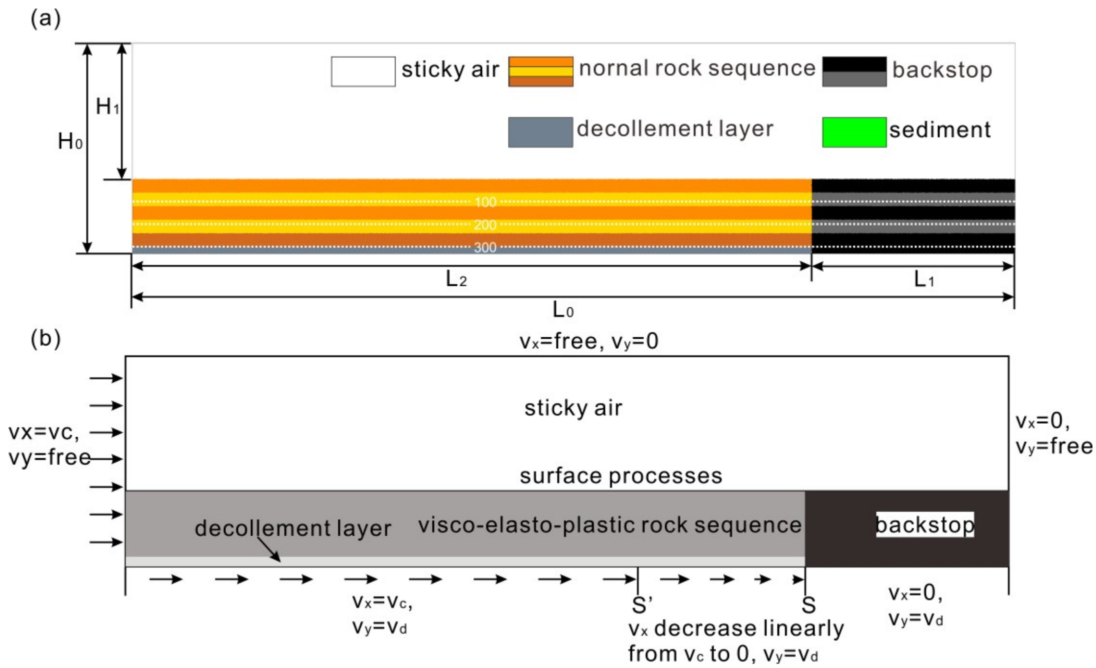

Figure 2. Model setup. (a) Initial model configuration. The definitions of each parameter can be found in Table 1. Different colors represent different rock types,with:white—sticky air; orange, yellow and brown—normal rock sequence; slategrey—decollement layer; grey and black—backstop; green—sediment. The sediment is not shown in Figure 3a, but will appear during the evolution of the model. The white dashed lines indicate isotherms (in °C). (b) Boundary conditions. v_c represents the convergence rate, and v_d is defined in the main text.

To simulate the mechanical environment at convergent plate boundary, a horizontal convergence velocity v_c (towards the right) is applied on the left boundary and the left portion of the lower boundary (Figure 2b), while the horizontal velocity on the right boundary and the right portion (right side of point S in Figure 2b) of the lower boundary is fixed at zero. To prevent abrupt velocity change, the horizontal velocity between S and S' at the lower boundary is assumed to decrease linearly from the convergence rate v_c to zero. In order to ensure mass conservation in the computational model, a vertical outward velocity $v_d = H * v_c/L$, which changes at every time step, is prescribed along the lower boundary. Here, H and L are the current height and width of the model, respectively. The upper boundary is free slip. All the experiments presented here share the same boundary conditions.

The thermal boundary conditions are 0 °C at the upper boundary and zero heat flux across the vertical boundaries. The temperature of the "sticky air" is consistent with temperature at the upper boundary. The temperature gradient at the lower boundary is fixed at the initial geothermal gradient dT/dh in order to ensure a relatively stable inward heat flux. The initial geothermal field is assumed to increase linearly from 0 °C at the surface to a specific bottom temperature, which varies depending on the initial geothermal gradient.

Table 1. Parameters used in the numerical experiments

Parameter	Description	Value
H_0	Height of the initial setup (km)	31
H_1	Thickness of the air (km)	20
L0	Initial length of the model (km)	600~1000
L_1	Length of backstop (km)	100
L_2	Length of rock sequence (km)	500~900
T_{top}	Temperature at model top (°C)	0
dT/dh	Initial thermal gradient (°C/km)	10~45 [a]
P_0	The average annual precipitation (m/yr)	0~20
v_c	Convergence rate (cm/yr)	0.5~5.0
T_0	Temperature at sea level in the model of orographic precipitation (°C)	30
Γ	The constant lapse rate in the model of orographic precipitation (°C/km)	-7.0
β_P	The coefficient in the model of orographic precipitation	0.370
V	effective settling velocity of the sediment particles (m/yr)	1.0 [b]
K	the erodibility in the stream-power incision model ($m^{-0.5}yr^{-0.5}$)	$2*10^{-5}$ [c]
m	The discharge exponent in the stream-power incision model	0.5 [c]
n	The slope exponent in the stream-power incision model	1.0 [c]
Ks	the 'topography diffusion' coefficient (m^2/yr)	0.035 [d]

Note. [a] Parameters from (Turcotte & Schubert, 2014). [b] Parameters from Yuan et al. (2019). [c] Parameters from Whipple and Tucker (1999). [d] Parameters from Fernandes and Dietrich (1997)

Given that many of the significant structures linked to the development of the eastern Himalayan syntaxis are younger than 10 Ma, we focus our research on the most recent 7 Myr, rather than the entire evolutionary history of the Himalayan-Tibetan orogenic belt since the onset of collision. The total model runtime is set to 8 Myr. The precipitation for the first 1 Myr is set to 0 m/yr to achieve a model state with a certain degree of deformation and relief. The orographic precipitation is applied after t=1 Myr, and for all the experiments, it's assumed that the direction of the prevailing winds is consistent with the direction of the subduction, which is from the left. By varying the convergence rate v_c, average precipitation P_0, and initial geothermal gradient dT/dh, which is related to the overall strength of the shallow crustal rock sequence, a total of 232 experiments are designed and conducted (Table S2, S3, and S4 in Supporting Information S1).

3.3 Numerical implementation

The thermomechanical processes are solved using the code provided by Gerya (2019), which uses a finite difference approach and a marker in cell technique to solve the thermal and mechanical equations mentioned above. The surface processes and orographic precipitation are implemented through landlab, an open-source package for numerical modelling of Earth surface dynamics (Barnhart et al., 2019; Barnhart et al., 2020; Hobley et al., 2017), and Python programming. We use a 3-by-N regular landlab grid with top and bottom edges as fixed zero gradient boundaries to simulate the evolution of a 1D model domain. We couple the thermomechanical model, surface processes model, and orographic precipitation model through the following steps. Firstly, the thermomechanical processes are solved using the finite difference code. This provides the current topography, which is then used to simulate the precipitation based on the orographic precipitation model. Subsequently, the surface processes are solved based on the topography and precipitation with smaller sub-time steps in landlab, after which the elevation changes due to surface processes can be determined. Based on these elevation changes and the thermomechanical velocity field, the topography in the model is updated. At the same time, if the rock types of the Lagrangian markers near the surface has changed, the corresponding field quantities are also updated. This process is repeated until the computation reaches the predetermined end time.

4 Results

4.1 Relative importance of tectonic and climatic forcings in controlling the evolution of orogenic wedge

The modelling results indicate that the convergence rate, average precipitation and initial geothermal gradient all have significant influences on the structural and geomorphic evolution of the orogenic wedge. For all the models depicted in Figure 3 and 4, the initial geothermal gradients are consistently set at 30 °C/km. When increasing the convergence rate and maintaining a constant average precipitation, it leads to an increase in the width and height of the orogenic wedge (Figure 3). Additionally, at relatively lower convergence rates, the orogenic wedge tends to develop folds or fault-related folds (Figure 3b), and for those models with sufficiently low convergence rates, the deformation structures and topography will be unable to withstand intense erosion and thus cannot be completely preserved (Figure 3a). As the convergence rate increases, the deformation style within the orogenic wedge gradually transitions to thrust faults, and the deformation continuously extends towards the foreland basin through developing imbricate structures (Figure 3c and d).

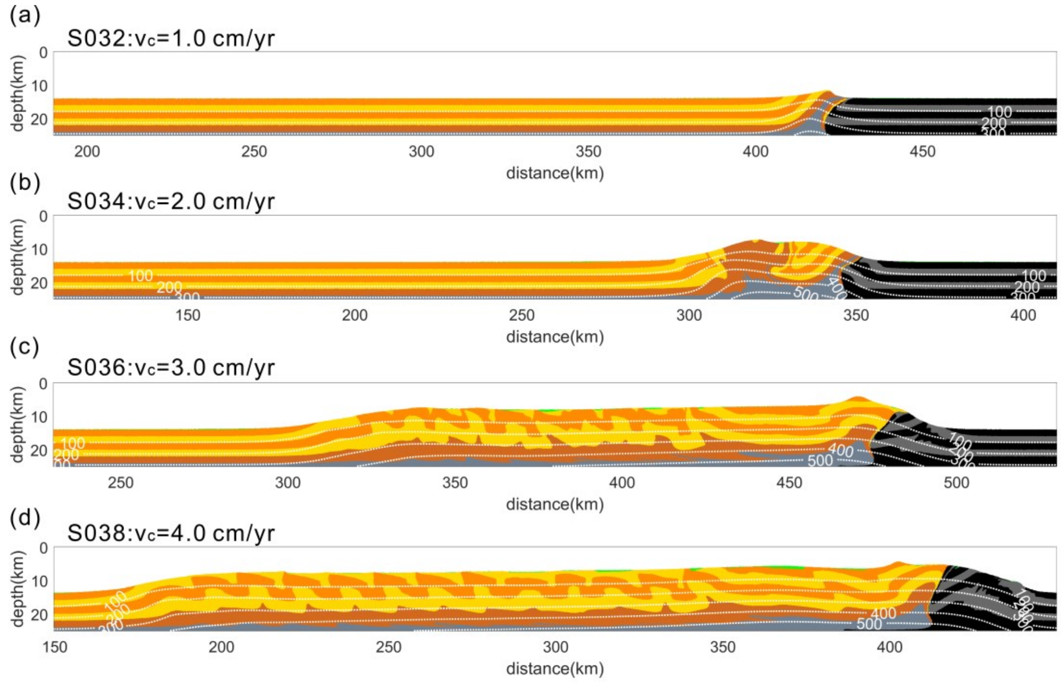

Figure 3. Numerical modelling results showing the influence of convergence rate(v_c) on the evolution of orogenic wedges. The white dashed lines indicate isotherms (in °C). For all models, the average precipitation(P_0) is 6 m/yr, the initial geothermal gradient(dT/dh) is 30 °C/km, and the runtime is 8 Myr. The convergence rates for (a), (b), (c) and (d) are 1.0 cm/yr, 2.0 cm/yr, 3.0 cm/yr and 4.0 cm/yr, respectively. The width and height of the orogenic wedge increase as the convergence rate increases, while keeping the average precipitation constant. At the same time, the rock deformation exhibits the tendency from folding toward imbricate thrusting.

The effect of increasing the average precipitation while fixing the convergence rate is opposite to that of increasing the convergence rate while keeping the average precipitation constant. When the convergence rate and initial geothermal gradient remain constant, increasing the average precipitation favors reducing the height and width of the orogenic wedge (Figure 4). At the same time, the deformation style within the orogenic wedge gradually transitions from thrusting to folding. Similarly, for models with sufficiently high average precipitation, the deformation structures will be quickly eroded, resulting in very low topography (Figure 4d and e). These findings suggest that the height, width, and deformation style of a specific orogenic wedge primarily rely on the relative strength of tectonic and climatic forces, rather than their respective magnitudes. When the tectonic forces are relatively stronger, the orogenic wedge tends to broaden, increase in elevation, and develop thrust faults. Conversely, when the tectonic forces are relatively weaker, the orogenic wedge tends to narrow, decrease in elevation, and develop folds.

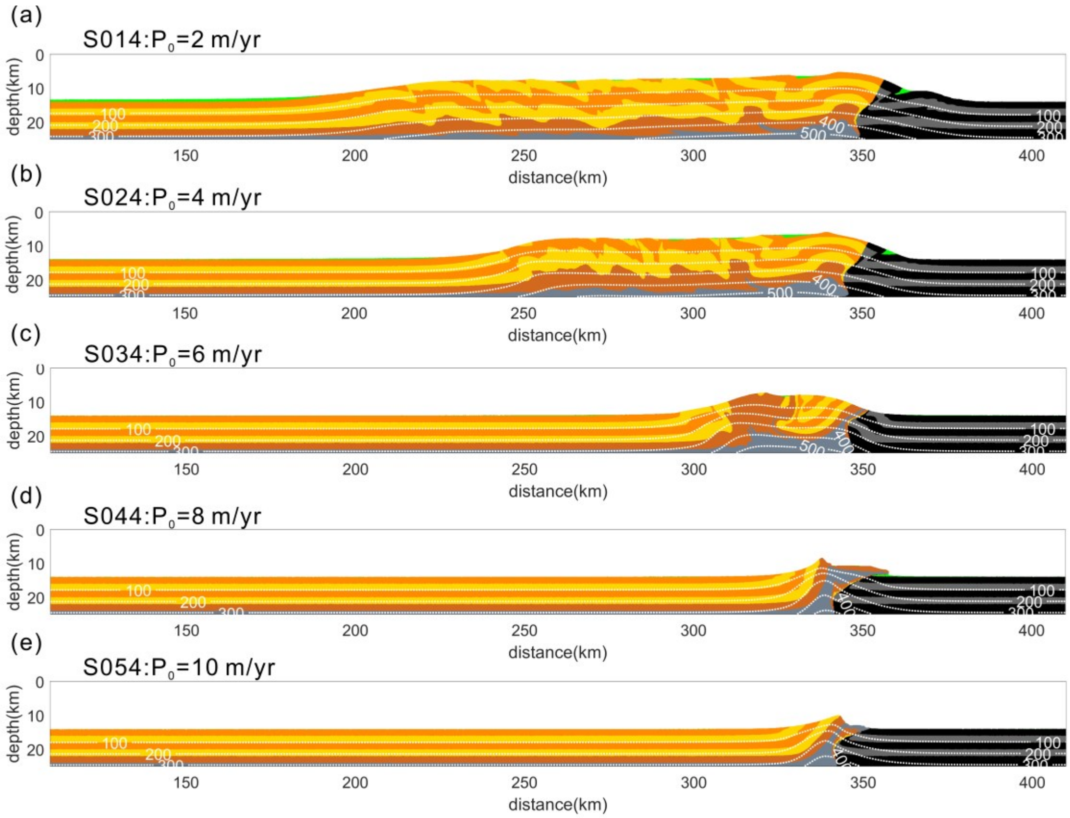

Figure 4. Numerical modelling results showing the influence of the average precipitation(P_0) on the evolution of orogenic wedges. The white dashed lines indicate isotherms (in ℃). For all models, the convergence rate(v_c) is 2.0 cm/yr, the initial geothermal gradient(dT/dh) is 30 ℃/km, and the runtime is 8 Myr. The average precipitations for (a), (b), (c), (d) and (e) are 2 m/yr, 4 m/yr, 6 m/yr, 8 m/yr and 10 m/yr, respectively. The width and height of the orogenic wedge decrease as the average precipitation increases, while keeping the convergence rate constant. At the same time, the rock deformation exhibits the tendency from imbricate thrusting toward folding.

Besides convergence rate and average precipitation, geothermal conditions also play a significant role in influencing the evolution of orogenic wedges. Since the geothermal gradients at the model's bottom boundary are set to remain consistent with the initial geothermal gradients, the initial geothermal gradient not only affects the initial geothermal field but also influences the heat flow at the bottom of the model. This means that increasing the initial geothermal gradient will enhance the overall geothermal field of the model, and vice versa. Our modelling results indicate that, under constant convergence rate and average precipitation, a gentler initial geothermal gradient favors developing wider orogenic wedge and higher topography. Additionally, it tends to promote the formation of imbricate structures (Figure 5a and b). Models with steeper initial geothermal gradients tend to develop narrower orogenic wedges and lower topographies, and the deformation style is dominated by folding (Figure 5c and d). In this context, increasing the initial geothermal gradient has a comparable effect to strengthening the relative dominance of climatic forces over tectonic forces, as both contribute to the softening of crustal rocks. This can be attributed to the former enhancing the overall geothermal field, while the latter can localize deformation and steepen geothermal gradients. These will elevate the temperature and strain rate of the rocks, leading to a decrease in viscosity, thereby weakening the rock strength.

Figure 5. Numerical modelling results showing the influence of the initial geothermal gradient(dT/dh) on the evolution of orogenic wedges. The white dashed lines indicate isotherms (in ℃). For all models, the convergence rate(v_c) is 2.0 cm/yr, the average precipitation (P_0) is 6 m/yr, and the runtime is 8 Myr. The initial geothermal gradients for (a), (b), (c) and (d) are 20 ℃/km, 25 ℃/km, 30 ℃/km and 35 ℃/km, respectively. The width and height of the orogenic wedge decrease as the initial geothermal gradient increases. At the same time, the rock deformation exhibits the tendency from imbricate thrusting toward folding.

4.2 Evolutionary regimes of orogenic wedges

Based on the relative dominance of tectonic and climatic forces, as well as the features of tectonic and topographic evolution, the modelling outcomes can be categorized into three basic types of orogenic wedge (or evolutionary regimes), which can be referred as type A, B and C (Figure 6). A type A orogenic wedge is dominated by climatic forces compared to tectonic forces (Figure 6a). The most typical feature of this type of orogenic wedge is the rapid obliteration of initial deformation structures and topography due to intense erosion before reaching a steady state. In most cases, this process occurs within approximately 3 Myr, although in a few cases the topography may persist for 5~6 Myr. During this phase, there can be rapid and significant variations in the structural and topographic characteristics. However, the ultimate tendency is towards topographic flattening, resulting in minimal preservation of deformation structures (Figure 3a, Figure 4d and e, Figure 5d). Once a steady state is reached, a type A orogenic wedge maintains a long-term stable equilibrium of material flux. Conversely, A type B orogenic wedge is dominated by tectonic forces compared to climatic forces (Figure 6b). In a type B orogenic wedge, the erosional efficiency is insufficient so that the erosional outflux cannot balance the tectonic influx. This results in continuous expansion of deformation towards the foreland basin, forming orogenic wedge with large size and high topography. A type B orogenic wedge does not attain a stable equilibrium of material flux, and its deformation style is dominated by imbricate thrusting.

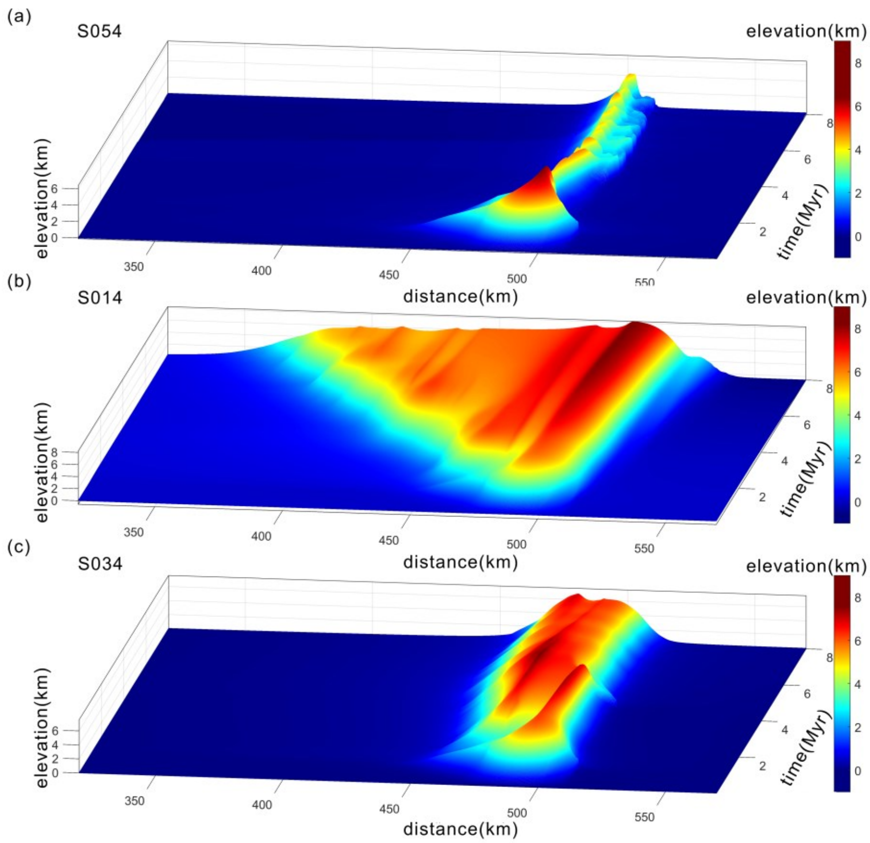

Figure 6. The geomorphic evolution of typical models of three basic types of orogenic wedge. (a) is the representative of type A orogenic wedge, which is dominated by the climatic forces. In this case, the width and height of the wedge shrink rapidly starting from t=1 Myr until the topography is almost entirely erased before reaching a steady state. (b) is the representative of type B orogenic wedge, which is dominated by the tectonic forces. In this case, the deformation continuously extends towards the foreland basin, leading to high topography and wider wedge. (c) is the representative of type C orogenic wedge, in which the climatic and tectonic forces exhibit comparable strength. In this case, the material flux reaches a steady state after a brief period of adjustment (around 1 Myr). Subsequently, the height, width and the topography of the wedge can remain relatively stable in the long-term time.

When the climatic and tectonic forces exhibit comparable strength, it gives rise to type C orogenic wedge (Figure 6c). In this case, the orogenic system is able to establish a dynamic equilibrium within a short period of time (around 1 Myr). In this state of equilibrium, the material flow field, width of the orogenic wedge, topography and deformation style of rocks can remain relatively stable in the long-term time (Figure 3b, Figure 4b, Figure 5b and c). In contrast to type A orogenic wedge, a type C orogenic wedge in a state of equilibrium retains a certain amount of deformation structures, resulting in a relatively larger size. The deformation style in a type C orogenic wedge is variable and it can manifest as either imbricate thrusting (Figure 5b) or folding (Figure 5c), depending on the shallow crustal geothermal field or other factors.

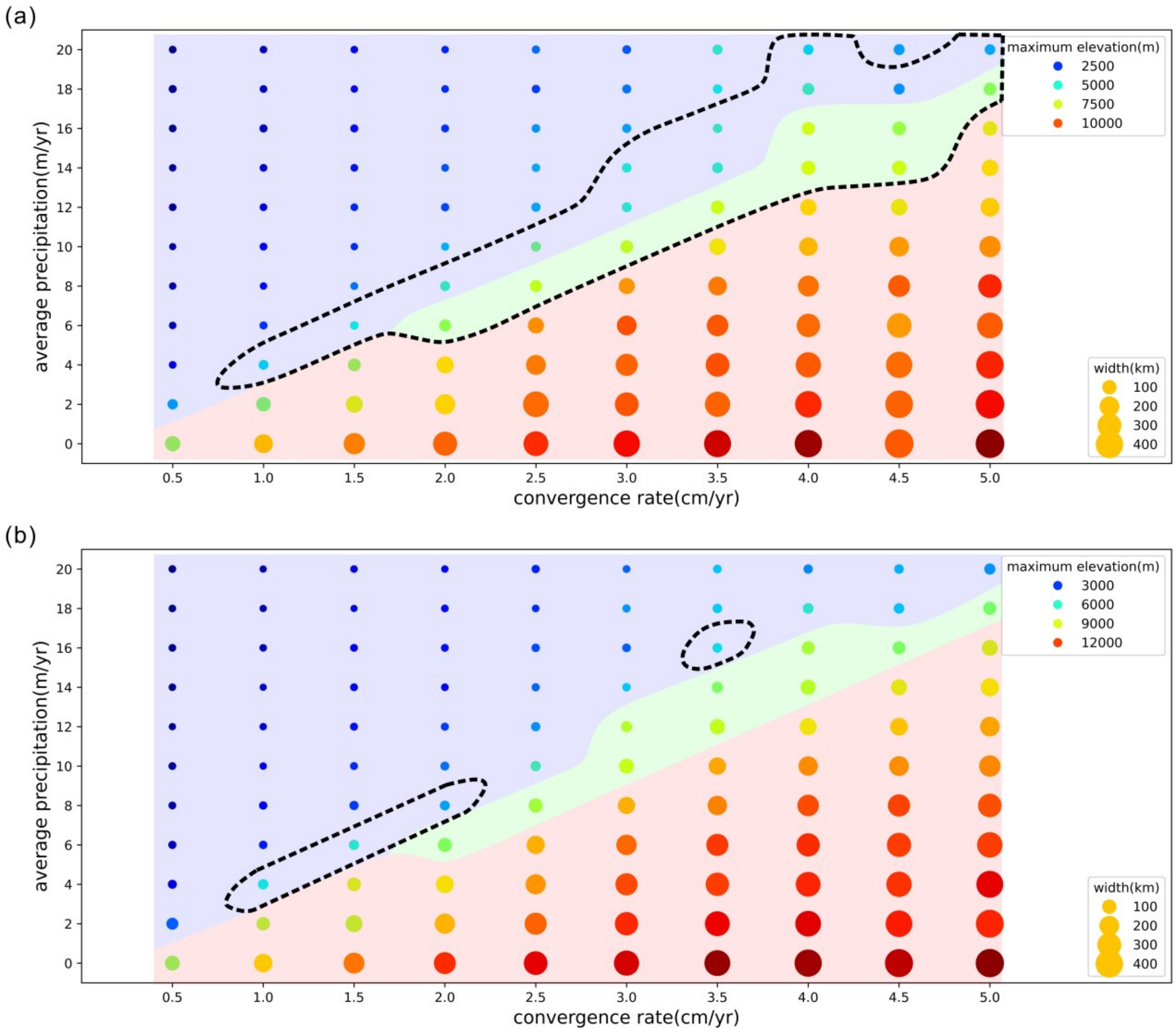

Figure 7. Orogenic wedge type as a function of convergence rate and average precipitation for cases with an initial geothermal gradient of 30 (a) and 25 (b) °C/km. Each point inside the diagrams represents one numerical experiment in Table S2 and S3 in Supporting Information S1. The color and size of each point indicate the maximum elevation and width of the orogenic wedge (at t=8 Myr), respectively. The regions marked in light blue, light red, and light green correspond to the orogenic wedges categorized as type A, B and C, respectively. Enclosed within the dashed circle are the models that exhibit similar structural features to the eastern Himalayan syntaxis (Type D zone). The distribution of type A, B and C orogenic wedges doesn't show significant variation when the initial geothermal gradient changes, but the Type D zone shrinks as the initial geothermal gradient decreases.

In the parameter space of the average precipitation and convergence rate, a certain regularity can be observed about the distribution of the three basic types of orogenic wedges (Figure 7). Irrespective of whether the initial geothermal gradient is 30 or 25 °C/km, type C orogenic wedges are primarily located near the line $P_0 = 4 \times v_c - 2$ (where P_0 is in units of m/yr, v_c is in units of cm/yr, and v_c > 1.5 cm/yr), while type A and type B orogenic wedges are distributed above and below this line, respectively. This distribution pattern remains relatively stable regardless of the variation in the initial geothermal gradient. This is reasonable because the three basic types of orogenic wedges are essentially the result of different relative strengths of tectonic and climatic forces, and this distribution pattern corresponds to different parameter ranges of different relative strengths between the two forces.

Figure 8. Typical models that exhibit similar structural features to the eastern Himalayan syntaxis. The white dashed lines indicate isotherms (in °C). When the convergence rate, average precipitation and initial geothermal gradient fall within certain ranges, several significant structural features resembling those observed in the syntaxis will emerge within the orogenic wedge. At a particular geological time (t) during model evolution, sustained, stationary, and localized erosion induces localized rock uplift and deformation, forming large-scale antiforms. In the core areas of the antiforms, extreme relief, deep exhumation, intense deformation and steepening of the near-surface thermal gradient overlap spatially.

Among type A and type C orogenic wedges, we identified a fourth special type of orogenic wedge (referred as type D), which exhibits similar structural features to the eastern

Himalayan syntaxis at a particular geological time (Figure 8). When the convergence rate, average precipitation and initial geothermal gradient fall within certain ranges, it leads to the development of sustained, stationary, and localized erosion within the orogenic wedge. This further induces rapid uplift of rocks in a local area, forming large-scale antiforms. In the core areas of the antiforms, extreme relief, deep exhumation, intense deformation and steepening of the near-surface thermal gradient overlap spatially. These structural features closely approximate the field observations in the eastern Himalayan syntaxis region. However, for those orogenic wedges that belong to both type D and type A, such antiformal structures cannot be preserved for a very long time. Generally, they are completely destroyed within around 1 Myr after their formation, but for those belonging to both type D and type C, these structures can be sustained for a longer period (usually >2 Myr). Similar to type C orogenic wedges, the majority of the type D orogenic wedges conform to the condition of relatively balanced climatic and tectonic forces, but their distributions in the $P_0 - v_c$ parameter space do not align perfectly (Figure 7). Here we refer to the domain corresponding to type D orogenic wedges in the $P_0 - v_c$ parameter space as “Type D zone”. Unlike the distribution pattern of the three basic types, the Type D zone is highly sensitive to the initial geothermal gradient, and it shrinks considerably when the initial geothermal gradient decreases from 30 to 25 °C/km. Moreover, it can be observed that the Type D zone tends to expand with an increase in the initial geothermal gradient or average precipitation increase (Figure 7). As discussed above, the increase in initial geothermal gradient and average precipitation promotes a decrease in effective viscosity of crustal rocks. This founding implies that the softening of the crustal rocks appears to favor the formation of syntaxes.

Our results indicate that the tectonic and topographic evolution of an orogenic wedge is the result of the combined effects of crustal shortening, precipitation, and geothermal field.

5 Discussion

5.1 Model limitations

The distribution pattern depicted in Figure 7 is related to the initial model configuration. It can be inferred that the distribution of different types of orogenic wedges in $P_0 - v_c$ parameter space may vary slightly if the initial model configuration, such as the rheology of the initial undeformed rock sequence, is altered. Therefore, it may not perfectly fit every similar numerical model or orogenic region. Nevertheless, the regularities revealed by regime diagram (Figure 7) are expected to exist in nature. Moreover, although the type D orogenic wedges closely match the field observations from the eastern Himalayan syntaxis in various aspects, some crucial features still haven’t been reproduced in our simulation. For instance, although a simple partial melting model is included in our simulation, obvious partial melting of rocks is not observed in the type D orogenic wedges. Nevertheless, the depression melting process in the eastern Himalayan syntaxis since 10 Ma is widely recognized (Booth et al., 2009; Koons et al., 2013).This discrepancy is probably attributed to the simplifications in our initial model configuration, including simplified profile of rock sequence and thermal structure. The initial state of the eastern Himalayan syntaxis around 8 million years ago was more complex than we assumed.

For simplicity, we assume that the surface processes are fluvially-dominated. In other words, above the ELA, we substitute fluvial erosion for glacial erosion. This will inevitably introduce errors. Most of our modelling results, especially the type B orogenic wedges, exhibit peak elevations far exceeding the highest peak on Earth (8848 m) (Figure 7). This could be due to the absence of an accurate glacial erosion process in our models. Glaciers can limit mountain height through a distinct mechanism of erosion, known as glacial buzzsaw (Egholm et al., 2009). Therefore, coupled surface process model accounting for both fluvial and glacial activities is necessary for more accurate modelling of landscape evolution in the eastern Himalayan syntaxis region.

In order to simulate the co-evolution of topography and climate, we employed a simplified model for orographic precipitation (Equation 9). While this precipitation model can capture the primary characteristics of precipitation distribution in mountainous regions, it tends to overestimate the precipitation in the inland areas on the leeward side of the mountain ranges and leads to minor unrealistic erosion (Text S3 and Figure S1 in Supporting Information S1, Figure 9 and 10). In the future, constructing more realistic precipitation models could be a promising research direction.

Since orogenic wedges or syntaxes are three-dimensional in reality, the 2D geometry employed in this study renders the models inadequate for addressing a number of significant aspects of orogenic development, such as the growth of structures oriented parallel to plate boundaries, the development of possible strike-slip faults and the evolution of 2D topography, etc. Therefore, this work would be greatly improved if these geological processes are simulated in 3D models.

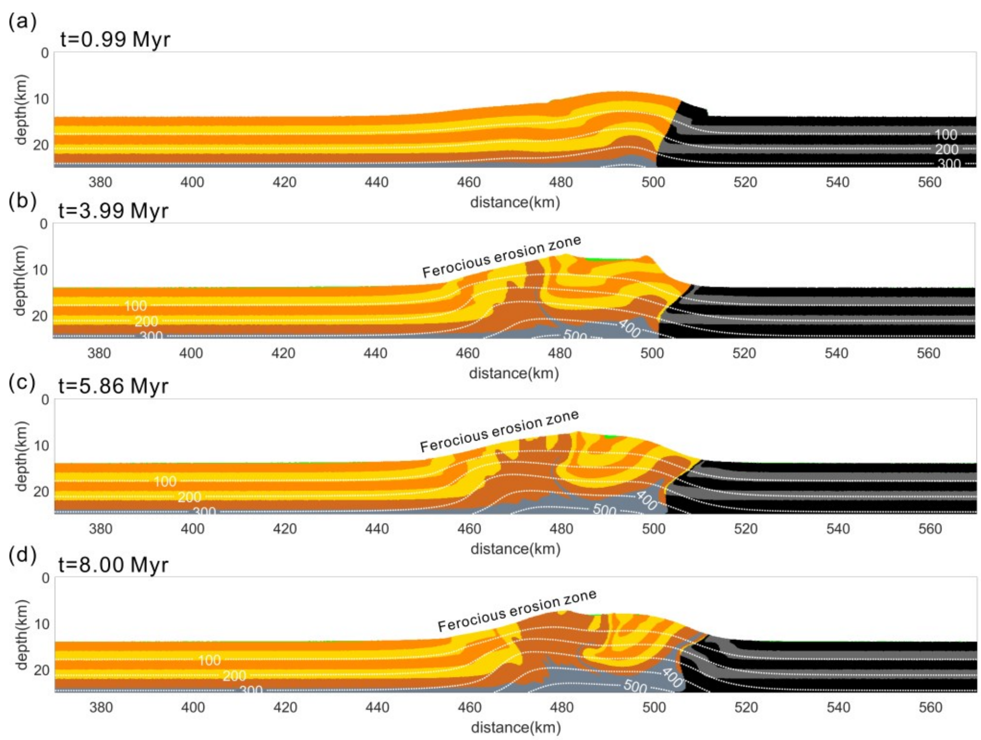

Figure 9. Modelling results showing the evolution of model S034. The white dashed lines indicate isotherms (in ℃). The orographic precipitation applied from t=1 Myr induces rapid erosion within a narrow zone on the windward flank. Most of the material entering the orogenic wedge “flows out” through this narrow window, resulting in relatively stable positioning of the zone with rapid erosion and the width of the orogenic wedge. Sustained, stationary, localized and rapid erosion induces rapid uplift of rocks in local area, leading to the formation of a large-scale antiform.

5.2 Comparison with the eastern Himalayan syntaxis

Taking account of parameter selection and modelling results, we identify that model S034 best matches the field observations from the eastern Himalayan syntaxis (Figure 9 and 10). In model S034, the applied orographic precipitation starting at t=1 Myr induces rapid erosion within a narrow zone (20~25 km scale) on the windward flank of the orogenic wedge (Figure 9 and 10b). Rapid erosion and decompression further result in rapid uplift, exhumation, and deformation of local rocks (Figure 9 and 11). It can be observed that the position of this intense erosion zone and the width of the orogenic wedge remain relatively stable in the long-term time (several million years), indicating a relative equilibrium in the material influx and outflux. This implies that most of the material entering the orogenic wedge "flows out" of this limited area via the narrow erosional window. The magnitudes of the crucial parameters (such as convergence rate, average precipitation and initial geothermal gradient) and the underlying physics (conservation of mass, momentum and energy, rheology, orographic precipitation, surface processes, etc.) ensure that the model develops sustained, stationary, localized, rapid erosion, and decompression on the windward flank. This further induces sustained, rapid rock uplift, exhumation, and deformation in the local area, ultimately forming a large-scale antiform (Figure 9 and 10). These outcomes appear to be the inevitable results of the delicate equilibrium among tectonic forces, climatic forces and crustal thermal structure under various physical laws.

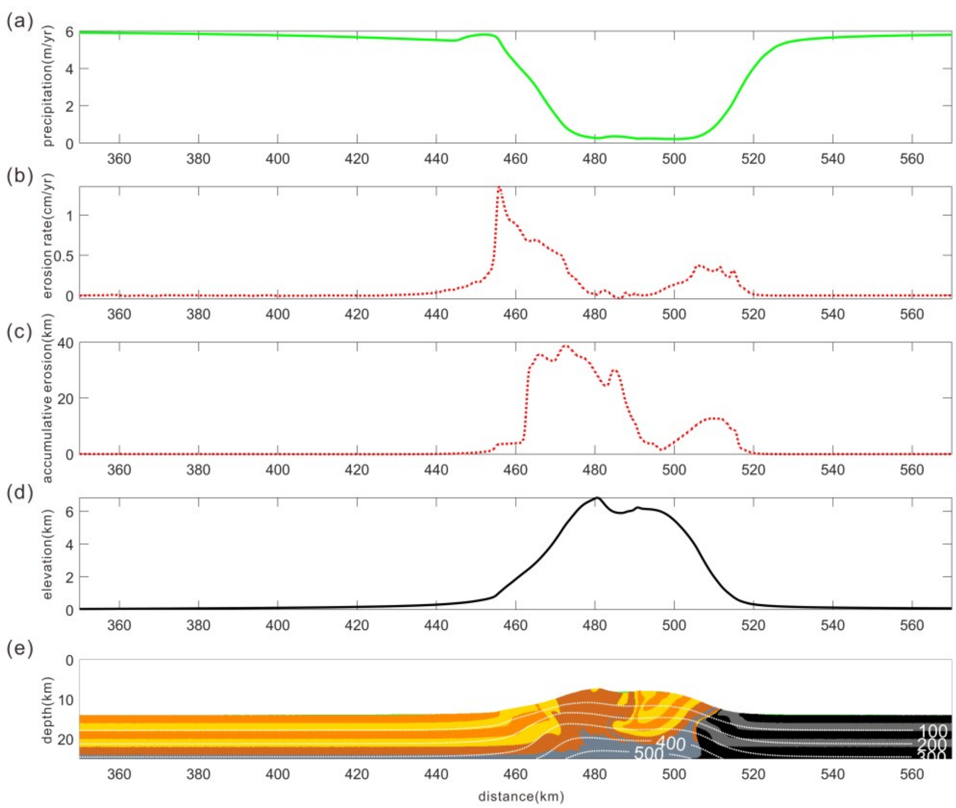

Figure 10. Modelling results of model S034 at t=8 Myr. The modelling results closely approximate various significant aspects of the field observations from the eastern Himalayan syntaxis. (a), (b), (c) and (d) represent the precipitation, transient erosion rate, accumulative erosion and topography along the model cross-section profile, respectively. (e) demonstrates the deformation pattern of the model, where white dashed lines indicate isotherms (in °C).

In model S034, the spatial scale of the area with rapid exhumation and intense deformation in the core of the antiform is about 25 km, which is close to the actual observations from the eastern Himalayan syntaxis (Koons et al., 2013; Zeitler, Meltzer, et al., 2001). The transient erosion rate of 0.5~1.4 cm/yr within the intense erosion zone (Figure 10b) also matches the decadal erosion rate reported by Enkelmann et al. (2011) based on the study of detrital zircon. The accumulative erosion (20~40 km) within this zone is slightly greater than the exhumation (>20 km) inferred from P-T estimates and thermochronological dating (Figure 10c) (Koons et al., 2013). This is reasonable because the rock trajectories within the orogenic wedge are usually non-vertical. Furthermore, the maximum elevation in the core of the antiform reaches approximately 6817 m, which is comparable to the elevations of the two main peaks, Namche Barwa Peak (7782 m) and Gyala Peri Peak (7294 m), in the eastern Himalayan syntaxis region.

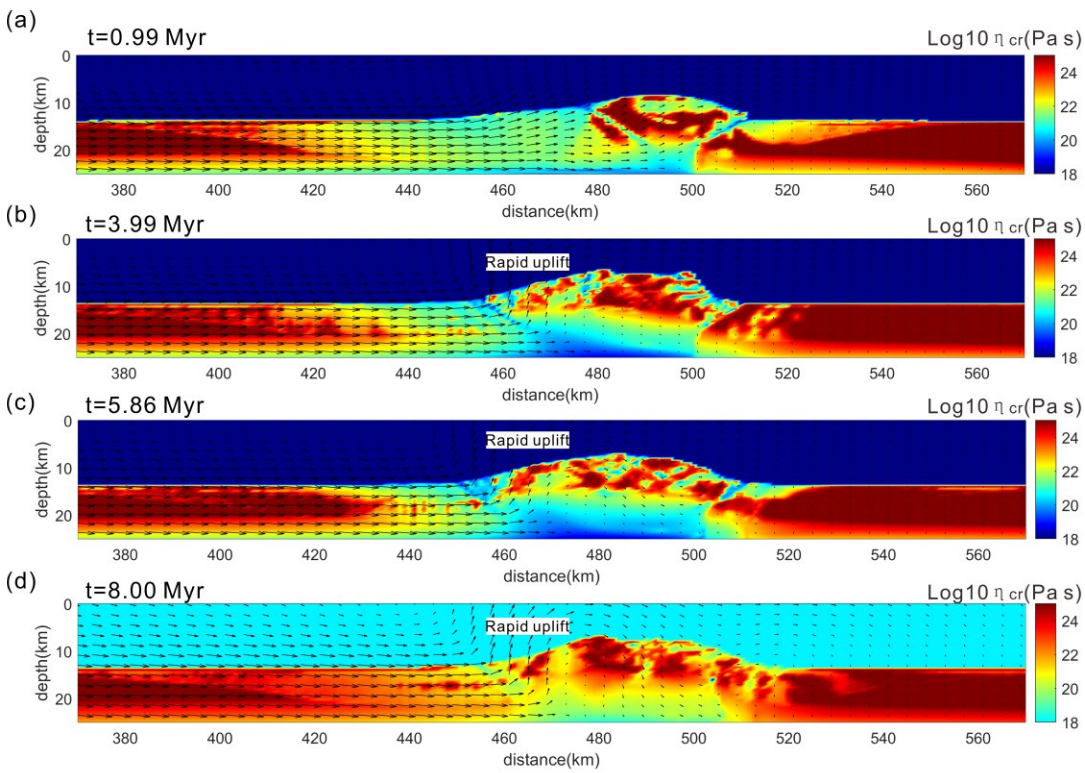

Figure 11. The evolution of the viscosity and velocity field in model S034. Within the intense erosion zone on the windward flank of the orogenic wedge, rapid erosion and decompression induce continuous and rapid uplift of rocks. However, the model doesn't show a significant decrease in the viscosity of rocks within this intense erosion zone.

However, the selected average precipitation of 6 m/year in model S034 is much higher than the current average precipitation (~2 m/yr) in the eastern Himalayan syntaxis region (Anders et al., 2006; Bookhagen & Burbank, 2006), although this value may not align well with the historical precipitations. It's important to note that, due to the model limitations, the erosion rates generated by our surface processes model may be underestimated for two reasons. Firstly, the glacial erosion was not fully accounted for in our model. Secondly, our modelling on landscape evolution employs a 3-by-N grid, which may result in lower water discharge at each point compared to real-world conditions, leading to lower erosion rates. Therefore, to achieve a better approximation of the actual erosional efficiency in the eastern Himalayan syntaxis region, a higher average precipitation would be required. In addition, the convergence rate of 2.0 cm/yr in model S034 is consistent with the Himalayan shortening rate obtained from the reconstruction of the India-Asia convergence history (Guillot et al., 2003). A relatively steep initial geothermal gradient of 30 ℃/km also approximates the relatively hot regime that characterized the majority of the Himalayan-Tibetan Plateau soon after the collision (Zhang et al., 2022).

In summary, the simulation results of model S034 closely match the field observations in the eastern Himalayan syntaxis region from various perspectives, indicating that our modelling scheme is applicable to the study area. Therefore, the mechanisms of tectonic and geomorphic evolution revealed by the model are reliable.

5.3 Syntaxis as the result of the combined effects of multiple factors

Our modelling results indicate that different combinations of tectonic and climatic forces result in various types of orogenic wedges. The three basic types of orogenic wedge mentioned above closely resemble the three end-member types of growing orogens proposed by Wolf et al. (2022). The only difference is that their model is defined on a larger scale (mantle-scale), while our model operates at a relatively smaller scale, specifically limited to the orogenic wedges or fold and thrust belts. Wolf et al. (2022)'s modelling study also shows that the topographic evolution of collisional orogens is determined by the combination of plate velocity, crustal rheology and surface process efficiency. As early as the end of the last century, Avouac and Burov (1996) had proposed that there is a coupled regime allowing for mountain growth. They showed that mountain growth only occurs when the surface mass diffusion and lithospheric shortening exhibit comparable efficiency, otherwise the mountain will "collapse". Similar combined effect of tectonic and climatic forces was also identified in smaller-scale models (Simpson, 2004). This is also supported by the analytical treatment studies. For instance, Roe et al. (2006) have found that the width (L) or height (R_c) of a fluvial-dominated steady-state orogenic wedge is related to both accretionary flux (F) and average precipitation (P_0):

$$R_c(or\ L) \propto F^{\frac{1}{1+h_k m}} P_0^{\frac{-m}{1+h_k m}} \quad (11)$$

where m and n are the discharge and slope exponents, respectively (Whipple & Tucker, 1999). h_k is the Hack's law exponent (Hack, 1957).

Considering the initial thickness of the incoming plate (H) to be relatively constant for a specific orogenic wedge, the accretionary flux can be rewritten as (Dahlen, 1990; Whipple & Meade, 2004):

$$F = Hv_c \quad (12)$$

where v_c is the convergence rate. Substituting Equation (12) into Equation (11) and rearranging:

$$R_c(or\ L) \propto \left(\frac{{P_0}^m}{v_c}\right)^{\frac{-1}{1+h_k m}} H^{\frac{1}{1+h_k m}} \quad (13)$$

since H is assumed to be relatively constant, we get:

$$R_c(or\ L) \propto \left(\frac{{P_0}^m}{v_c}\right)^{\frac{-1}{1+h_k m}} \quad (14)$$

From the perspective of energy, the convergence rate and average precipitation can be regarded as significant indicators of the strength of tectonic and climatic forces , respectively

(Xiangjiang & Dalai, 2017). As shown by our modelling results, Equation (14) supports the perspective that the height and width of a specific orogenic wedge primarily rely on the relative strength of tectonic and climatic forces, rather than their respective magnitudes. As m and h_k are typically positive (Montgomery & Dietrich, 1992; Whipple & Tucker, 1999), Equation (14) suggests that the height and width of an orogenic wedge decrease with increasing ratio of average precipitation to convergence rate, which is consistent with our modelling results (Figures 3, 4 and 7). The proportionality symbol (∝) in Equation (14) implies that there are other factors influencing the evolution of orogenic wedges, such as rock erodibility, orogen geometry, and critical taper angle (Roe et al., 2006; Roe et al., 2008). According to our modelling, the geothermal gradients within the crust is also one of the important factors.

Here we assume that the maximum elevation of an orogenic wedge ($MaxE$) is proportional to its height. Then, based on Equation (14), if the convergence rate holds constant, we have:

$$MaxE \propto {P_0}^{x_1} \quad (15)$$

or

$$MaxE = A_1 {P_0}^{x_1} \quad (16)$$

In the same way, if the average precipitation holds constant, we have:

$$MaxE \propto {v_c}^{x_2} \quad (17)$$

or

$$MaxE = A_2 {v_c}^{x_2} \quad (18)$$

where A_1, A_2, x_1, x_2 are coefficients.

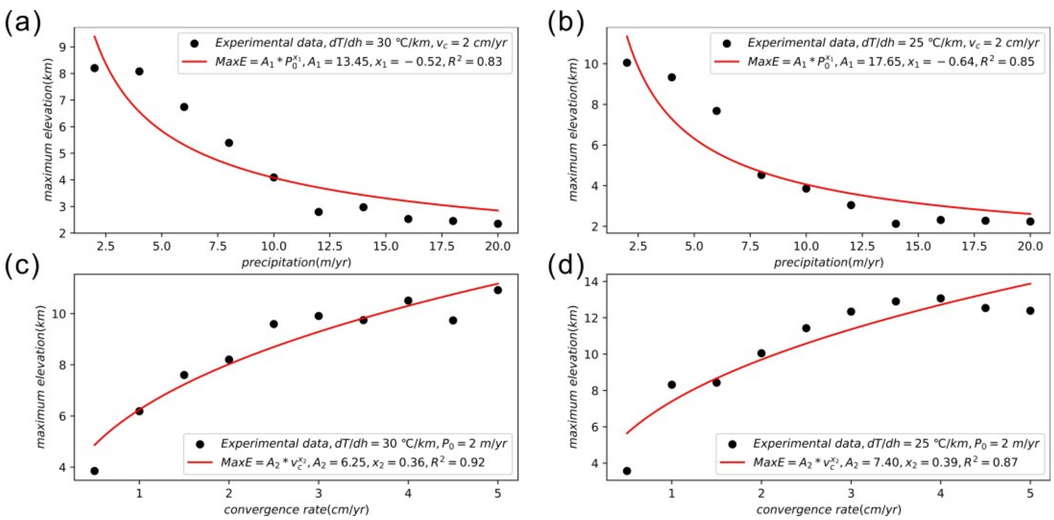

Figure 12. The relationships between the maximum elevations of orogenic wedges and the average precipitations ((a) and (b)) or convergence rates((c) and (d)). Each black dot represents one numerical experiment. Experiments in (a) and (b) have a convergence rate of 2 cm/yr and initial geothermal gradients of 30 °C/km and 25 °C/km, respectively, while experiments in (c) and (d) have an average precipitation of 2 m/yr and initial geothermal gradients of 30 °C/km and 25 °C/km, respectively. The red solid lines represent the best-fit curves obtained through least-squares method using Equation (16) for (a) and (b), and Equation (18) for (c) and (d). The fitting results (R^2>0.83) indicate a good power-law relationship between the maximum elevations of orogenic wedges and both the average precipitations and convergence rates.

To further confirm the above relationships, we performed a least-squares fitting on our experimental data (Figure 12). In Figure 12a and b, the black dots represent the experiments with a convergence rate of 2 cm/yr and initial geothermal gradients of 30 °C/km and 25 °C/km, respectively. Equation (16) was used for fitting, and the fitted values of x_1 are -0.52 and -0.64, with corresponding R^2 of 0.83 and 0.85. Similarly, in Figure 12c and d, the experiments have an average precipitation of 2 m/yr and initial geothermal gradients of 30 °C/km and 25 °C/km, respectively. Equation (18) was used for fitting, and the fitted values of x_2 are 0.36 and 0.39, with corresponding R^2 of 0.92 and 0.87. Theoretically, the values of x_1 and x_2 should be -0.25 and 0.5, respectively (assuming $m = 0.5$ and $h_k = 2$ as suggested by Whipple and Tucker (1999) and Montgomery and Dietrich (1992)). The deviation between the theoretical and fitted values may attribute to the more complex precipitation, surface processes and rheology considered in our model. Nevertheless, both analytical treatment and our numerical modelling indicate that there is a specific power-law relationship between the orogen height and the average precipitation or convergence rate, with negative and positive exponents for average precipitation and convergence rate, respectively.

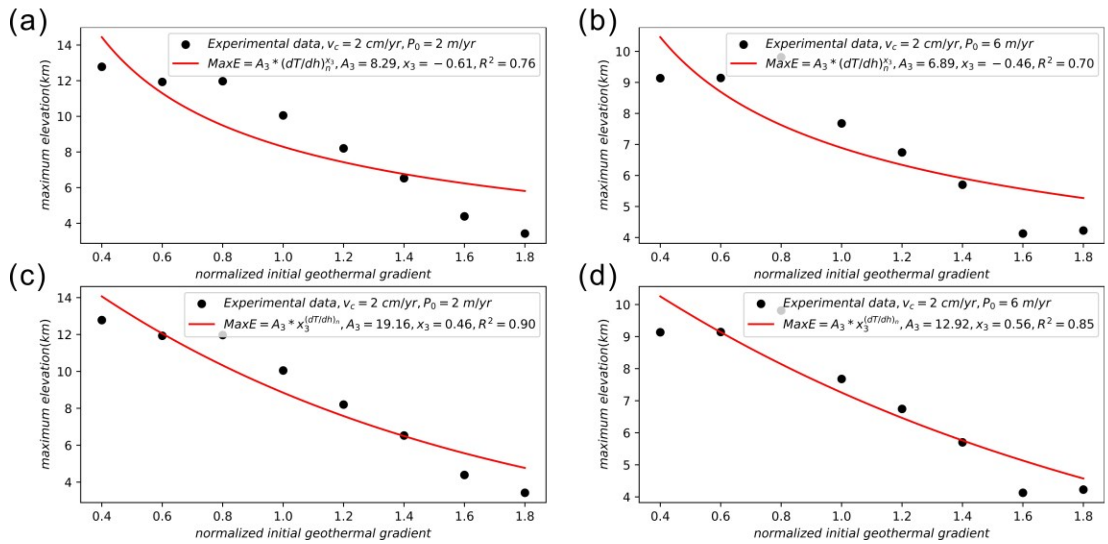

Figure 13. The relationships between the maximum elevations of orogenic wedges and initial geothermal gradients. Each black dot represents one numerical experiment. Experiments in (a) and (c) have a convergence rate and average precipitation of 2 cm/yr and 2 m/yr, respectively, while experiments in (b) and (d) have a convergence rate of 2 cm/yr and an average precipitation of 6 m/yr. The red solid lines represent the best-fit curves obtained through least-squares method using Equation (20) for (a) and (b), and Equation (21) for (b) and (d). The fitting results indicate that the exponential equation provides a better fit than the power-law equation, suggesting a higher probability of an exponential relationship between the maximum elevation of an orogenic wedge and the initial geothermal gradient.

According to our modelling results (Figure 5), it is conceivable that the relationship between the maximum elevation of an orogenic wedge and the initial temperature gradient may follow a similar pattern as its relationship with the average precipitation. In other words, under the condition of constant convergence rate and average precipitation, we may have:

$$MaxE \propto (dT/dh)_n{}^{x_3} \quad (19)$$

or

$$MaxE = A_3(dT/dh)_n{}^{x_3} \quad (20)$$

where A_3 and x_3 are coefficients. $(dT/dh)_n$ is the initial temperature gradient normalized by average shallow crustal geothermal gradient (25 °C/km). However, when Equation (20) is used for fitting, the resultant goodness of fit is not satisfactory (Figure 13a and b). For two sets of experimental data with a convergence rate of 2 cm/yr and average precipitation of 2 m/yr and 6 m/yr, respectively, the corresponding R^2 are 0.76 and 0.70. This suggests that the relationship between the maximum elevation and the initial temperature gradient may not follow a power-law relationship. On the contrary, it is more likely to exhibit an exponential function relationship:

$$MaxE = A_3 x_3{}^{(dT/dh)_n} \quad (21)$$

When fitting the same dataset using Equation (21), we achieved significantly improved goodness of fit (the fitted values of x_3 are 0.46 and 0.56, with corresponding R^2 of 0.90 and 0.85, as depicted in Figure 13c and d). This indicates that Equation (21) is more likely to reveal the quantitative relationship between the maximum elevation and the initial temperature gradient compared to Equation (20).

Combining Equations (15), (17) and (21) gives:

$$MaxE \propto P_0{}^{x_1} v_c{}^{x_2} x_3{}^{\left(\frac{dT}{dh}\right)_n} \quad (22)$$

or

$$MaxE = A * P_0{}^{x_1} v_c{}^{x_2} x_3{}^{\left(\frac{dT}{dh}\right)_n} \quad (23)$$

similarly, A, x_1, x_2 and x_3 are coefficients. To unveil the combined effect of average precipitation, convergence rate, and initial temperature gradient on the topographic evolution, we conducted a least-squares fitting on the data from 212 experiments in this study (excluding the 20 experiments with zero precipitation) using Equation (23). The fitted values of $x_1 = -0.35$, $x_2 = 0.71$ and $x_3 = 0.46$ were obtained, with a corresponding R^2 of 0.82. The fitted values of x_1, x_2 and x_3 are sensitive to the dataset used. Statistical analysis of the above fitted values obtained from different datasets showed that the population standard deviations of the fitted values of x_1, x_2 and x_3 are 0.12, 0.16, and 0.047, respectively, none of which exceeds 33% of the absolute value of the mean of the fitted values, indicating that the coefficients are relatively stable. Based on Equation (23), we define the following parameter (E_F):

$$E_F = P_0{}^{-0.35} v_c{}^{0.71} 0.46^{(dT/dh)_n} \quad (24)$$

This parameter can be used to evaluate the combined effect of average precipitation, convergence rate and crustal thermal structure on the topographic evolution of an orogenic wedge. As shown in Figure 14, on the whole, the maximum elevation of the orogenic wedge increases with an increase in E_F. However, when E_F>0.45, the slope becomes gentler, indicating that the orogenic wedge may be in a critical state around $E_F \approx 0.45$. On either side of this critical state (E_F<0.45 or E_F>0.45), the evolution of an orogenic wedge seems to exhibit different patterns. This suggests that orogen is not simply a linear system (Phillips et al., 2003), and highly complex nonlinear mechanisms may be involved during its evolutionary process. Moreover, it is evident that most of the type A and B orogenic wedges are distributed on the left and right sides of line E_F=0.45, respectively, while type C orogenic wedges are distributed around this line. Type D orogenic wedges are primarily concentrated within the narrow band of 0.24<E_F<0.45. Admittedly, the four types of orogenic wedges cannot be perfectly identified through the value of E_F. This may be attributed to the fact that most experiments at the boundaries of two different types of orogenic wedges in Figure 7 are actually transitional types, and they were assigned to the category that best represents their most prominent features. This is inevitable and it may have introduced some degree of error. Nevertheless, our modelling results indicate that the tectonic and geomorphic evolution of the orogenic wedge is closely related to parameter E_F. Furthermore, we estimated the E_F of the eastern Himalayan syntaxis based on a convergence rate of 2.0 cm/yr (Guillot et al., 2003), an average precipitation of 2.0 m/yr (Anders et al., 2006; Bookhagen & Burbank, 2006) and a crustal geothermal gradient of 50 ℃/km (Craw et al., 2005). The result shows that the E_F (0.27) of the eastern Himalayan syntaxis is also situated within the specific range, implying that the tectonic and geomorphic evolution of the syntaxis is not solely influenced by a single factor but the result of the combined effects of multiple factors (Figure 14).

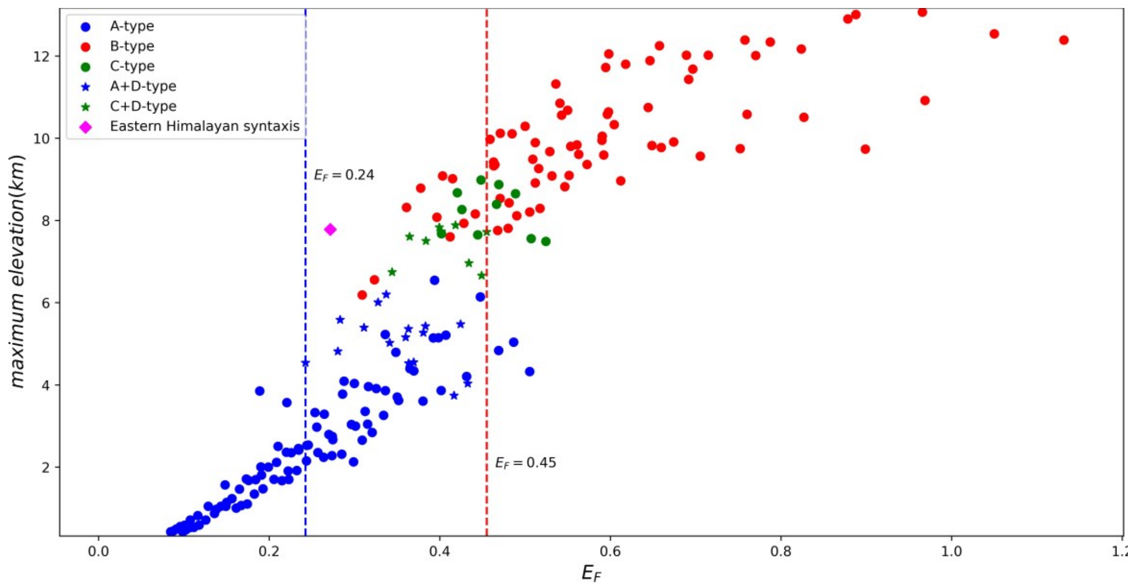

Figure 14. Plot of the maximum elevation of the orogenic wedges against E_F. The dots and stars represent the 200 experiments from Table S2 and S3 in Supporting Information S1 (20 experiments with average precipitation of 0 m/yr are excluded). The blue, red and green colors correspond to type A, B and C orogenic wedges, respectively. The stars represent orogenic wedges that exhibit similar structural features to the eastern Himalayan syntaxis (type D). Most of the type A and B orogenic wedges are distributed on the left and right sides of line $E_F = 0.45$, respectively, while type C orogenic wedges are distributed around this line. Type D orogenic wedges are primarily concentrated within the narrow band of $0.24 < E_F < 0.45$, and the eastern Himalayan syntaxis, depicted as a fuchsia diamond, is also situated within this specific range. On the whole, the maximum elevation of orogenic wedges is proportional to E_F, but the slope becomes gentler when $E_F > 0.45$. This suggests that orogenic wedges seem to be in a critical state when $E_F \approx 0.45$. Thus the evolution of an orogenic system should be non-linear.

5.4 The mechanism of the formation of the eastern Himalayan syntaxis

All the three classical models explaining the formation of syntaxis have undergone extensive testing through abundant field observations and numerical modeling studies (Bendick & Ehlers, 2014; Burg et al., 1998; Burg & Podladchikov, 1999; Burg & Schmalholz, 2008; Ding et al., 2001; Koons et al., 2002; Koptev et al., 2019; Nettesheim et al., 2018; Yang et al., 2023; Zeitler, Koons, et al., 2001; Zeitler et al., 2014; Zhang et al., 2004). Our modelling results indicate that the processes involved in the formation of syntaxis are more closely associated with those described by the tectonic aneurysm model (Figure 8 and 9), and we propose that the initiation of these processes requires the cooperation of tectonic forces, climatic forces and geothermal field (Figure 15).

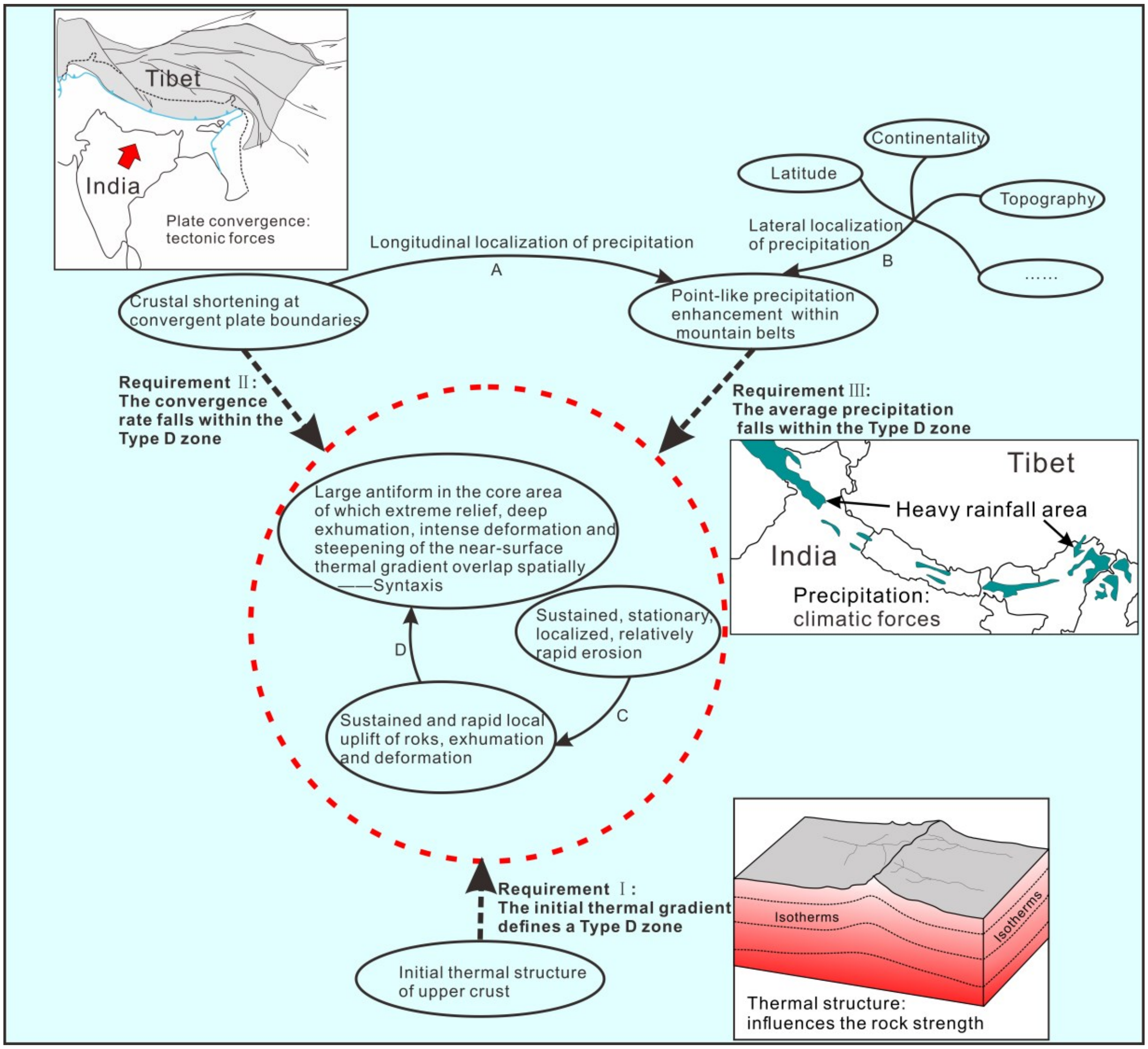

Figure 15. The proposed mechanism of the formation of the eastern Himalayan syntaxis. The elements outside the red dashed circle are the conditions for the formation of a syntaxis, while the elements inside the red dashed circle show the process of its formation. The formation of a syntaxis requires the combination of tectonic forces, climatic forces and crustal thermal structure. Once the convergence rate and the average precipitation fall within the Type D zone determined by the thermal structure of shallow crust, a sustained, stationary, localized and relatively rapid erosion process will be established on the windward flank of the orogenic wedge. This will further induce sustained and rapid uplift of rocks, exhumation and deformation, ultimately forming a syntaxis.

For a given crust, it may have a Type D zone, which is determined by its thermal structure (Figure 7). In addition, a certain degree of regional tectonic compression (or crustal shortening) and precipitation, including the resultant erosion, are also necessary. During the orogenesis, regional tectonic compression sets the initial conditions by raising Earth's surface. If moisture is transported into the region by the prevailing winds, it will lead to longitudinal (perpendicular to the strike of the mountain range) localization of precipitation (Anders et al., 2006; Berger & Spotila, 2008; Burbank et al., 2003; Reiners et al., 2003; Roe, 2005; Roe et al., 2002; Wratt et al., 2000) (Figure 15 path A, Figure 10a). At the same time, precipitation is also influenced by other factors such as latitude, continentality, and topographic features (Barry, 2008), which can lead to spatial heterogeneity of precipitation in the direction parallel to the strike of the mountain range, namely lateral localization of precipitation (Anders et al., 2006; Bookhagen & Burbank, 2006) (Figure 15 path B). The superposition of these two effects will lead to point-like precipitation enhancement within mountain belts. If the average precipitation and convergence rate fall within the Type D zone, a sustained, stationary, localized and relatively rapid erosion process will be established on the windward flank (Figure 9). This will further induce sustained and rapid uplift of rocks, exhumation and deformation (Figure 9, Figure 11, Figure 15 path C), ultimately leading to the formation of a large-scale antiform. At the core area of the antiform, extreme relief, deep exhumation, intense deformation and steepening of the near-surface thermal gradient overlap spatially. Additionally, the crustal material may experience low-P-high-T metamorphism and decompression melting during rapid uplifting and exhumation (Booth et al., 2009; Booth et al., 2004; Koons et al., 2002; Koons et al., 2013; Zeitler, Meltzer, et al., 2001) (Figure 17). Here, "sustained" means that the formation of a mature syntaxis needs a certain amount of time. According to our modelling, this process takes several million years. During this period, the average precipitation and convergence rate need to remain relatively stable (not falling outside the Type D zone). "Stationary" and "localized" mean that the position of the intense erosion zone on the windward flank do not undergo significant changes (Figure 9, Figure 11). "Relatively rapid" means that the erosional efficiency cannot be too fast (which would rapidly flatten the topography) nor too slow (which would cause continuous of deformation towards the foreland basin and lead to the displacement of the position of the intense erosion zone). Instead, it should be moderate to allow the majority of the material entering the orogenic wedge "flows out" through the narrow erosional window (Figure 11, Figure 16), so that this state can be maintained relatively stable over the long term (several million years).

In this context, the process of rock uplift triggered by erosion is governed by the universal principle that natural systems have the tendency towards dynamic equilibrium (Hack, 1975). The dynamic equilibrium of an orogen can be expressed as relatively stable states of material flux, topography, geotherm and exhumation (Willett & Brandon, 2002). In essence, it's about the equilibrium of temperature and pressure within the orogenic system. Rapid erosion can cause perturbations in the orogenic system, resulting in imbalances in temperature and pressure. To achieve a new state of equilibrium, the orogen will respond to the perturbations by undergoing rapid uplift, exhumation, deformation and steepening of geothermal gradients. Satellite rainfall estimates indicate that heaviest rainfall amounts within Himalayas occur closer to the major moisture source, the two ends of the Himalayan arc (Anders et al., 2006; Bookhagen & Burbank, 2006). Such precipitation localization effect might have resulted in the average precipitation and convergence rates at two ends of the Himalayan arc falling within their Type D zones, thereby promoting the development of syntaxes. The east-west rainfall gradient in the Himalayas is mainly influenced by the shape of Indian subcontinent, which has contributed to its stability since the onset of the Indian and east Asian monsoons (8-9 Ma) (Zhisheng et al., 2001). Meanwhile, the shortening rate of the Himalayas has remained relatively stable since 40 Ma

(Guillot et al., 2003), providing relatively stable tectonic and climatic conditions for the development of a mature syntaxis.

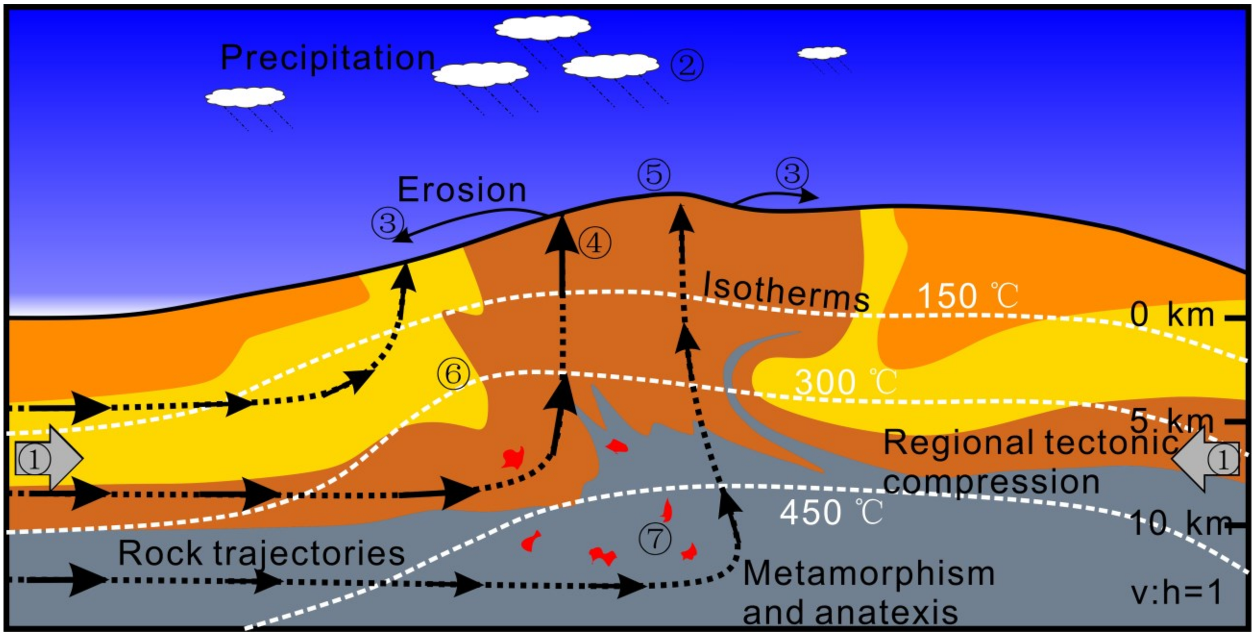

Figure 16. Geologic manifestation of a mature syntaxis. Once the convergence rate(①) and the average precipitation(②) fall within the Type D zone determined by the thermal structure of shallow crust, the formation process of a syntaxis will be initiated. Subsequently, a sustained, stationary, localized and relatively rapid erosion process(③) will be established on the windward flank of the orogenic wedge. This erosion process further induces sustained and rapid uplift of rocks, deep exhumation and intense deformation(④) within the intense erosion zone, forming large-scale antiform. Within the core of the antiform, extreme relief(⑤), deep exhumation, intense deformation and steepning of the near-surface thermal gradient(⑥) overlap spatially. During rapid uplifting and exhumation, crustal material may experience low-P-high-T metamorphism and decompression melting(⑦).

In model S034 and other type D models, there are no obvious low-viscosity channels observed near the intense erosion zone on the windward flank of the orogenic wedge (Figure 11). Therefore, we suspect that the positive feedback among erosion, heat advection, rock strength and deformation may not be necessary during the development of syntaxis. However, strain concentration and steepening of geothermal gradients will inevitably reduce rock viscosity in some degree (Ranalli, 1995; Turcotte & Schubert, 2014) so that the positive feedback is theoretically possible (Koons et al., 2002; Yang et al., 2023). In our models, the positive feedback was not observed possibly due to our model simplifications.

The complex interplay among climate, tectonics and surface processes in the orogen implies that orogen is best viewed as complex open system controlled by multiple factors (Pinter & Brandon, 1997). The system always evolves towards dynamic equilibrium and responds to changes in controlling factors in order to achieve a new state of equilibrium (Molnar, 2009). The response of the orogenic system to a specific factor also depends on the other controlling factors. Therefore, the evolution of an orogen is determined by a series of controlling factors (system inputs), none of which can be considered as the sole cause of the system's outcome. In mountain belts, once the convergence rate and the average precipitation fall within the Type D zone determined by the crustal thermal structure, syntaxis becomes the inevitable system's outcome under various physical laws, including conservation of mass, momentum and energy, rheology, orographic precipitation, surface processes, etc.

5 Conclusions

We presented results from numerical experiments that explore the interactions between climate, tectonics and surface processes, as well as the formation conditions and mechanisms of the eastern Himalayan syntaxis. In this study, we have tested three crucial controlling parameters: the convergence rate, average precipitation and initial geothermal gradient. Combined with field observations, we draw the following conclusions:

1. For a specific orogenic wedge, its tectonic and topographic evolution primarily relies on the relative strength of tectonic and climatic forces, rather than their respective magnitudes. When the tectonic forces are relatively stronger, the orogenic wedge tends to broaden, increase in elevation, and develop thrust faults. Conversely, when the tectonic forces are relatively weaker, the orogenic wedge tends to narrow, decrease in elevation, and develop folds.
2. For a specific orogenic wedge, there may exist a Type D zone in the in the $P_0 - v_c$ parameter space. This Type D zone is determined by the thermal structure of the crust, and its presence is the necessary condition for the development of a syntaxis.
3. Orogens are best viewed as complex open systems controlled by multiple factors. A syntaxis is the result of the combined effects of tectonic forces, climatic forces and geothermal field. In mountain belts, once the convergence rate and the average precipitation fall within the Type D zone, syntaxis becomes the inevitable system's outcome under various physical laws, including conservation of mass, momentum and energy, rheology, orographic precipitation, surface processes, etc.

Acknowledgments

This research has been funded by the National Natural Science Foundation of China (Grants Nos. 40472100, and 41472175). We are indebted to Prof. Taras Gerya for generously sharing the finite difference code used for thermo-mechanical calculations. We also express our gratitude to Daniel E. J. Hobley, Katherine R. Barnhart and their team for granting us access to landlab software for landscape evolution modelling.

Data Availability Statement

The finite difference code used for thermo-mechanical calculations can be found at www.cambridge.org/gerya2e. The landlab source code is found at https://github.com/landlab/landlab. Figures are plotted by MATLAB and Python.

References

Anders, A. M., Roe, G. H., Hallet, B., Montgomery, D. R., Finnegan, N. J., & Putkonen, J. (2006). Spatial patterns of precipitation and topography in the Himalaya. *Special Papers-Geological Society of America*, *398*, 39.

Avouac, J.-P., & Burov, E. (1996). Erosion as a driving mechanism of intracontinental mountain growth. *Journal of Geophysical Research: Solid Earth*, *101*(B8), 17747-17769.

Bahadori, A., Holt, W. E., Feng, R., Austermann, J., Loughney, K. M., Salles, T., . . . Flesch, L. M. (2022). Coupled influence of tectonics, climate, and surface processes on landscape evolution in southwestern North America. *Nature communications*, *13*(1), 4437.

Barnhart, K. R., Glade, R. C., Shobe, C. M., & Tucker, G. E. (2019). Terrainbento 1.0: a Python package for multi-model analysis in long-term drainage basin evolution. *Geoscientific Model Development*, *12*(4), 1267-1297.

Barnhart, K. R., Hutton, E. W., Tucker, G. E., Gasparini, N. M., Istanbulluoglu, E., Hobley, D. E., . . . Adams, J. M. (2020). Landlab v2. 0: A software package for Earth surface dynamics. *Earth Surface Dynamics*, *8*(2), 379-397.

Barros, A. P., & Lettenmaier, D. P. (1994). Dynamic modeling of orographically induced precipitation. *Reviews of geophysics*, *32*(3), 265-284.

Barry, R. (2008). Mountain weather and climate. Cambridge University Press. *New York*.

Beaumont, C., Jamieson, R. A., Nguyen, M., & Lee, B. (2001). Himalayan tectonics explained by extrusion of a low-viscosity crustal channel coupled to focused surface denudation. *Nature*, *414*(6865), 738-742.

Beaumont, C., Jamieson, R. A., Nguyen, M. H., & Medvedev, S. (2004). Crustal channel flows: 1. Numerical models with applications to the tectonics of the Himalayan‐Tibetan orogen. *Journal of Geophysical Research: Solid Earth*, *109*(B6).

Bendick, R., & Ehlers, T. A. (2014). Extreme localized exhumation at syntaxes initiated by subduction geometry. *Geophysical Research Letters*, *41*(16), 5861-5867.

Berger, A. L., Gulick, S. P., Spotila, J. A., Upton, P., Jaeger, J. M., Chapman, J. B., . . . Willems, B. A. (2008). Quaternary tectonic response to intensified glacial erosion in an orogenic wedge. *Nature geoscience*, *1*(11), 793-799.

Berger, A. L., & Spotila, J. A. (2008). Denudation and deformation in a glaciated orogenic wedge: The St. Elias orogen, Alaska. *Geology*, *36*(7), 523-526.

Bookhagen, B., & Burbank, D. W. (2006). Topography, relief, and TRMM‐derived rainfall variations along the Himalaya. *Geophysical Research Letters*, *33*(8).

Booth, A. L., Chamberlain, C. P., Kidd, W. S., & Zeitler, P. K. (2009). Constraints on the metamorphic evolution of the eastern Himalayan syntaxis from geochronologic and petrologic studies of Namche Barwa. *Geological Society of America Bulletin*, *121*(3-4), 385-407.

Booth, A. L., Zeitler, P. K., Kidd, W. S., Wooden, J., Liu, Y., Idleman, B., . . . Chamberlain, C. P. (2004). U-Pb zircon constraints on the tectonic evolution of southeastern Tibet, Namche Barwa area. *American journal of Science*, *304*(10), 889-929.

Bracciali, L., Parrish, R. R., Najman, Y., Smye, A., Carter, A., & Wijbrans, J. R. (2016). Plio-Pleistocene exhumation of the eastern Himalayan syntaxis and its domal 'pop-up'. *Earth-Science Reviews*, *160*, 350-385.

Buiter, S. J. (2012). A review of brittle compressional wedge models. *Tectonophysics*, *530*, 1-17.

Burbank, D., Blythe, A., Putkonen, J., Pratt-Sitaula, B., Gabet, E., Oskin, M., . . . Ojha, T. (2003). Decoupling of erosion and precipitation in the Himalayas. *Nature*, *426*(6967), 652-655.

Burg, J.-P., Nievergelt, P., Oberli, F., Seward, D., Davy, P., Maurin, J.-C., . . . Meier, M. (1998). The Namche Barwa syntaxis: evidence for exhumation related to compressional crustal folding. *Journal of Asian Earth Sciences*, *16*(2-3), 239-252.

Burg, J.-P., & Podladchikov, Y. (1999). Lithospheric scale folding: numerical modelling and application to the Himalayan syntaxes. *International Journal of Earth Sciences*, *88*(2), 190-200.

Burg, J.-P., & Schmalholz, S. (2008). Viscous heating allows thrusting to overcome crustal-scale buckling: Numerical investigation with application to the Himalayan syntaxes. *Earth and Planetary Science Letters*, *274*(1-2), 189-203.

Burg, J. P., Davy, P., Nievergelt, P., Oberli, F., Seward, D., Diao, Z., & Meier, M. (1997). Exhumation during crustal folding in the Namche‐Barwa syntaxis. *Terra Nova*, *9*(2), 53-56.

Butler, R. W. (2019). Tectonic evolution of the Himalayan syntaxes: the view from Nanga Parbat. *Geological Society, London, Special Publications*, *483*(1), 215-254.

Butler, R. W. H., Casey, M., Lloyd, G. E., Bond, C. E., McDade, P., Shipton, Z., & Jones, R. (2002). Vertical stretching and crustal thickening at Nanga Parbat, Pakistan Himalaya: a model for distributed continental deformation during mountain building. *Tectonics*, *21*(4), 9-1-9-17.

Champagnac, J. D., Molnar, P., Sue, C., & Herman, F. (2012). Tectonics, climate, and mountain topography. *Journal of Geophysical Research: Solid Earth*, *117*(B2).

Champagnac, J. D., Valla, P. G., & Herman, F. (2014). Late-Cenozoic relief evolution under evolving climate: A review. *Tectonophysics*, *614*(1), 44-65.

Clift, P. D., Pandey, D. K., & Kulhanek, D. K. (2020). Climate–tectonic interactions in the eastern Arabian Sea. *Geological Magazine*, *157*(6), 829-833.

Crameri, F., Schmeling, H., Golabek, G., Duretz, T., Orendt, R., Buiter, S., . . . Tackley, P. (2012). A comparison of numerical surface topography calculations in geodynamic modelling: an evaluation of the 'sticky air'method. *Geophysical Journal International*, *189*(1), 38-54.

Craw, D., Koons, P., Zeitler, P., & Kidd, W. (2005). Fluid evolution and thermal structure in the rapidly exhuming gneiss complex of Namche Barwa–Gyala Peri, eastern Himalayan syntaxis. *Journal of Metamorphic Geology*, *23*(9), 829-845.

Cruz, L., Malinski, J., Wilson, A., Take, W., & Hilley, G. (2010). Erosional control of the kinematics and geometry of fold‐and‐thrust belts imaged in a physical and numerical sandbox. *Journal of Geophysical Research: Solid Earth*, *115*(B9).

Culling, W. (1963). Soil creep and the development of hillside slopes. *The Journal of Geology*, *71*(2), 127-161.

Dadson, S. J., Hovius, N., Chen, H., Dade, W. B., Hsieh, M.-L., Willett, S. D., . . . Stark, C. P. (2003). Links between erosion, runoff variability and seismicity in the Taiwan orogen. *Nature*, *426*(6967), 648-651.

Dahlen, F. (1990). Critical taper model of fold-and-thrust belts and accretionary wedges. *Annual Review of Earth and Planetary Sciences*, *18*(1), 55-99.

Dahlen, F., Suppe, J., & Clark, S. (1988). Mechanics, growth, and erosion of mountain belts. *Processes in continental lithospheric deformation*, *218*, 161-178.

Davy, P., & Lague, D. (2009). Fluvial erosion/transport equation of landscape evolution models revisited. *Journal of Geophysical Research: Earth Surface*, *114*(F3).

Ding, L., Zhong, D., Yin, A., Kapp, P., & Harrison, T. M. (2001). Cenozoic structural and metamorphic evolution of the eastern Himalayan syntaxis (Namche Barwa). *Earth and Planetary Science Letters*, *192*(3), 423-438.

Egholm, D., Nielsen, S., Pedersen, V., & Lesemann, J.-E. (2009). Glacial effects limiting mountain height. *Nature*, *460*(7257), 884-887.

Emanuel, K. A. (1994). *Atmospheric convection*. Oxford University Press on Demand.

Enkelmann, E., Ehlers, T., Zeitler, P., & Hallet, B. (2011). Denudation of the Namche Barwa antiform, eastern Himalaya. *Earth and Planetary Science Letters*, *307*(3-4), 323-333.

Fernandes, N. F., & Dietrich, W. E. (1997). Hillslope evolution by diffusive processes: The timescale for equilibrium adjustments. *Water Resources Research*, *33*(6), 1307-1318.

Finnegan, N. J., Hallet, B., Montgomery, D. R., Zeitler, P. K., Stone, J. O., Anders, A. M., & Yuping, L. (2008). Coupling of rock uplift and river incision in the Namche Barwa–Gyala Peri massif, Tibet. *Geological Society of America Bulletin*, *120*(1-2), 142-155.

Gerya, T. (2019). *Introduction to numerical geodynamic modelling*. Cambridge University Press.

Gong, J., Ji, J., Zhou, J., Tu, J., Sun, D., Zhong, D., & Han, B. (2015). Late Miocene thermal evolution of the eastern Himalayan syntaxis as constrained by biotite 40Ar/39Ar thermochronology. *The Journal of Geology*, *123*(4), 369-384.

Grujic, D., Coutand, I., Bookhagen, B., Bonnet, S., Blythe, A., & Duncan, C. (2006). Climatic forcing of erosion, landscape, and tectonics in the Bhutan Himalayas. *Geology*, *34*(10), 801-804.

Guillot, S., Garzanti, E., Baratoux, D., Marquer, D., Mahéo, G., & de Sigoyer, J. (2003). Reconstructing the total shortening history of the NW Himalaya. *Geochemistry, Geophysics, Geosystems*, *4*(7).

Hack, J. T. (1957). *Studies of longitudinal stream profiles in Virginia and Maryland* (Vol. 294). US Government Printing Office.

Hack, J. T. (1975). Dynamic equilibrium and landscape evolution. *Theories of landform development*, *1*, 87-102.

Herman, F., Seward, D., Valla, P. G., Carter, A., Kohn, B., Willett, S. D., & Ehlers, T. A. (2013). Worldwide acceleration of mountain erosion under a cooling climate. *Nature*, *504*(7480), 423-426.

Hilley, G., Strecker, M., & Ramos, V. (2004). Growth and erosion of fold‐and‐thrust belts with an application to the Aconcagua fold‐and‐thrust belt, Argentina. *Journal of Geophysical Research: Solid Earth*, *109*(B1).

Hobley, D. E., Adams, J. M., Nudurupati, S. S., Hutton, E. W., Gasparini, N. M., Istanbulluoglu, E., & Tucker, G. E. (2017). Creative computing with Landlab: an open-source toolkit for building, coupling, and exploring two-dimensional numerical models of Earth-surface dynamics. *Earth Surface Dynamics*, *5*(1), 21-46.

King, G. E., Herman, F., & Guralnik, B. (2016). Northward migration of the eastern Himalayan syntaxis revealed by OSL thermochronometry. *Science*, *353*(6301), 800-804.

Koons, P. (1995). Modeling the topographic evolution of collisional belts. *Annual Review of Earth and Planetary Sciences*, *23*(1), 375-408.

Koons, P., Zeitler, P., Chamberlain, C., Craw, D., & Meltzer, A. (2002). Mechanical links between erosion and metamorphism in Nanga Parbat, Pakistan Himalaya. *American journal of Science*, *302*(9), 749-773.

Koons, P. O., Zeitler, P. K., & Hallet, B. (2013). Tectonic Aneurysms and Mountain Building. In J. F. Shroder (Ed.), *Treatise on geomorphology* (pp. 318-349). Academic Press. https://doi.org/https://doi.org/10.1016/B978-0-12-374739-6.00094-4

Koptev, A., Ehlers, T. A., Nettesheim, M., & Whipp, D. M. (2019). Response of a rheologically stratified lithosphere to subduction of an indenter‐shaped plate: Insights into localized exhumation at orogen syntaxes. *Tectonics*, *38*(6), 1908-1930.

Lin, T.-H., Lo, C.-H., Chung, S.-L., Hsu, F.-J., Yeh, M.-W., Lee, T.-Y., . . . Liu, D. (2009). 40Ar/39Ar dating of the Jiali and Gaoligong shear zones: Implications for crustal deformation around the Eastern Himalayan Syntaxis. *Journal of Asian Earth Sciences*, *34*(5), 674-685.

Liu, Y., & Zhong, D. (1997). Petrology of high‐pressure granulites from the eastern Himalayan syntaxis. *Journal of Metamorphic Geology*, *15*(4), 451-466.

Molnar, P. (2003). Nature, nurture and landscape. *Nature*, *426*(6967), 612-613.

Molnar, P. (2009). The state of interactions among tectonics, erosion, and climate: A polemic. *GSA Today*, *19*(7), 44-45.

Molnar, P., & England, P. (1990). Late Cenozoic uplift of mountain ranges and global climate change: chicken or egg? *Nature*, *346*(6279), 29-34.

Montgomery, D. R., & Dietrich, W. E. (1992). Channel initiation and the problem of landscape scale. *Science*, *255*(5046), 826-830.

Mukhopadhyay, B., Acharyya, A., Bhattacharyya, D., Dasgupta, S., & Pande, P. (2011). Seismotectonics at the terminal ends of the Himalayan arc. *Geomatics, Natural Hazards and Risk*, *2*(2), 159-181.

NASEM. (2020). *A vision for NSF Earth sciences 2020-2030: Earth in time*. National Academies Press.

Nettesheim, M., Ehlers, T. A., Whipp, D. M., & Koptev, A. (2018). The influence of upper-plate advance and erosion on overriding plate deformation in orogen syntaxes. *Solid Earth*, *9*(6), 1207-1224.

Norton, K., & Schlunegger, F. (2011). Migrating deformation in the Central Andes from enhanced orographic rainfall. *Nature communications*, *2*(1), 1-7.

Peizhen, Z., Molnar, P., & Downs, W. R. (2001). Increased sedimentation rates and grain sizes 2–4 Myr ago due to the influence of climate change on erosion rates. *Nature*, *410*(6831), 891-897.

Phillips, C. L., Parr, J. M., Riskin, E. A., & Prabhakar, T. (2003). *Signals, systems, and transforms*. Prentice Hall Upper Saddle River.

Pinter, N., & Brandon, M. T. (1997). How erosion builds mountains. *Scientific American*, *276*(4), 74-79.

Ranalli, G. (1995). *Rheology of the Earth*. Springer Science & Business Media.

Raymo, M. E., & Ruddiman, W. F. (1992). Tectonic forcing of late Cenozoic climate. *Nature*, *359*(6391), 117-122.

Reiners, P. W., Ehlers, T. A., Mitchell, S. G., & Montgomery, D. R. (2003). Coupled spatial variations in precipitation and long-term erosion rates across the Washington Cascades. *Nature*, *426*(6967), 645-647.

Roe, G. H. (2005). Orographic precipitation. *Annu. Rev. Earth Planet. Sci.*, *33*, 645-671.

Roe, G. H., Montgomery, D. R., & Hallet, B. (2002). Effects of orographic precipitation variations on the concavity of steady-state river profiles. *Geology*, *30*(2), 143-146.

Roe, G. H., Stolar, D. B., & Willett, S. D. (2006). Response of a steady-state critical wedge orogen to changes in climate and tectonic forcing. *Special Papers-Geological Society of America*, *398*, 227.

Roe, G. H., Whipple, K. X., & Fletcher, J. K. (2008). Feedbacks among climate, erosion, and tectonics in a critical wedge orogen. *American journal of Science*, *308*(7), 815-842.

Royden, L. H., Burchfiel, B. C., & van der Hilst, R. D. (2008). The geological evolution of the Tibetan Plateau. *Science*, *321*(5892), 1054-1058.

Ruh, J. B., Kaus, B. J., & Burg, J. P. (2012). Numerical investigation of deformation mechanics in fold‐and‐thrust belts: Influence of rheology of single and multiple décollements. *Tectonics*, *31*(3).

Schmeling, H., Babeyko, A., Enns, A., Faccenna, C., Funiciello, F., Gerya, T., . . . Morra, G. (2008). A benchmark comparison of spontaneous subduction models—Towards a free surface. *Physics of the Earth and Planetary Interiors*, *171*(1-4), 198-223.

Schulte-Pelkum, V., Monsalve, G., Sheehan, A., Pandey, M., Sapkota, S., Bilham, R., & Wu, F. (2005). Imaging the Indian subcontinent beneath the Himalaya. *Nature*, *435*(7046), 1222-1225.

Seward, D., & Burg, J.-P. (2008). Growth of the Namche Barwa Syntaxis and associated evolution of the Tsangpo Gorge: Constraints from structural and thermochronological data. *Tectonophysics*, *451*(1-4), 282-289.

Simpson, G. (2004). Role of river incision in enhancing deformation. *Geology*, *32*(4), 341-344.

Smith, R., & Barstad, I. (2004). A Linear Theory of Orographic Precipitation. *Journal of The Atmospheric Sciences - J ATMOS SCI*, *61*, 1377-1391. https://doi.org/10.1175/1520-0469(2004)061<1377:ALTOOP>2.0.CO;2

Song, Z., Zhenhan, W., Xitao, Z., Jianping, L., & Hua, W. (2012). Middle-Late Pleistocene Glacial Lakes in the Grand Canyon of the Tsangpo River, Tibet. *Acta Geologica Sinica - English Edition*, *86*(1), 266-283. https://doi.org/https://doi.org/10.1111/j.1755-6724.2012.00627.x

Steer, P., Simoes, M., Cattin, R., & Shyu, J. B. H. (2014). Erosion influences the seismicity of active thrust faults. *Nature communications*, *5*(1), 1-7.

Stewart, R., Hallet, B., Zeitler, P., Malloy, M., Allen, C. M., & Trippett, D. (2008). Brahmaputra sediment flux dominated by highly localized rapid erosion from the easternmost Himalaya. *Geology*, *36*(9), 711-714.

Stolar, D. B., Willett, S. D., & Roe, G. H. (2006). Climatic and tectonic forcing of a critical orogen. *Special Papers-Geological Society of America*, *398*, 241.

Tapponnier, P., Zhiqin, X., Roger, F., Meyer, B., Arnaud, N., Wittlinger, G., & Jingsui, Y. (2001). Oblique stepwise rise and growth of the Tibet Plateau. *Science*, *294*(5547), 1671-1677.

Tomkin, J. H., & Roe, G. H. (2007). Climate and tectonic controls on glaciated critical-taper orogens. *Earth and Planetary Science Letters*, *262*(3-4), 385-397.

Tu, J.-Y., Ji, J.-Q., Sun, D.-X., Gong, J.-F., Zhong, D.-L., & Han, B.-F. (2015). Thermal structure, rock exhumation, and glacial erosion of the Namche Barwa Peak, constraints from thermochronological data. *Journal of Asian Earth Sciences*, *105*, 223-233.

Turcotte, D., & Schubert, G. (2014). Geodynamics.

Valla, P. G., Sternai, P., & Fox, M. (2021). How climate, uplift and erosion shaped the Alpine topography. *Elements: An International Magazine of Mineralogy, Geochemistry, and Petrology*, *17*(1), 41-46.

Vogt, K., Matenco, L., & Cloetingh, S. (2017). Crustal mechanics control the geometry of mountain belts. Insights from numerical modelling. *Earth and Planetary Science Letters*, *460*, 12-21. https://doi.org/https://doi.org/10.1016/j.epsl.2016.11.016

Vogt, K., Willingshofer, E., Matenco, L., Sokoutis, D., Gerya, T., & Cloetingh, S. (2018). The role of lateral strength contrasts in orogenesis: A 2D numerical study. *Tectonophysics*, *746*, 549-561.

Wang, P., Scherler, D., Liu-Zeng, J., Mey, J., Avouac, J.-P., Zhang, Y., & Shi, D. (2014). Tectonic control of Yarlung Tsangpo Gorge revealed by a buried canyon in Southern Tibet. *Science*, *346*(6212), 978-981.

Whipp Jr, D. M., Beaumont, C., & Braun, J. (2014). Feeding the "aneurysm": Orogen‐parallel mass transport into Nanga Parbat and the western Himalayan syntaxis. *Journal of Geophysical Research: Solid Earth*, *119*(6), 5077-5096.

Whipple, K. X. (2009). The influence of climate on the tectonic evolution of mountain belts. *Nature geoscience*, *2*(2), 97-104.

Whipple, K. X. (2014). Can erosion drive tectonics? *Science*, *346*(6212), 918-919.

Whipple, K. X., & Meade, B. J. (2004). Controls on the strength of coupling among climate, erosion, and deformation in two‐sided, frictional orogenic wedges at steady state. *Journal of Geophysical Research: Earth Surface*, *109*(F1).

Whipple, K. X., & Meade, B. J. (2006). Orogen response to changes in climatic and tectonic forcing. *Earth and Planetary Science Letters*, *243*(1-2), 218-228.

Whipple, K. X., & Tucker, G. E. (1999). Dynamics of the stream‐power river incision model: Implications for height limits of mountain ranges, landscape response timescales, and research needs. *Journal of Geophysical Research: Solid Earth*, *104*(B8), 17661-17674.

Willett, S. D. (1999). Orogeny and orography: The effects of erosion on the structure of mountain belts. *Journal of Geophysical Research: Solid Earth*, *104*(B12), 28957-28981.

Willett, S. D. (2006). *Tectonics, climate, and landscape evolution* (Vol. 398). Geological Society of America.

Willett, S. D., & Brandon, M. T. (2002). On steady states in mountain belts. *Geology*, *30*(2), 175-178.

Willett, S. D., Schlunegger, F., & Picotti, V. (2006). Messinian climate change and erosional destruction of the central European Alps. *Geology*, *34*(8), 613-616.

Wolf, S. G., Huismans, R. S., Braun, J., & Yuan, X. (2022). Topography of mountain belts controlled by rheology and surface processes. *Nature*, 1-6.

Wratt, D., Revell, M., Sinclair, M., Gray, W., Henderson, R., & Chater, A. (2000). Relationships between air mass properties and mesoscale rainfall in New Zealand's Southern Alps. *Atmospheric Research*, *52*(4), 261-282.

Xiangjiang, W. F. J. J. Y., & Dalai, T. J. Z. (2017). Quantitative research on temporal and spatial coupling of precipitation potential energy and erosion intensity in Himalayas. *Chinese Journal of Geology*, *52*(1), 1-14.

Yang, J., Cao, W., Yuan, X., & Yang, J. (2023). Erosion-Driven Isostatic Flow and Crustal Diapirism: Analytical and Numerical Models With Implications for the Evolution of the Eastern Himalayan Syntaxis, Southern Tibet. *Tectonics*, *42*(8), e2022TC007717. https://doi.org/https://doi.org/10.1029/2022TC007717

Yang, R., Herman, F., Fellin, M. G., & Maden, C. (2018). Exhumation and topographic evolution of the Namche Barwa Syntaxis, eastern Himalaya. *Tectonophysics*, *722*, 43-52.

Yao, T., Li, Z., Yang, W., Guo, X., Zhu, L., Kang, S., . . . Yu, W. (2010). Glacial distribution and mass balance in the Yarlung Zangbo River and its influence on lakes. *Chinese Science Bulletin*, *55*(20), 2072-2078.

Ye, Y., Wu, L., Cowgill, E., Tian, Y., Lin, X., Xiao, A., & Chen, H. (2022). Long-lagged (~ 19 Myr) response of accelerated river incision to rock uplift on the northern margin of the Tibetan Plateau. *Earth and Planetary Science Letters*, *591*, 117608.

Yin, A. (2006). Cenozoic tectonic evolution of the Himalayan orogen as constrained by along-strike variation of structural geometry, exhumation history, and foreland sedimentation. *Earth-Science Reviews*, *76*(1-2), 1-131.

Yu, X., Ji, J., Gong, J., Sun, D., Qing, J., Wang, L., . . . Zhang, Z. (2011). Evidences of rapid erosion driven by climate in the Yarlung Zangbo (Tsangpo) Great Canyon, the eastern Himalayan syntaxis. *Chinese Science Bulletin*, *56*(11), 1123-1130. https://doi.org/10.1007/s11434-011-4419-x

Yu, X., Ji, J., Wang, F., & Zhong, D. (2017). Intensified climate-driven exhumation along the South Himalayan Front since one million years ago. *Journal of Asian Earth Sciences*, *136*, 50-57.

Yuan, X. P., Braun, J., Guerit, L., Rouby, D., & Cordonnier, G. (2019). A New Efficient Method to Solve the Stream Power Law Model Taking Into Account Sediment Deposition. *Journal of Geophysical Research: Earth Surface*, *124*(6), 1346-1365. https://doi.org/https://doi.org/10.1029/2018JF004867

Zeitler, P. K., Koons, P. O., Bishop, M. P., Chamberlain, C. P., Craw, D., Edwards, M. A., . . . Khattak, M. U. K. (2001). Crustal reworking at Nanga Parbat, Pakistan: Metamorphic consequences of thermal‐mechanical coupling facilitated by erosion. *Tectonics*, *20*(5), 712-728.

Zeitler, P. K., Meltzer, A. S., Brown, L., Kidd, W. S., Lim, C., & Enkelmann, E. (2014). Tectonics and topographic evolution of Namche Barwa and the easternmost Lhasa block, Tibet. In *Toward an improved understanding of uplift mechanisms and the elevation history of the Tibetan Plateau* (Vol. 507, pp. 23-58). Geological Society of America Special Papers.

Zeitler, P. K., Meltzer, A. S., Koons, P. O., Craw, D., Hallet, B., Chamberlain, C. P., . . . Bishop, M. (2001). Erosion, Himalayan geodynamics, and the geomorphology of metamorphism. *GSA Today*, *11*(1), 4-9.

Zhang, H., Hou, Z., Rolland, Y., & Santosh, M. (2022). The cold and hot collisional orogens: Thermal regimes and metallogeny of the Alpine versus Himalayan-Tibetan belts. *Ore Geology Reviews*, *141*, 104671.

Zhang, J., Ji, J., Zhong, D., Ding, L., & He, S. (2004). Structural pattern of eastern Himalayan syntaxis in Namjagbarwa and its formation process. *Science in China Series D: Earth Sciences*, *47*(2), 138-150.

Zhang, Z., Zhao, G., Santosh, M., Wang, J., Dong, X., & Liou, J. (2010). Two stages of granulite facies metamorphism in the eastern Himalayan syntaxis, south Tibet: Petrology, zircon geochronology and implications for the subduction of Neo‐Tethys and the Indian continent beneath Asia. *Journal of Metamorphic Geology*, *28*(7), 719-733.

Zhisheng, A., Kutzbach, J. E., Prell, W. L., & Porter, S. C. (2001). Evolution of Asian monsoons and phased uplift of the Himalaya–Tibetan plateau since Late Miocene times. *Nature*, *411*(6833), 62-66.

References From the Supporting Information

Anders, A. M., Roe, G. H., Hallet, B., Montgomery, D. R., Finnegan, N. J., & Putkonen, J. (2006). Spatial patterns of precipitation and topography in the Himalaya. *Special Papers-Geological Society of America*, *398*, 39.

Bittner, D., & Schmeling, H. (1995). Numerical Modelling of Melting Processes and Induced Diapirism In the Lower Crust. *Geophysical Journal International*, *123*(1), 59-70. https://doi.org/10.1111/j.1365-246X.1995.tb06661.x

Bookhagen, B., & Burbank, D. W. (2006). Topography, relief, and TRMM‐derived rainfall variations along the Himalaya. *Geophysical Research Letters*, *33*(8).

Burg, J.-P., & Gerya, T. V. (2005). The role of viscous heating in Barrovian metamorphism of collisional orogens: thermomechanical models and application to the Lepontine Dome in the Central Alps. *Journal of Metamorphic Geology*, *23*(2), 75-95. https://doi.org/https://doi.org/10.1111/j.1525-1314.2005.00563.x

Clauser, C., & Huenges, E. (1995). Thermal conductivity of rocks and minerals. *Rock physics and phase relations: a handbook of physical constants*, *3*, 105-126.

Gerya, T. (2019). *Introduction to numerical geodynamic modelling*. Cambridge University Press.

Gerya, T. V., & Yuen, D. A. (2003). Rayleigh–Taylor instabilities from hydration and melting propel 'cold plumes' at subduction zones. *Earth and Planetary Science Letters*, *212*(1), 47-62. https://doi.org/https://doi.org/10.1016/S0012-821X(03)00265-6

Pinkerton, H., & Stevenson, R. J. (1992). Methods of determining the rheological properties of magmas at sub-liquidus temperatures. *Journal of Volcanology and Geothermal Research*, *53*(1), 47-66. https://doi.org/https://doi.org/10.1016/0377-0273(92)90073-M

Ranalli, G. (1995). *Rheology of the Earth*. Springer Science & Business Media.

Schmidt, M. W., & Poli, S. (1998). Experimentally based water budgets for dehydrating slabs and consequences for arc magma generation. *Earth and Planetary Science Letters*, *163*(1), 361-379. https://doi.org/https://doi.org/10.1016/S0012-821X(98)00142-3

Turcotte, D., & Schubert, G. (2014). Geodynamics.

Numerical Modelling of Coupled Climate, Tectonics and Surface Processes on the Eastern Himalayan Syntaxis

Xueyun Lu[1], Jingtao Lai[2], Lining Wang[3,4], Jianqing Ji[1], Dalai Zhong[5]

[1]Key Laboratory of Orogenic Belts and Crustal Evolution, School of Earth and Space Sciences, Peking University, Beijing 100871, China

[2]Earth Surface Process Modelling, GFZ German Research Centre for Geosciences, 14473 Potsdam, Germany

[3]Research Institute of Petroleum Exploration & Development, PetroChina, Beijing 100083, China

[4]Key Laboratory of Basin Structure & Hydrocarbon Accumulation, CNPC, Beijing 100083, China

[5]Institute of Geology and Geophysics, Chinese Academy of Sciences, Beijing 100029, China

Corresponding author: Jianqing Ji (grsange@pku.edu.cn)

Key Points:

- A climatic-geomorphological-thermomechanical modelling technique is developed to investigate the evolution of orogenic wedges.
- The evolution of a specific orogenic wedge primarily relies on the relative strength of tectonic and climatic forces.
- The formation of the eastern Himalayan syntaxis results from the cooperation of tectonic forces, climatic forces and geothermal field.

Abstract

The interactions between climate, tectonics and surface processes have become a research hotspot in Earth science in recent years. Although various insights have been achieved, the relative importance of climatic and tectonic forcing in influencing the evolution of mountain belts still remains controversial. In order to investigate the tectonic and topographic evolution, as well as the formation mechanism of the eastern Himalayan syntaxis, we developed a comprehensive 2D climatic-geomorphological-thermomechanical numerical model and conducted over 200 experiments to test the influences of convergence rate, average precipitation and initial geothermal gradient on orogenic wedge. The results indicate that, for a specific orogenic wedge, its tectonic and topographic evolution primarily relies on the relative strength of tectonic and climatic forces, rather than their respective magnitudes. A syntaxis is the result of the combined effects of tectonic forces, climatic forces and geothermal field. In mountain belts, once the convergence rate and average precipitation fall within a Type D zone determined by the crustal thermal structure, a sustained, stationary, localized and relatively rapid erosion process will be established on the windward flank of the orogenic wedge. This will further induce sustained and rapid uplift of rocks, exhumation and deformation, ultimately forming a syntaxis. In this context, syntaxis is the inevitable system's outcome under various physical laws, including conservation of mass, momentum and energy, rheology, orographic precipitation, surface processes, etc. Orogens are best viewed as complex open systems controlled by multiple factors, none of which can be considered as the sole cause of the system's outcome.

Plain Language Summary

The eastern Himalayan syntaxis is essentially a large-scale antiform, where extreme relief, deep exhumation, intense deformation, and a steepening near-surface thermal gradient coincide in core areas. Despite its significance, the formation mechanism of this antiform still remains controversial. To investigate its formation mechanism, we developed a numerical model that integrates rock deformation processes, surface processes, and topography-dependent precipitation. We designed and conducted numerical experiments to investigate the influences of convergence rate, average precipitation and initial geothermal gradient on the evolution of an orogenic wedge. The results show that the tectonic and topographic evolution of an orogenic wedge, as well as the formation of the eastern Himalayan syntaxis, is the result of cooperation of tectonic compression, precipitation and geothermal field.

1 Introduction

The topography of collisional mountain ranges is controlled by both tectonics and climate: crustal thickening generates topography, while climate modulates surface processes and lowers mountain heights (Champagnac et al., 2012; Champagnac et al., 2014; Molnar, 2003; Molnar & England, 1990; Valla et al., 2021; Whipple, 2009; Willett, 2006). Much effort has been made to understand the mechanisms of the interactions between climate, tectonics and surface processes through various methods, including analytical treatment (Dahlen, 1990; Dahlen et al., 1988; Hilley et al., 2004; Roe et al., 2006; Roe et al., 2008; Tomkin & Roe, 2007; Whipple & Meade, 2006), numerical modelling (Avouac & Burov, 1996; Bahadori et al., 2022; Beaumont et al., 2001; Beaumont et al., 2004; Cruz et al., 2010; Koons et al., 2002; Simpson, 2004; Stolar et al., 2006; Willett, 1999; Wolf et al., 2022)and field observation (Berger et al., 2008; Clift et al., 2020; Gong et al., 2015; Grujic et al., 2006; Molnar & England, 1990; Norton & Schlunegger, 2011; Peizhen et al., 2001; Reiners et al., 2003; Steer et al., 2014; Tu et al., 2015; Willett et al., 2006; Ye et al., 2022; Zeitler, Koons, et al., 2001; Zeitler et al., 2014), and many important insights have been achieved (e.g.,NASEM, 2020; Whipple, 2009). For instance, previous researchers have found that the width and relief of a steady-state critical wedge are quantitatively related to precipitation and accretionary flux (Roe et al., 2006; Tomkin & Roe, 2007). Surface processes can influence the tectonic evolution of mountain belts by altering the distribution of mass on the surface and influencing gravitational stresses (Willett, 2006). Numerical modelling studies have demonstrated that erosion can promote localized crustal shortening and contribute to mountain growth (Avouac & Burov, 1996). Additionally, asymmetric rainfall intensity and erosional efficiency can lead to asymmetric development of the topography, deformation and exhumation (Willett, 1999). In the case of large, hot orogens like the Himalayan-Tibetan system, rapid erosion along the plateau margin can facilitate the extrusion of low-viscosity material from beneath the plateau (Beaumont et al., 2001).However, the relative importance of climatic and tectonic forcings in influencing the evolution of mountain belts is still debated (Burbank et al., 2003; Dadson et al., 2003; Herman et al., 2013; King et al., 2016; Molnar, 2003, 2009; Molnar & England, 1990; Pinter & Brandon, 1997; Raymo & Ruddiman, 1992; Wang et al., 2014; Whipple, 2009, 2014; Zeitler et al., 2014).

In the eastern Himalayan syntaxis, the intense tectonism, heavy precipitation, and ultra-fast surface processes make it an ideal natural laboratory for investigating the interactions among tectonics, climate, and surface processes (Bracciali et al., 2016; Gong et al., 2015; Tu et al., 2015; Yu et al., 2011). On the whole, the eastern Himalayan syntaxis is a large-scale antiform, in the core areas of which, extreme relief, deep exhumation, intense deformation and steepening of the near-surface thermal gradient overlap spatially (Burg et al., 1998; Butler, 2019; Koons et al., 2013; Zeitler et al., 2014). Various models have been proposed to illustrate its formation mechanism and structural evolution (Butler et al., 2002; Ding et al., 2001; Koons, 1995; Mukhopadhyay et al., 2011; Whipp Jr et al., 2014; Zeitler, Koons, et al., 2001). Classical models include northward indentation of Indian plate (Ding et al., 2001; Koons, 1995; Zhang et al., 2004), crustal and lithospheric scale folding under continental shortening (Burg et al., 1998; Burg & Podladchikov, 1999; Burg et al., 1997) and tectonic aneurysm (Koons et al., 2013; Zeitler, Koons, et al., 2001; Zeitler, Meltzer, et al., 2001). Concretely, the indentation model posits that syntaxis results from the northward indentation of the Indian continental indenter, while the crustal and lithospheric scale folding model believes that the large-scale antiform arises from lithospheric buckling, which is considered as a basic response to large-scale continental shortening. The tectonic aneurysm model attributes the development of the syntaxis to the positive feedbacks among erosion, heat advection, rock strength, and deformation. These models focus on different factors. For instance, the indentation model highlights the influences of plate geometry and rock strength, while the crustal and lithospheric scale folding model emphasizes the role of tectonic forces. The tectonic aneurysm model assigns a crucial role to climate and surface processes. Nevertheless, extensive research has demonstrated that climatic forces, tectonic forces and rock strength (crustal thermal structure) all play crucial roles in influencing the evolution of an orogenic wedge (Avouac & Burov, 1996; Beaumont et al., 2001; Buiter, 2012; Royden et al., 2008; Ruh et al., 2012; Tapponnier et al., 2001; Vogt et al., 2017; Vogt et al., 2018; Willett, 1999) , and their respective roles (regardless of magnitude) persist throughout the whole course of orogenesis. When evaluating the impact of one specific factor, it is essential to consider the other relevant factors as preconditions or assumptions. These models have different preconditions and assumptions, making comparison and testing among them challenging. Thus, further quantitative research on the feedback mechanisms and the relative importance of climate and tectonics is required.

To quantitatively investigate the interactions between climate, tectonics and surface processes, as well as the formation conditions and mechanisms of the eastern Himalayan syntaxis, we developed a comprehensive 2D climatic-geomorphological-thermomechanical numerical model and conducted a set of experiments to investigate the evolution of orogenic wedges under varying climatic, tectonic and geothermal conditions. Our results indicate that the formation of the eastern Himalayan syntaxis is the consequence of the combined effects of climatic forcing, tectonic forcing and crustal thermal structure (or rock strength).

2 Background

Located at the eastern end of Himalayan arc, the eastern Himalayan syntaxis is part of the Himalayan orogenic belt and essentially a special orogenic wedge (Yin, 2006). Compared to the central Himalayan arc, the eastern Himalayan syntaxis exhibits the following characteristics: (1)The overall structure exhibits a large-scale antiform (Burg et al., 1998; Burg et al., 1997). (2)A broad upwarp of the Moho beneath the Namche Barwa, with the crustal thickness in the core area of the syntaxis (55 km) appearing notably lower than the regional background crustal thickness (~70 km) (Zeitler et al., 2014). (3) Steep thermal gradients in upper crust (>50 ℃/km) (Craw et al., 2005). (4) Strong "bull's-eye" spatial localization of deformation (< ~50 km in diameter) (Bendick & Ehlers, 2014; Koons et al., 2013). (5) The thermochronological ages generally become younger with proximity to the Namche Barwa Peak (NBP), the core area of the syntaxis (Gong et al., 2015; King et al., 2016; Tu et al., 2015). (6) Rapid exhumation rate (>5 mm/yr)(Burg et al., 1997; Enkelmann et al., 2011; King et al., 2016; Stewart et al., 2008). (7) Extreme relief, intense climate and surface processes overlap in local area within the orogenic belt (Bookhagen & Burbank, 2006; Koons et al., 2013; Yu et al., 2017). Although the collision of India with Asia has been widely acknowledged to have occurred over 50 million years ago, many of the significant structures associated with the formation of the eastern Himalayan syntaxis only formed within the past 10 Myr (Butler, 2019; Zeitler et al., 2014).

2.1 Geological setting

The eastern Himalayan syntaxis is Cored by the Namche Barwa-Gyala Peri massif (NBGPM) and surrounded by the Lhasa terrane to the east, north, and west (Figure 1). In this region, the Lhasa terrane is mainly composed of high-grade metamorphic rocks, Cambrian–Eocene unmetamorphosed strata and numerous plutons (Gangdese granites) (Zhang et al., 2010). The core metamorphic massif primarily consists of meta-sedimentary greenschist-facies schists and amphibolite- to granulite-facies gneisses. These include garnet biotite schist, biotite epidote schist, sillimanite garnet biotite gneiss, biotite hornblende plagioclase gneiss, and biotite plagioclase amphibolites (Tu et al., 2015). High-pressure granulite-facies metamorphic rocks are predominantly exposed in the core area of the syntaxis, particularly near NBP (Booth et al., 2009; Ding et al., 2001; Liu & Zhong, 1997; Tu et al., 2015). According to Booth et al. (2009)'s study, the peak metamorphic pressures and temperatures within the core of the massif are estimated to be 10~14 kbar and 700~900 °C, respectively. Meanwhile, abundant young granitoids distribute in the region with the youngest age of only 0.9 Ma being reported (Zeitler et al., 2014). Geochemical analysis suggests that these young granites within the core of the massif predominantly originate from rapid depression melting of parent rocks (Booth et al., 2004; Koons et al., 2013).

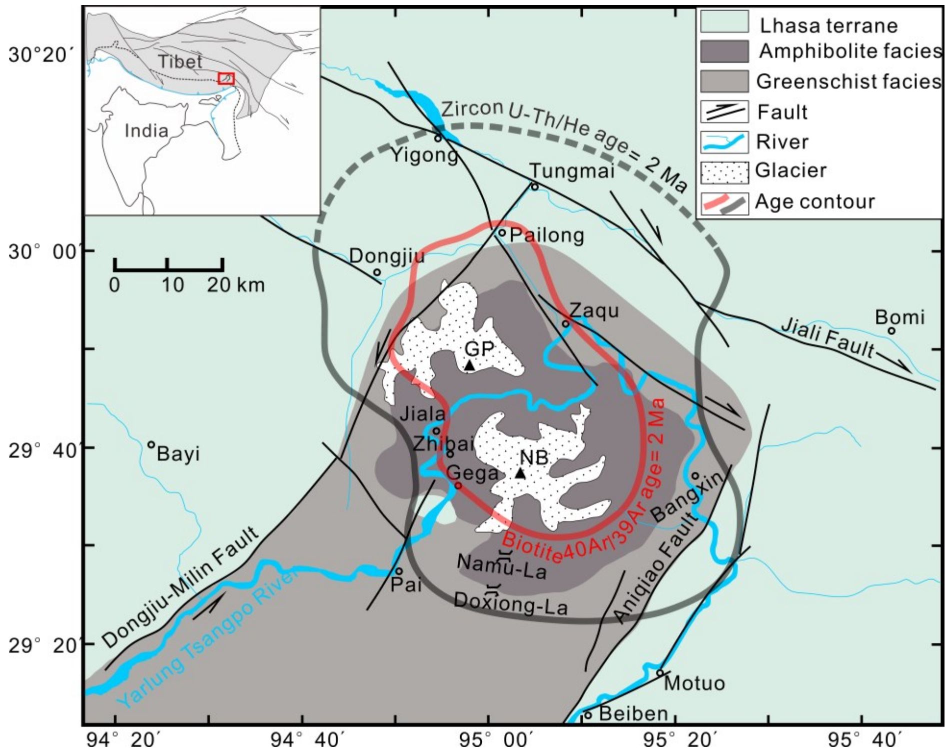

Figure 1. Geological sketch of the eastern Himalayan syntaxis showing the main geological units and structures (after Tu et al. (2015)). The inset in the top left corner illustrates the location of the eastern Himalayan syntaxis within the Himalayan-Tibetan orogenic belt. The bold black and red lines outline the areas with previously published young (<2 Ma) zircon U-Th/He and biotite 40Ar/39Ar ages, respectively (after Stewart et al. (2008)).

The overall structure of the eastern Himalayan syntaxis is a large NE-trending and N-plunging antiform (30 to 40 km wide), with its hinge lying near Doxiong-La (Burg et al., 1998; Burg et al., 1997; Ding et al., 2001). To the west of the syntaxis, the left-slip NE-trending Donjiu–Milin ductile fault zone defines its western boundary (Zhang et al., 2004), while the dip-slip NE-trending ductile Aniqiao fault zone is considered as its eastern bounding structure. To the north of the syntaxis lies the nearly E–W-trending Jiali ductile shear zone. The structural data suggests that this zone underwent a kinematic shift from left-slip to right-slip during its movement history (Lin et al., 2009). There are also a series of 290° - trending right-slip thrust fault zones and NE(or NW)-trending high-angle brittle normal faults in the syntaxis (Tu et al., 2015; Zhang et al., 2004).

2.2 Climate and geomorphology

Present climate data shows that the precipitation in the Tibetan Plateau is concentrated along the southern Himalayan topographic front, while the two ends of the Himalayan arc receive the highest amount of precipitation (Bookhagen & Burbank, 2006). According to the rainfall amounts estimated from TRMM (Tropical Rainfall Measurement Mission) satellite data, the annual average precipitation in the eastern Himalayan syntaxis region is currently around 2 m/yr, with maximum rainfall reaching up to 6 m/yr (Anders et al., 2006; Bookhagen & Burbank, 2006). In addition, the NBP and GPP (Gyala Peri Peak) are covered by massive modern glaciers, with the equilibrium line altitudes (ELAs) ranging between 4400 and 4500 m (Yao et al., 2010). The presence of abundant moraine deposits and outwash (with thickness ranging from 100 m to over 200 m) discovered at altitudes of 2900 to 4800 m at the foot of NBP also suggests that the eastern Himalayan syntaxis region has been subjected to significant glacial activities since Quaternary (Song et al., 2012).

The Yarlung Tsangpo River, the largest river in southern Tibet, flows parallel to the Himalayan orogenic belt for ~1700 km before entering the eastern Himalayan syntaxis, where it suddenly becomes narrow and deeply entrenched, creating one of the most spectacular gorges on the planet, the Yarlung Tsangpo Canyon. At the syntaxis, the river undergoes a rapid turn of ~180°, giving rise to a topographic relief of nearly 5 km within a horizontal distance of ~12 km. Then it flows southward, leaving the syntaxis (Finnegan et al., 2008; Yang et al., 2018). Under the influences of intense climate and tectonism, the eastern Himalayan syntaxis has developed distinct geomorphic features, including extreme local relief of over 4 km, steep topographic slopes and towering peak elevations that extend well above the ELA (Koons et al., 2013).

2.3 Thermochronology

The thermochronological ages in the eastern Himalayan syntaxis are relatively young (King et al., 2016). In this region, the published biotite 40Ar/39Ar are basically younger than 8 Ma (Gong et al., 2015; Stewart et al., 2008; Yu et al., 2011; Zhang et al., 2004). In the center of the metamorphic massif, some of the biotite 40Ar/39Ar ages can be as low as 0.2 and 0.4 Ma (Zeitler et al., 2014). The reported zircon fission track ages, zircon U-Th/He ages and apatite fission track ages are generally younger than 3 Ma (Burg et al., 1998; Stewart et al., 2008; Tu et al., 2015; Yu et al., 2011), while the youngest zircon fission track age and zircon U-Th/He age can be as low as 0.2 Ma and 0.2~0.3 Ma, respectively (Seward & Burg, 2008; Zeitler et al., 2014). In contrast, the thermochronological ages of the surrounding Lhasa terrane are relatively older (Gong et al., 2015; Zeitler et al., 2014). On the whole, the four types of thermochronological data mentioned above show a gradual decrease in age as they approach the core area of the syntaxis (Figure 1). All these data suggest rapid exhumation rates in this region. According to the P-T estimates , U-Pb and Th-Pb dating of metamorphic and anatectic phases, it is inferred that the long-term (since 5~10 Ma) exhumation rate in the core area of the syntaxis could reach 4~6 mm/yr or more, with total exhumation exceeding 20 km (Koons et al., 2013). Enkelmann et al. (2011) also reported decadal erosion rates of 5~17 mm/yr in the region based on the study of detrital zircon from the Brahmaputra River and tributaries.

3 Methodology

In this study, we use a coupled 2D climatic-geomorphological-thermomechanical modelling technique to simulate the crustal deformation, geothermal evolution, partial melting, fluvial erosion, sediment deposition, hillslope, and orographic precipitation in a compressional system.

3.1 Tectonic processes

In the thermomechanical model, the following continuity equation and stokes equation are employed to approximate the conservation of mass and momentum for 2D incompressible material in the gravitational field. The geothermal evolution of the system is modelled by solving the energy equations, which account for radioactive, shear, adiabatic and latent heat production.

Incompressible continuity equation:

$$\frac{\partial v_x}{\partial x}+\frac{\partial v_y}{\partial y}=0 \quad (1)$$

where v_x and v_y are horizontal and vertical velocity components, respectively.

2D stokes equation:

$$\frac{\partial \sigma'_{ij}}{\partial x_j}-\frac{\partial P}{\partial x_i}+\rho(C,P,T,M)g_i=0 \quad (2)$$

where i and j are coordinate indexes, x_j and x_i are spatial coordinates, σ'_{ij} is the deviatoric stress tensor, g_i is the ith component of the gravity vector, ρ is the density, which depends on the composition (C), pressure (P), temperature (T) and melt fraction (M).

Energy equations:

$$\rho C_p\frac{DT}{Dt}=-\frac{\partial q_i}{\partial x_i}+H_r+H_s+H_a+H_L \quad (3)$$

$$q_i=-k(C,T)\frac{\partial T}{\partial x_i} \quad (4)$$

$$H_a=T\alpha\frac{DP}{Dt} \quad (5)$$

$$H_s=\frac{{\sigma'_{xx}}^2}{\eta_{vp}}+\frac{{\sigma'_{xy}}^2}{\eta_{vp}} \quad (6)$$

where C_p is the effective isobaric heat capacity, $\frac{DT}{Dt}$ is the substantive time derivative of temperature, q_i is the heat flux components, H_r, H_s, H_a and H_L are the radioactive, shear, adiabatic and latent heat production, respectively. $k(C,T)$ is the composition- and temperature-dependent thermal conductivity, $\frac{DP}{Dt}$ is the substantive time derivative of pressure, α is the thermal expansion, η_{vp} is the effective visco-plastic viscosity. For details regarding the visco-elasto-plastic rheology of rocks, the partial melting model, and the material properties used in this study, readers are referred to Texts S1, S2, and Table S1 in Supporting Information S1.

3.2 Surface processes

Considering the code accessibility, feasibility and brevity, a landscape evolution model that accounts for the stream-power law (SPL) fluvial erosion, sediment deposition, hillslope, tectonic horizontal advection and vertical uplift is adopted (Barnhart et al., 2019; Culling, 1963; Davy & Lague, 2009):

$$\frac{\partial h}{\partial t}=\frac{VQ_s}{Q}-KQ^mS^n+K_s\nabla^2 h-\boldsymbol{v}\cdot\nabla h \quad (7)$$

where h is the topographic elevation, t is time, K_s is the 'topography diffusion' coefficient, K is the erodibility, m and n are the discharge and slope exponents, respectively. V is the effective settling velocity of the sediment particles, $\boldsymbol{v}$ is the material velocity vector at the surface. Q is volumetric water discharge, Q_s is volumetric sediment discharge. The volumetric sediment discharge at a specific downstream point ($Q_{s,out}$) is determined by integrating all the erosion minus deposition that has occurred upstream (Barnhart et al., 2019):

$$Q_{s,out}=\int_A\left([KQ^mS^n]_s-\left[\frac{VQ_{s,in}}{Q}\right]_s\right)dA \quad (8)$$

Here, the water discharge is calculated based on the orographic precipitation. It has been recognized that topography has a profound effect on the spatial patterns of precipitation (Roe, 2005; Roe et al., 2002; Smith & Barstad, 2004). Mountains can influence the flow of air and disturb the vertical stratification of the atmosphere by acting as physical barriers and sources or sinks of heat, thereby influencing the patterns of precipitation (Barros & Lettenmaier, 1994). At the space scale of mountain ranges (tens to hundreds of kilometers) and in the climatological average, the windward flank of the mountain range receives significantly higher precipitation compared to the leeward flank, forming the well-known rain shadow. Such precipitation localization effect is well observed in mountain ranges in today's climate across a wide range of latitudes, such as Southern Alps of New Zealand (Wratt et al., 2000), Himalayas (Bookhagen & Burbank, 2006; Burbank et al., 2003), Cascades mountains of Washington (Reiners et al., 2003) and St Elias Range of Alaska (Berger & Spotila, 2008). Here, following Anders et al. (2006)'s study, we assume that the precipitation in Himalayas is proportional to two factors. One is saturation vapor pressure at the surface, and the other is the saturation vapor pressure multiplied by the slope of the topography in the direction of the prevailing wind:

$$P = (\alpha_P + \beta_P S) e_{sat}(T) \quad (9)$$

where P is precipitation, α_P and β_P are constants, S is the topographic slope in the direction of the prevailing wind. $e_{sat}(T)$ is the saturation vapor pressure, and it can be estimated by the Clausius-Clapeyron relation (Emanuel, 1994):

$$e_{sat}(T) = 6.112 \exp\left(\frac{aT}{b+T}\right) \quad (10)$$

where $a = 17.67$, $b = 243.5$℃, T is the air temperature in degrees Celsius, and it is calculated using an average temperature at sea level (T_0, assumed to be 30℃) and a constant air temperature lapse rate (Γ, assumed to be -7 ℃/km), expressed as $T = T_0 + \Gamma h$.

Although its simplicity, this model captures the significant features of the pattern of the precipitation in Himalayas (Anders et al., 2006), and it's easy to implement and couple with landscape evolution models and thermomechanical models. According to the regression analysis by Anders et al. (2006), the values of α_P and β_P are approximately within the range of 0 to 1, and they are region-specific and scale-dependent, which indicates that there is no single set of values should be generally applicable. For details regarding the selection of these two parameters, readers are referred to Text S3 and Figure S1 in Supporting Information S1.

3.3 Numerical model design

The initial model domain extends 31 km in the Y direction and varies from 600 to 1000 km in the X direction depending on the total shortening amount (Figure 2a). To simulate the topographic evolution, the top 20 km of the model domain is set as "sticky air" layer with viscosity of 10^{18} $Pa\ s$ and density of 1 kg/m^3 (Crameri et al., 2012; Schmeling et al., 2008). Beneath the "sticky air" layer, the rightmost 100 km is set as a relatively rigid backstop, while the left part is composed of 11-km-thick undeformed visco-elasto-plastic rock sequence. Referring to the seismic reflection profile across Himalayas (Schulte-Pelkum et al., 2005) and some general profiles of fold-and-thrust belts or accretionary wedges on the planet (Buiter, 2012; Ruh et al., 2012), we assume that the initial thickness of the normal undeformed rock sequence is 10 km. Beneath this rock sequence, a 1-km-thick decollement layer is introduced to mimic the main decollement at the base of Himalayan orogenic wedge. This decollement layer is assumed to be frictional and has smaller compressive strength and internal friction coefficient compared to the normal rock sequence so that it's prone to plastic deformation (Ruh et al., 2012)(see material properties in Table S1 in Supporting Information S1). The model is solved by 401×81 non-uniform Eulerian nodes, with the finest initial resolution of 1 km×0.39 km in the proximity of the convergence center, and 8 million randomly distributed Lagrangian markers.

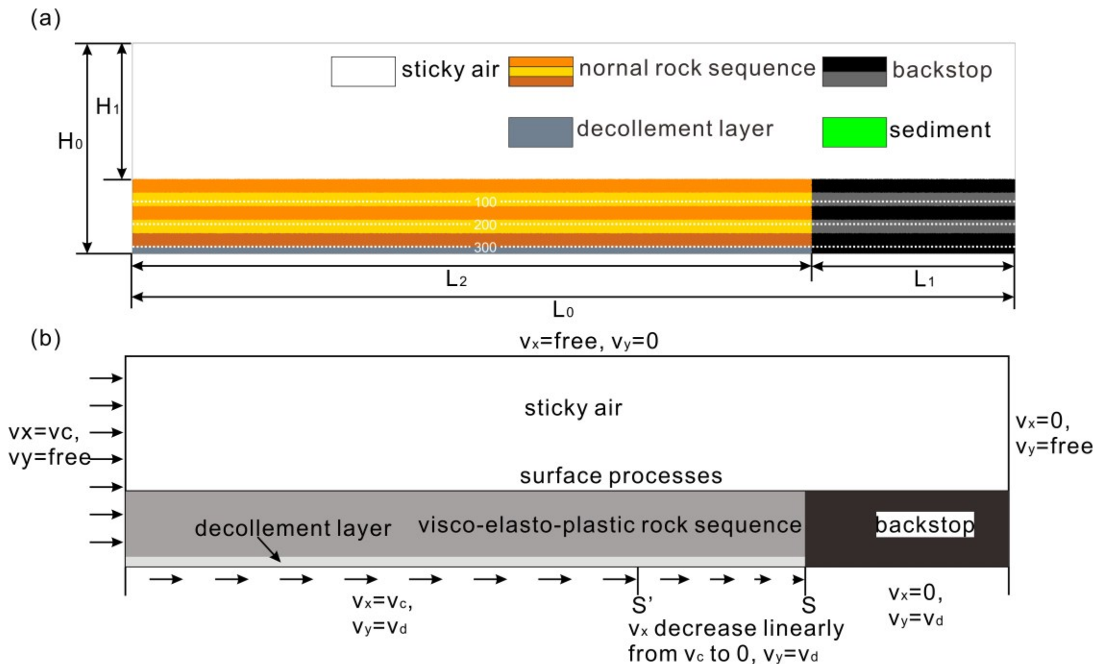

Figure 2. Model setup. (a) Initial model configuration. The definitions of each parameter can be found in Table 1. Different colors represent different rock types,with:white—sticky air; orange, yellow and brown—normal rock sequence; slategrey—decollement layer; grey and black—backstop; green—sediment. The sediment is not shown in Figure 3a, but will appear during the evolution of the model. The white dashed lines indicate isotherms (in °C). (b) Boundary conditions. v_c represents the convergence rate, and v_d is defined in the main text.

To simulate the mechanical environment at convergent plate boundary, a horizontal convergence velocity v_c (towards the right) is applied on the left boundary and the left portion of the lower boundary (Figure 2b), while the horizontal velocity on the right boundary and the right portion (right side of point S in Figure 2b) of the lower boundary is fixed at zero. To prevent abrupt velocity change, the horizontal velocity between S and S' at the lower boundary is assumed to decrease linearly from the convergence rate v_c to zero. In order to ensure mass conservation in the computational model, a vertical outward velocity $v_d = H * v_c/L$, which changes at every time step, is prescribed along the lower boundary. Here, H and L are the current height and width of the model, respectively. The upper boundary is free slip. All the experiments presented here share the same boundary conditions.

The thermal boundary conditions are 0 °C at the upper boundary and zero heat flux across the vertical boundaries. The temperature of the "sticky air" is consistent with temperature at the upper boundary. The temperature gradient at the lower boundary is fixed at the initial geothermal gradient dT/dh in order to ensure a relatively stable inward heat flux. The initial geothermal field is assumed to increase linearly from 0 °C at the surface to a specific bottom temperature, which varies depending on the initial geothermal gradient.

Table 1. Parameters used in the numerical experiments

Parameter	Description	Value
H_0	Height of the initial setup (km)	31
H_1	Thickness of the air (km)	20
L0	Initial length of the model (km)	600~1000
L_1	Length of backstop (km)	100
L_2	Length of rock sequence (km)	500~900
T_{top}	Temperature at model top (°C)	0
dT/dh	Initial thermal gradient (°C/km)	10~45 [a]
P_0	The average annual precipitation (m/yr)	0~20
v_c	Convergence rate (cm/yr)	0.5~5.0
T_0	Temperature at sea level in the model of orographic precipitation (°C)	30
Γ	The constant lapse rate in the model of orographic precipitation (°C/km)	-7.0
β_P	The coefficient in the model of orographic precipitation	0.370
V	effective settling velocity of the sediment particles (m/yr)	1.0 [b]
K	the erodibility in the stream-power incision model ($m^{-0.5}yr^{-0.5}$)	$2*10^{-5}$ [c]
m	The discharge exponent in the stream-power incision model	0.5 [c]
n	The slope exponent in the stream-power incision model	1.0 [c]
Ks	the 'topography diffusion' coefficient (m^2/yr)	0.035 [d]

Note. [a] Parameters from (Turcotte & Schubert, 2014). [b] Parameters from Yuan et al. (2019). [c] Parameters from Whipple and Tucker (1999). [d] Parameters from Fernandes and Dietrich (1997)

Given that many of the significant structures linked to the development of the eastern Himalayan syntaxis are younger than 10 Ma, we focus our research on the most recent 7 Myr, rather than the entire evolutionary history of the Himalayan-Tibetan orogenic belt since the onset of collision. The total model runtime is set to 8 Myr. The precipitation for the first 1 Myr is set to 0 m/yr to achieve a model state with a certain degree of deformation and relief. The orographic precipitation is applied after t=1 Myr, and for all the experiments, it's assumed that the direction of the prevailing winds is consistent with the direction of the subduction, which is from the left. By varying the convergence rate v_c, average precipitation P_0, and initial geothermal gradient dT/dh, which is related to the overall strength of the shallow crustal rock sequence, a total of 232 experiments are designed and conducted (Table S2, S3, and S4 in Supporting Information S1).

3.3 Numerical implementation

The thermomechanical processes are solved using the code provided by Gerya (2019), which uses a finite difference approach and a marker in cell technique to solve the thermal and mechanical equations mentioned above. The surface processes and orographic precipitation are implemented through landlab, an open-source package for numerical modelling of Earth surface dynamics (Barnhart et al., 2019; Barnhart et al., 2020; Hobley et al., 2017), and Python programming. We use a 3-by-N regular landlab grid with top and bottom edges as fixed zero gradient boundaries to simulate the evolution of a 1D model domain. We couple the thermomechanical model, surface processes model, and orographic precipitation model through the following steps. Firstly, the thermomechanical processes are solved using the finite difference code. This provides the current topography, which is then used to simulate the precipitation based on the orographic precipitation model. Subsequently, the surface processes are solved based on the topography and precipitation with smaller sub-time steps in landlab, after which the elevation changes due to surface processes can be determined. Based on these elevation changes and the thermomechanical velocity field, the topography in the model is updated. At the same time, if the rock types of the Lagrangian markers near the surface has changed, the corresponding field quantities are also updated. This process is repeated until the computation reaches the predetermined end time.

4 Results

4.1 Relative importance of tectonic and climatic forcings in controlling the evolution of orogenic wedge

The modelling results indicate that the convergence rate, average precipitation and initial geothermal gradient all have significant influences on the structural and geomorphic evolution of the orogenic wedge. For all the models depicted in Figure 3 and 4, the initial geothermal gradients are consistently set at 30 °C/km. When increasing the convergence rate and maintaining a constant average precipitation, it leads to an increase in the width and height of the orogenic wedge (Figure 3). Additionally, at relatively lower convergence rates, the orogenic wedge tends to develop folds or fault-related folds (Figure 3b), and for those models with sufficiently low convergence rates, the deformation structures and topography will be unable to withstand intense erosion and thus cannot be completely preserved (Figure 3a). As the convergence rate increases, the deformation style within the orogenic wedge gradually transitions to thrust faults, and the deformation continuously extends towards the foreland basin through developing imbricate structures (Figure 3c and d).

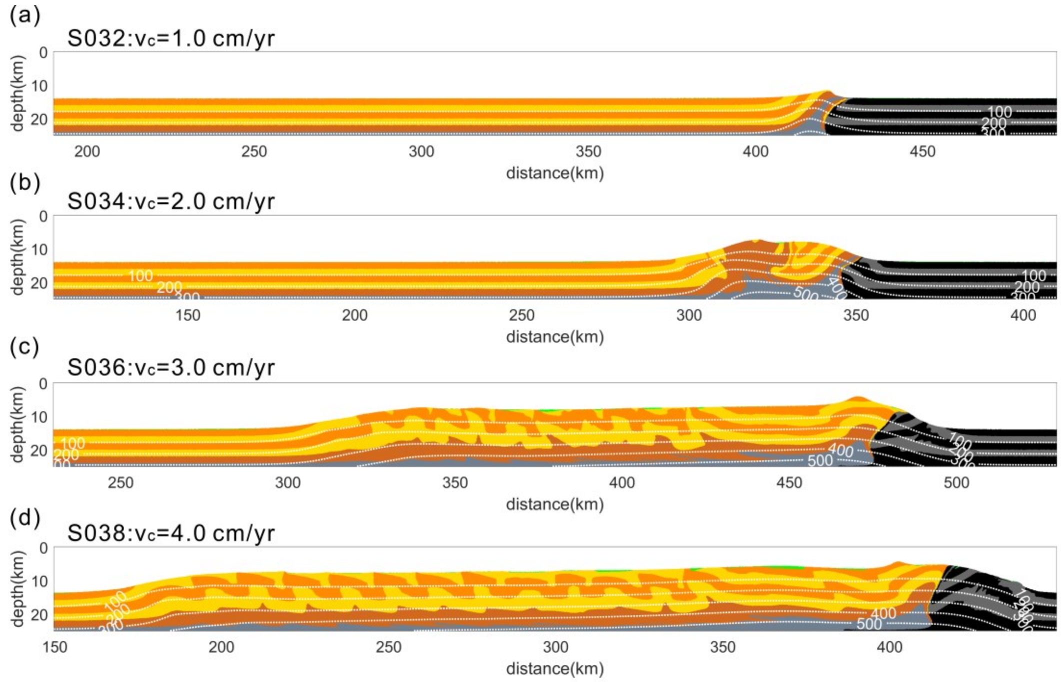

Figure 3. Numerical modelling results showing the influence of convergence rate(v_c) on the evolution of orogenic wedges. The white dashed lines indicate isotherms (in °C). For all models, the average precipitation(P_0) is 6 m/yr, the initial geothermal gradient(dT/dh) is 30 °C/km, and the runtime is 8 Myr. The convergence rates for (a), (b), (c) and (d) are 1.0 cm/yr, 2.0 cm/yr, 3.0 cm/yr and 4.0 cm/yr, respectively. The width and height of the orogenic wedge increase as the convergence rate increases, while keeping the average precipitation constant. At the same time, the rock deformation exhibits the tendency from folding toward imbricate thrusting.

The effect of increasing the average precipitation while fixing the convergence rate is opposite to that of increasing the convergence rate while keeping the average precipitation constant. When the convergence rate and initial geothermal gradient remain constant, increasing the average precipitation favors reducing the height and width of the orogenic wedge (Figure 4). At the same time, the deformation style within the orogenic wedge gradually transitions from thrusting to folding. Similarly, for models with sufficiently high average precipitation, the deformation structures will be quickly eroded, resulting in very low topography (Figure 4d and e). These findings suggest that the height, width, and deformation style of a specific orogenic wedge primarily rely on the relative strength of tectonic and climatic forces, rather than their respective magnitudes. When the tectonic forces are relatively stronger, the orogenic wedge tends to broaden, increase in elevation, and develop thrust faults. Conversely, when the tectonic forces are relatively weaker, the orogenic wedge tends to narrow, decrease in elevation, and develop folds.

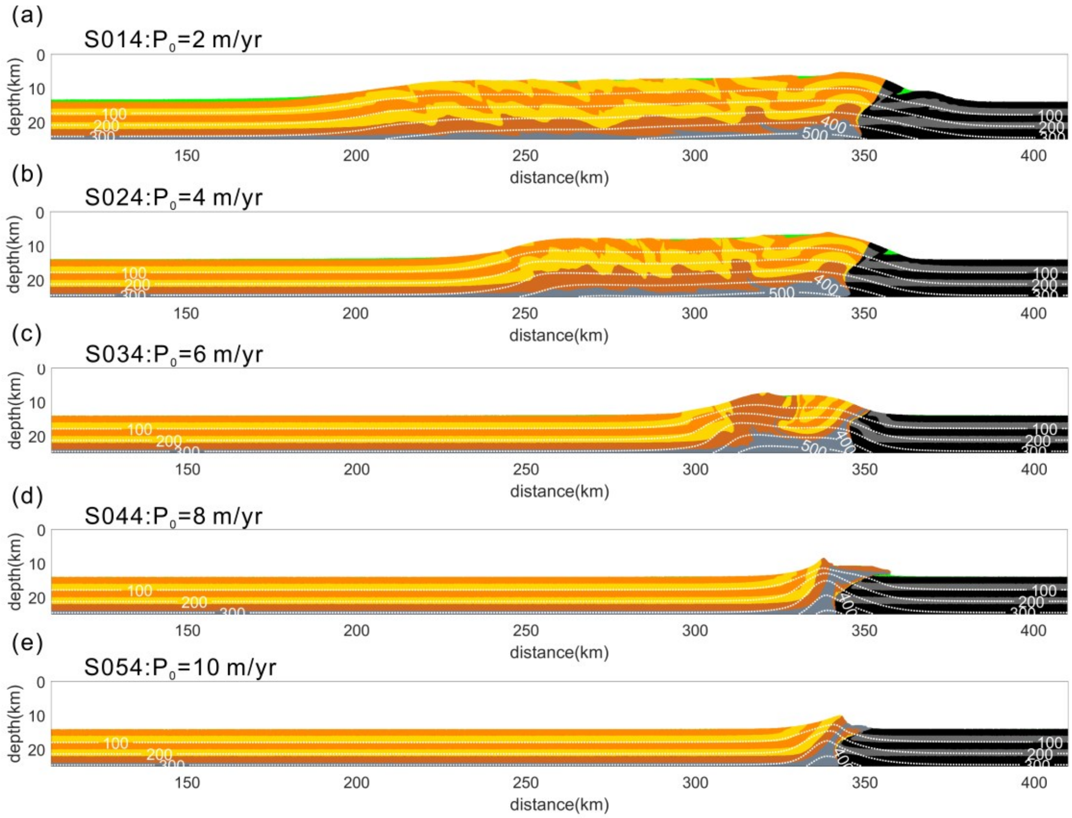

Figure 4. Numerical modelling results showing the influence of the average precipitation(P_0) on the evolution of orogenic wedges. The white dashed lines indicate isotherms (in ℃). For all models, the convergence rate(v_c) is 2.0 cm/yr, the initial geothermal gradient(dT/dh) is 30 ℃/km, and the runtime is 8 Myr. The average precipitations for (a), (b), (c), (d) and (e) are 2 m/yr, 4 m/yr, 6 m/yr, 8 m/yr and 10 m/yr, respectively. The width and height of the orogenic wedge decrease as the average precipitation increases, while keeping the convergence rate constant. At the same time, the rock deformation exhibits the tendency from imbricate thrusting toward folding.

Besides convergence rate and average precipitation, geothermal conditions also play a significant role in influencing the evolution of orogenic wedges. Since the geothermal gradients at the model's bottom boundary are set to remain consistent with the initial geothermal gradients, the initial geothermal gradient not only affects the initial geothermal field but also influences the heat flow at the bottom of the model. This means that increasing the initial geothermal gradient will enhance the overall geothermal field of the model, and vice versa. Our modelling results indicate that, under constant convergence rate and average precipitation, a gentler initial geothermal gradient favors developing wider orogenic wedge and higher topography. Additionally, it tends to promote the formation of imbricate structures (Figure 5a and b). Models with steeper initial geothermal gradients tend to develop narrower orogenic wedges and lower topographies, and the deformation style is dominated by folding (Figure 5c and d). In this context, increasing the initial geothermal gradient has a comparable effect to strengthening the relative dominance of climatic forces over tectonic forces, as both contribute to the softening of crustal rocks. This can be attributed to the former enhancing the overall geothermal field, while the latter can localize deformation and steepen geothermal gradients. These will elevate the temperature and strain rate of the rocks, leading to a decrease in viscosity, thereby weakening the rock strength.

Figure 5. Numerical modelling results showing the influence of the initial geothermal gradient(dT/dh) on the evolution of orogenic wedges. The white dashed lines indicate isotherms (in ℃). For all models, the convergence rate(v_c) is 2.0 cm/yr, the average precipitation (P_0) is 6 m/yr, and the runtime is 8 Myr. The initial geothermal gradients for (a), (b), (c) and (d) are 20 ℃/km, 25 ℃/km, 30 ℃/km and 35 ℃/km, respectively. The width and height of the orogenic wedge decrease as the initial geothermal gradient increases. At the same time, the rock deformation exhibits the tendency from imbricate thrusting toward folding.

4.2 Evolutionary regimes of orogenic wedges

Based on the relative dominance of tectonic and climatic forces, as well as the features of tectonic and topographic evolution, the modelling outcomes can be categorized into three basic types of orogenic wedge (or evolutionary regimes), which can be referred as type A, B and C (Figure 6). A type A orogenic wedge is dominated by climatic forces compared to tectonic forces (Figure 6a). The most typical feature of this type of orogenic wedge is the rapid obliteration of initial deformation structures and topography due to intense erosion before reaching a steady state. In most cases, this process occurs within approximately 3 Myr, although in a few cases the topography may persist for 5~6 Myr. During this phase, there can be rapid and significant variations in the structural and topographic characteristics. However, the ultimate tendency is towards topographic flattening, resulting in minimal preservation of deformation structures (Figure 3a, Figure 4d and e, Figure 5d). Once a steady state is reached, a type A orogenic wedge maintains a long-term stable equilibrium of material flux. Conversely, A type B orogenic wedge is dominated by tectonic forces compared to climatic forces (Figure 6b). In a type B orogenic wedge, the erosional efficiency is insufficient so that the erosional outflux cannot balance the tectonic influx. This results in continuous expansion of deformation towards the foreland basin, forming orogenic wedge with large size and high topography. A type B orogenic wedge does not attain a stable equilibrium of material flux, and its deformation style is dominated by imbricate thrusting.

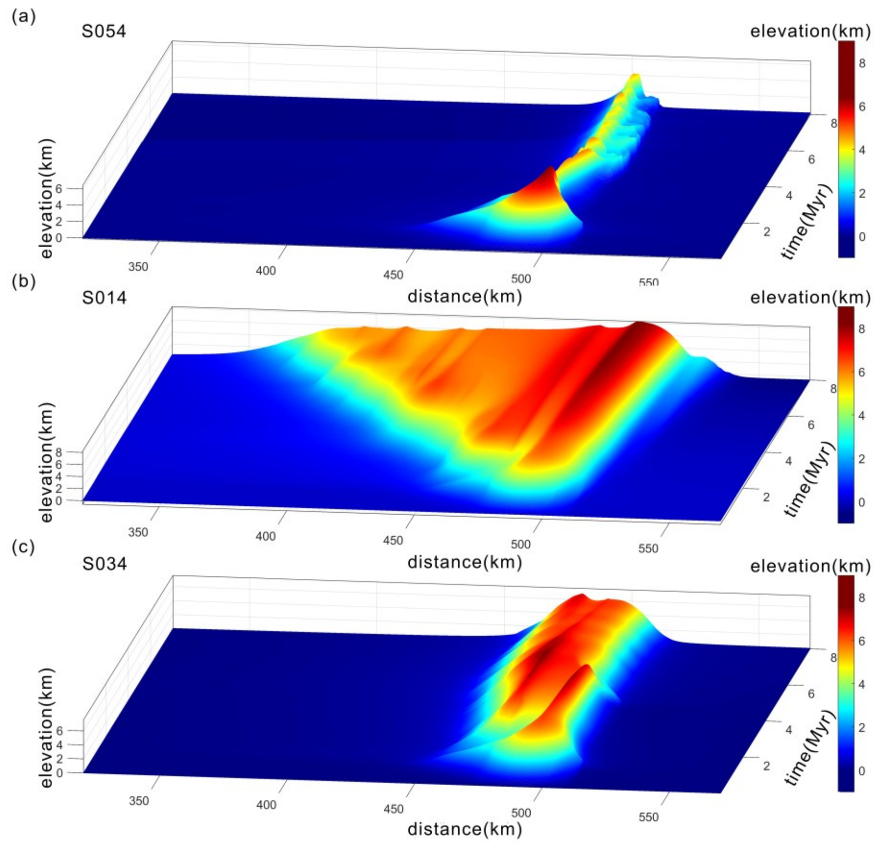

Figure 6. The geomorphic evolution of typical models of three basic types of orogenic wedge. (a) is the representative of type A orogenic wedge, which is dominated by the climatic forces. In this case, the width and height of the wedge shrink rapidly starting from t=1 Myr until the topography is almost entirely erased before reaching a steady state. (b) is the representative of type B orogenic wedge, which is dominated by the tectonic forces. In this case, the deformation continuously extends towards the foreland basin, leading to high topography and wider wedge. (c) is the representative of type C orogenic wedge, in which the climatic and tectonic forces exhibit comparable strength. In this case, the material flux reaches a steady state after a brief period of adjustment (around 1 Myr). Subsequently, the height, width and the topography of the wedge can remain relatively stable in the long-term time.

When the climatic and tectonic forces exhibit comparable strength, it gives rise to type C orogenic wedge (Figure 6c). In this case, the orogenic system is able to establish a dynamic equilibrium within a short period of time (around 1 Myr). In this state of equilibrium, the material flow field, width of the orogenic wedge, topography and deformation style of rocks can remain relatively stable in the long-term time (Figure 3b, Figure 4b, Figure 5b and c). In contrast to type A orogenic wedge, a type C orogenic wedge in a state of equilibrium retains a certain amount of deformation structures, resulting in a relatively larger size. The deformation style in a type C orogenic wedge is variable and it can manifest as either imbricate thrusting (Figure 5b) or folding (Figure 5c), depending on the shallow crustal geothermal field or other factors.

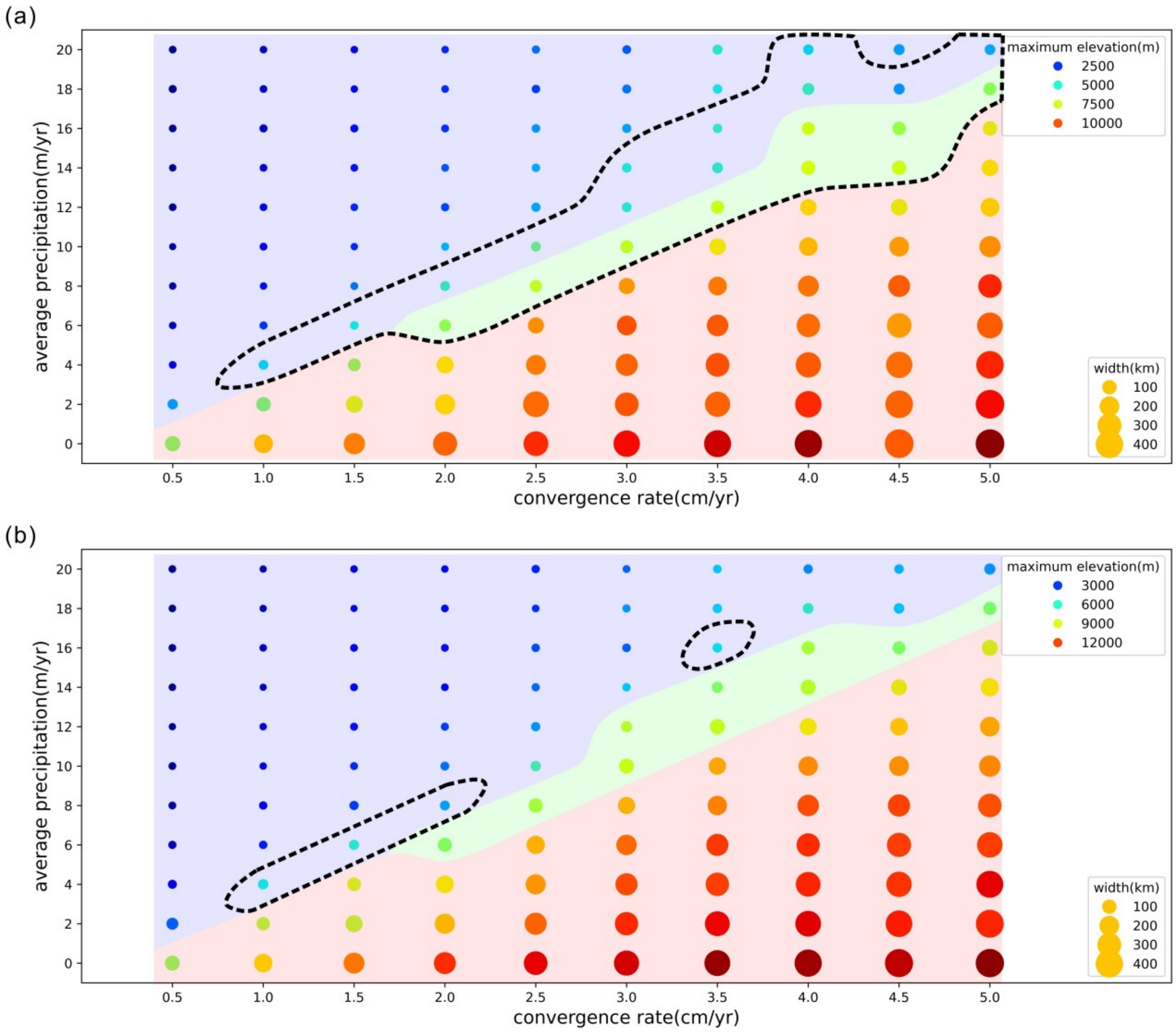

Figure 7. Orogenic wedge type as a function of convergence rate and average precipitation for cases with an initial geothermal gradient of 30 (a) and 25 (b) °C/km. Each point inside the diagrams represents one numerical experiment in Table S2 and S3 in Supporting Information S1. The color and size of each point indicate the maximum elevation and width of the orogenic wedge (at t=8 Myr), respectively. The regions marked in light blue, light red, and light green correspond to the orogenic wedges categorized as type A, B and C, respectively. Enclosed within the dashed circle are the models that exhibit similar structural features to the eastern Himalayan syntaxis (Type D zone). The distribution of type A, B and C orogenic wedges doesn't show significant variation when the initial geothermal gradient changes, but the Type D zone shrinks as the initial geothermal gradient decreases.

In the parameter space of the average precipitation and convergence rate, a certain regularity can be observed about the distribution of the three basic types of orogenic wedges (Figure 7). Irrespective of whether the initial geothermal gradient is 30 or 25 °C/km, type C orogenic wedges are primarily located near the line $P_0 = 4 \times v_c - 2$ (where P_0 is in units of m/yr, v_c is in units of cm/yr, and v_c > 1.5 cm/yr), while type A and type B orogenic wedges are distributed above and below this line, respectively. This distribution pattern remains relatively stable regardless of the variation in the initial geothermal gradient. This is reasonable because the three basic types of orogenic wedges are essentially the result of different relative strengths of tectonic and climatic forces, and this distribution pattern corresponds to different parameter ranges of different relative strengths between the two forces.

Figure 8. Typical models that exhibit similar structural features to the eastern Himalayan syntaxis. The white dashed lines indicate isotherms (in ℃). When the convergence rate, average precipitation and initial geothermal gradient fall within certain ranges, several significant structural features resembling those observed in the syntaxis will emerge within the orogenic wedge. At a particular geological time (t) during model evolution, sustained, stationary, and localized erosion induces localized rock uplift and deformation, forming large-scale antiforms. In the core areas of the antiforms, extreme relief, deep exhumation, intense deformation and steepening of the near-surface thermal gradient overlap spatially.

Among type A and type C orogenic wedges, we identified a fourth special type of orogenic wedge (referred as type D), which exhibits similar structural features to the eastern

Himalayan syntaxis at a particular geological time (Figure 8). When the convergence rate, average precipitation and initial geothermal gradient fall within certain ranges, it leads to the development of sustained, stationary, and localized erosion within the orogenic wedge. This further induces rapid uplift of rocks in a local area, forming large-scale antiforms. In the core areas of the antiforms, extreme relief, deep exhumation, intense deformation and steepening of the near-surface thermal gradient overlap spatially. These structural features closely approximate the field observations in the eastern Himalayan syntaxis region. However, for those orogenic wedges that belong to both type D and type A, such antiformal structures cannot be preserved for a very long time. Generally, they are completely destroyed within around 1 Myr after their formation, but for those belonging to both type D and type C, these structures can be sustained for a longer period (usually >2 Myr). Similar to type C orogenic wedges, the majority of the type D orogenic wedges conform to the condition of relatively balanced climatic and tectonic forces, but their distributions in the $P_0 - v_c$ parameter space do not align perfectly (Figure 7). Here we refer to the domain corresponding to type D orogenic wedges in the $P_0 - v_c$ parameter space as "Type D zone". Unlike the distribution pattern of the three basic types, the Type D zone is highly sensitive to the initial geothermal gradient, and it shrinks considerably when the initial geothermal gradient decreases from 30 to 25 °C/km. Moreover, it can be observed that the Type D zone tends to expand with an increase in the initial geothermal gradient or average precipitation increase (Figure 7). As discussed above, the increase in initial geothermal gradient and average precipitation promotes a decrease in effective viscosity of crustal rocks. This founding implies that the softening of the crustal rocks appears to favor the formation of syntaxes.

Our results indicate that the tectonic and topographic evolution of an orogenic wedge is the result of the combined effects of crustal shortening, precipitation, and geothermal field.

5 Discussion

5.1 Model limitations

The distribution pattern depicted in Figure 7 is related to the initial model configuration. It can be inferred that the distribution of different types of orogenic wedges in $P_0 - v_c$ parameter space may vary slightly if the initial model configuration, such as the rheology of the initial undeformed rock sequence, is altered. Therefore, it may not perfectly fit every similar numerical model or orogenic region. Nevertheless, the regularities revealed by regime diagram (Figure 7) are expected to exist in nature. Moreover, although the type D orogenic wedges closely match the field observations from the eastern Himalayan syntaxis in various aspects, some crucial features still haven't been reproduced in our simulation. For instance, although a simple partial melting model is included in our simulation, obvious partial melting of rocks is not observed in the type D orogenic wedges. Nevertheless, the depression melting process in the eastern Himalayan syntaxis since 10 Ma is widely recognized (Booth et al., 2009; Koons et al., 2013).This discrepancy is probably attributed to the simplifications in our initial model configuration, including simplified profile of rock sequence and thermal structure. The initial state of the eastern Himalayan syntaxis around 8 million years ago was more complex than we assumed.

For simplicity, we assume that the surface processes are fluvially-dominated. In other words, above the ELA, we substitute fluvial erosion for glacial erosion. This will inevitably introduce errors. Most of our modelling results, especially the type B orogenic wedges, exhibit peak elevations far exceeding the highest peak on Earth (8848 m) (Figure 7). This could be due to the absence of an accurate glacial erosion process in our models. Glaciers can limit mountain height through a distinct mechanism of erosion, known as glacial buzzsaw (Egholm et al., 2009). Therefore, coupled surface process model accounting for both fluvial and glacial activities is necessary for more accurate modelling of landscape evolution in the eastern Himalayan syntaxis region.

In order to simulate the co-evolution of topography and climate, we employed a simplified model for orographic precipitation (Equation 9). While this precipitation model can capture the primary characteristics of precipitation distribution in mountainous regions, it tends to overestimate the precipitation in the inland areas on the leeward side of the mountain ranges and leads to minor unrealistic erosion (Text S3 and Figure S1 in Supporting Information S1, Figure 9 and 10). In the future, constructing more realistic precipitation models could be a promising research direction.

Since orogenic wedges or syntaxes are three-dimensional in reality, the 2D geometry employed in this study renders the models inadequate for addressing a number of significant aspects of orogenic development, such as the growth of structures oriented parallel to plate boundaries, the development of possible strike-slip faults and the evolution of 2D topography, etc. Therefore, this work would be greatly improved if these geological processes are simulated in 3D models.

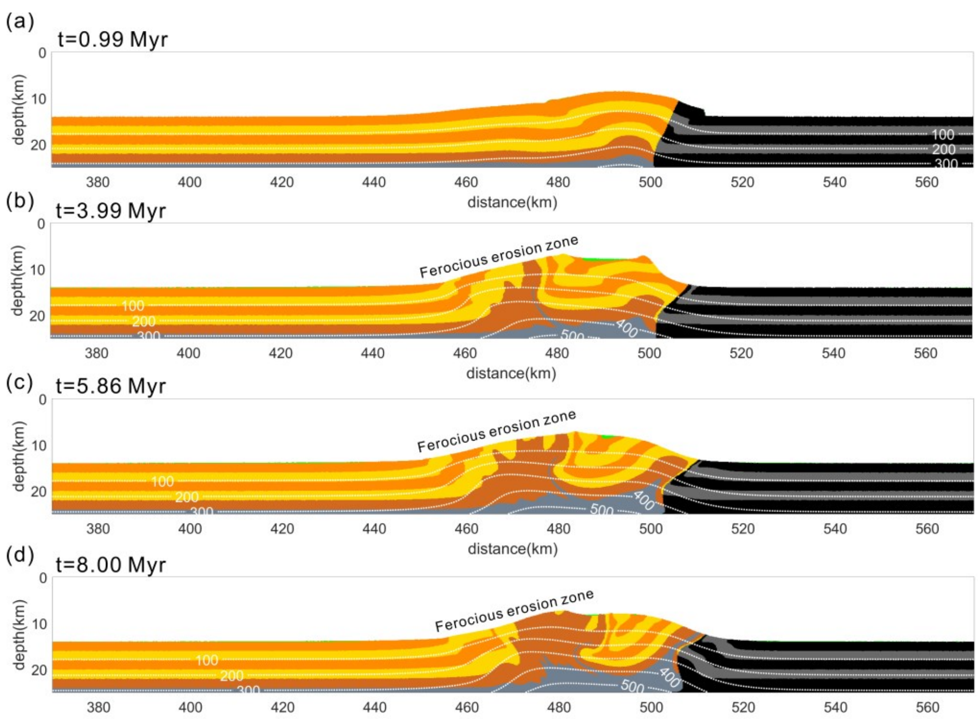

Figure 9. Modelling results showing the evolution of model S034. The white dashed lines indicate isotherms (in ℃). The orographic precipitation applied from t=1 Myr induces rapid erosion within a narrow zone on the windward flank. Most of the material entering the orogenic wedge “flows out” through this narrow window, resulting in relatively stable positioning of the zone with rapid erosion and the width of the orogenic wedge. Sustained, stationary, localized and rapid erosion induces rapid uplift of rocks in local area, leading to the formation of a large-scale antiform.

5.2 Comparison with the eastern Himalayan syntaxis

Taking account of parameter selection and modelling results, we identify that model S034 best matches the field observations from the eastern Himalayan syntaxis (Figure 9 and 10). In model S034, the applied orographic precipitation starting at t=1 Myr induces rapid erosion within a narrow zone (20~25 km scale) on the windward flank of the orogenic wedge (Figure 9 and 10b). Rapid erosion and decompression further result in rapid uplift, exhumation, and deformation of local rocks (Figure 9 and 11). It can be observed that the position of this intense erosion zone and the width of the orogenic wedge remain relatively stable in the long-term time (several million years), indicating a relative equilibrium in the material influx and outflux. This implies that most of the material entering the orogenic wedge "flows out" of this limited area via the narrow erosional window. The magnitudes of the crucial parameters (such as convergence rate, average precipitation and initial geothermal gradient) and the underlying physics (conservation of mass, momentum and energy, rheology, orographic precipitation, surface processes, etc.) ensure that the model develops sustained, stationary, localized, rapid erosion, and decompression on the windward flank. This further induces sustained, rapid rock uplift, exhumation, and deformation in the local area, ultimately forming a large-scale antiform (Figure 9 and 10). These outcomes appear to be the inevitable results of the delicate equilibrium among tectonic forces, climatic forces and crustal thermal structure under various physical laws.

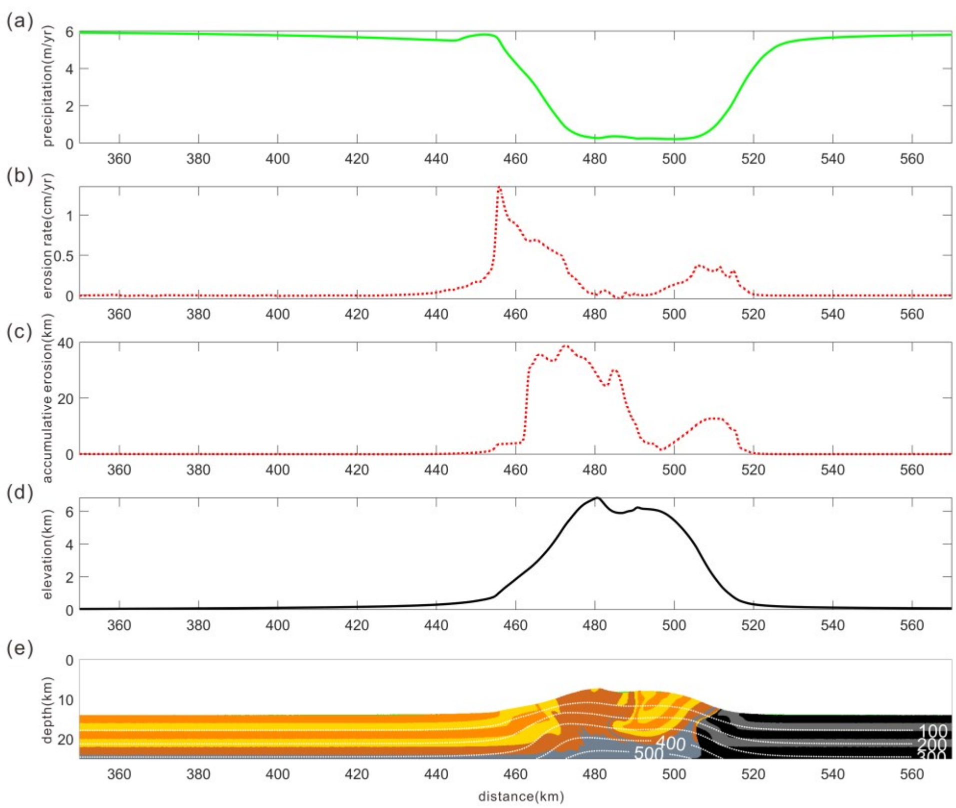

Figure 10. Modelling results of model S034 at t=8 Myr. The modelling results closely approximate various significant aspects of the field observations from the eastern Himalayan syntaxis. (a), (b), (c) and (d) represent the precipitation, transient erosion rate, accumulative erosion and topography along the model cross-section profile, respectively. (e) demonstrates the deformation pattern of the model, where white dashed lines indicate isotherms (in °C).

In model S034, the spatial scale of the area with rapid exhumation and intense deformation in the core of the antiform is about 25 km, which is close to the actual observations from the eastern Himalayan syntaxis (Koons et al., 2013; Zeitler, Meltzer, et al., 2001). The transient erosion rate of 0.5~1.4 cm/yr within the intense erosion zone (Figure 10b) also matches the decadal erosion rate reported by Enkelmann et al. (2011) based on the study of detrital zircon. The accumulative erosion (20~40 km) within this zone is slightly greater than the exhumation (>20 km) inferred from P-T estimates and thermochronological dating (Figure 10c) (Koons et al., 2013). This is reasonable because the rock trajectories within the orogenic wedge are usually non-vertical. Furthermore, the maximum elevation in the core of the antiform reaches approximately 6817 m, which is comparable to the elevations of the two main peaks, Namche Barwa Peak (7782 m) and Gyala Peri Peak (7294 m), in the eastern Himalayan syntaxis region.

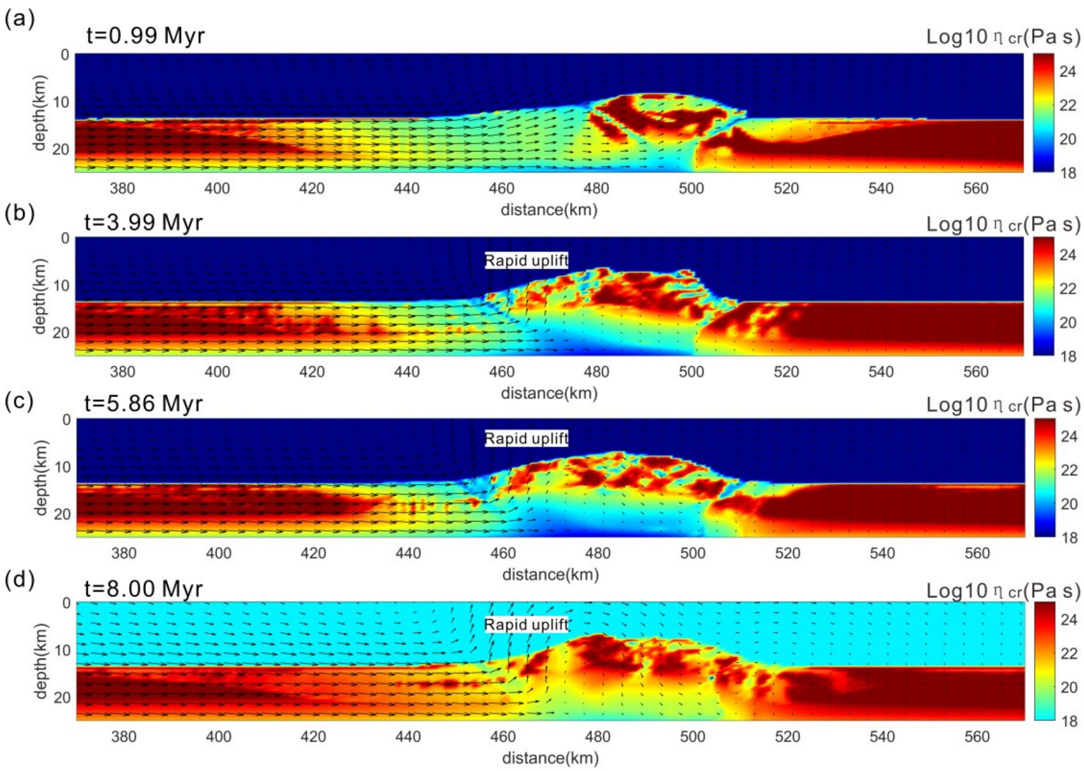

Figure 11. The evolution of the viscosity and velocity field in model S034. Within the intense erosion zone on the windward flank of the orogenic wedge, rapid erosion and decompression induce continuous and rapid uplift of rocks. However, the model doesn't show a significant decrease in the viscosity of rocks within this intense erosion zone.

However, the selected average precipitation of 6 m/year in model S034 is much higher than the current average precipitation (~2 m/yr) in the eastern Himalayan syntaxis region (Anders et al., 2006; Bookhagen & Burbank, 2006), although this value may not align well with the historical precipitations. It's important to note that, due to the model limitations, the erosion rates generated by our surface processes model may be underestimated for two reasons. Firstly, the glacial erosion was not fully accounted for in our model. Secondly, our modelling on landscape evolution employs a 3-by-N grid, which may result in lower water discharge at each point compared to real-world conditions, leading to lower erosion rates. Therefore, to achieve a better approximation of the actual erosional efficiency in the eastern Himalayan syntaxis region, a higher average precipitation would be required. In addition, the convergence rate of 2.0 cm/yr in model S034 is consistent with the Himalayan shortening rate obtained from the reconstruction of the India-Asia convergence history (Guillot et al., 2003). A relatively steep initial geothermal gradient of 30 ℃/km also approximates the relatively hot regime that characterized the majority of the Himalayan-Tibetan Plateau soon after the collision (Zhang et al., 2022).

In summary, the simulation results of model S034 closely match the field observations in the eastern Himalayan syntaxis region from various perspectives, indicating that our modelling scheme is applicable to the study area. Therefore, the mechanisms of tectonic and geomorphic evolution revealed by the model are reliable.

5.3 Syntaxis as the result of the combined effects of multiple factors

Our modelling results indicate that different combinations of tectonic and climatic forces result in various types of orogenic wedges. The three basic types of orogenic wedge mentioned above closely resemble the three end-member types of growing orogens proposed by Wolf et al. (2022). The only difference is that their model is defined on a larger scale (mantle-scale), while our model operates at a relatively smaller scale, specifically limited to the orogenic wedges or fold and thrust belts. Wolf et al. (2022)'s modelling study also shows that the topographic evolution of collisional orogens is determined by the combination of plate velocity, crustal rheology and surface process efficiency. As early as the end of the last century, Avouac and Burov (1996) had proposed that there is a coupled regime allowing for mountain growth. They showed that mountain growth only occurs when the surface mass diffusion and lithospheric shortening exhibit comparable efficiency, otherwise the mountain will "collapse". Similar combined effect of tectonic and climatic forces was also identified in smaller-scale models (Simpson, 2004). This is also supported by the analytical treatment studies. For instance, Roe et al. (2006) have found that the width (L) or height (R_c) of a fluvial-dominated steady-state orogenic wedge is related to both accretionary flux (F) and average precipitation (P_0):

$$R_c(or\ L) \propto F^{\frac{1}{1+h_k m}} P_0^{\frac{-m}{1+h_k m}} \quad (11)$$

where m and n are the discharge and slope exponents, respectively (Whipple & Tucker, 1999). h_k is the Hack's law exponent (Hack, 1957).

Considering the initial thickness of the incoming plate (H) to be relatively constant for a specific orogenic wedge, the accretionary flux can be rewritten as (Dahlen, 1990; Whipple & Meade, 2004):

$$F = H v_c \quad (12)$$

where v_c is the convergence rate. Substituting Equation (12) into Equation (11) and rearranging:

$$R_c(or\ L) \propto \left(\frac{{P_0}^m}{v_c}\right)^{\frac{-1}{1+h_k m}} H^{\frac{1}{1+h_k m}} \quad (13)$$

since H is assumed to be relatively constant, we get:

$$R_c(or\ L) \propto \left(\frac{{P_0}^m}{v_c}\right)^{\frac{-1}{1+h_k m}} \quad (14)$$

From the perspective of energy, the convergence rate and average precipitation can be regarded as significant indicators of the strength of tectonic and climatic forces , respectively

(Xiangjiang & Dalai, 2017). As shown by our modelling results, Equation (14) supports the perspective that the height and width of a specific orogenic wedge primarily rely on the relative strength of tectonic and climatic forces, rather than their respective magnitudes. As m and h_k are typically positive (Montgomery & Dietrich, 1992; Whipple & Tucker, 1999), Equation (14) suggests that the height and width of an orogenic wedge decrease with increasing ratio of average precipitation to convergence rate, which is consistent with our modelling results (Figures 3, 4 and 7). The proportionality symbol (∝) in Equation (14) implies that there are other factors influencing the evolution of orogenic wedges, such as rock erodibility, orogen geometry, and critical taper angle (Roe et al., 2006; Roe et al., 2008). According to our modelling, the geothermal gradients within the crust is also one of the important factors.

Here we assume that the maximum elevation of an orogenic wedge ($MaxE$) is proportional to its height. Then, based on Equation (14), if the convergence rate holds constant, we have:

$$MaxE \propto {P_0}^{x_1} \quad (15)$$

or

$$MaxE = A_1 {P_0}^{x_1} \quad (16)$$

In the same way, if the average precipitation holds constant, we have:

$$MaxE \propto {v_c}^{x_2} \quad (17)$$

or

$$MaxE = A_2 {v_c}^{x_2} \quad (18)$$

where A_1, A_2, x_1, x_2 are coefficients.

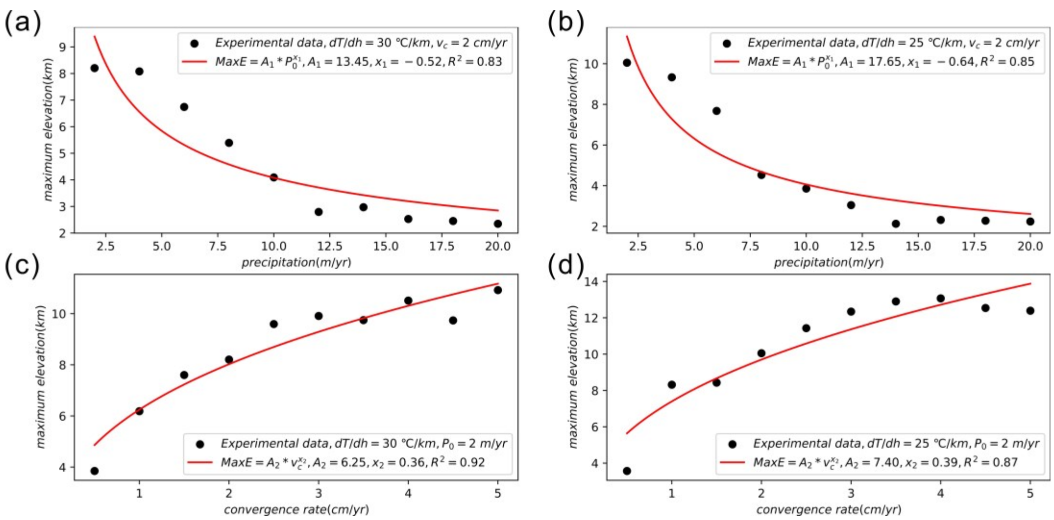

Figure 12. The relationships between the maximum elevations of orogenic wedges and the average precipitations ((a) and (b)) or convergence rates((c) and (d)). Each black dot represents one numerical experiment. Experiments in (a) and (b) have a convergence rate of 2 cm/yr and initial geothermal gradients of 30 °C/km and 25 °C/km, respectively, while experiments in (c) and (d) have an average precipitation of 2 m/yr and initial geothermal gradients of 30 °C/km and 25 °C/km, respectively. The red solid lines represent the best-fit curves obtained through least-squares method using Equation (16) for (a) and (b), and Equation (18) for (c) and (d). The fitting results (R^2>0.83) indicate a good power-law relationship between the maximum elevations of orogenic wedges and both the average precipitations and convergence rates.

To further confirm the above relationships, we performed a least-squares fitting on our experimental data (Figure 12). In Figure 12a and b, the black dots represent the experiments with a convergence rate of 2 cm/yr and initial geothermal gradients of 30 °C/km and 25 °C/km, respectively. Equation (16) was used for fitting, and the fitted values of x_1 are -0.52 and -0.64, with corresponding R^2 of 0.83 and 0.85. Similarly, in Figure 12c and d, the experiments have an average precipitation of 2 m/yr and initial geothermal gradients of 30 °C/km and 25 °C/km, respectively. Equation (18) was used for fitting, and the fitted values of x_2 are 0.36 and 0.39, with corresponding R^2 of 0.92 and 0.87. Theoretically, the values of x_1 and x_2 should be -0.25 and 0.5, respectively (assuming $m = 0.5$ and $h_k = 2$ as suggested by Whipple and Tucker (1999) and Montgomery and Dietrich (1992)). The deviation between the theoretical and fitted values may attribute to the more complex precipitation, surface processes and rheology considered in our model. Nevertheless, both analytical treatment and our numerical modelling indicate that there is a specific power-law relationship between the orogen height and the average precipitation or convergence rate, with negative and positive exponents for average precipitation and convergence rate, respectively.

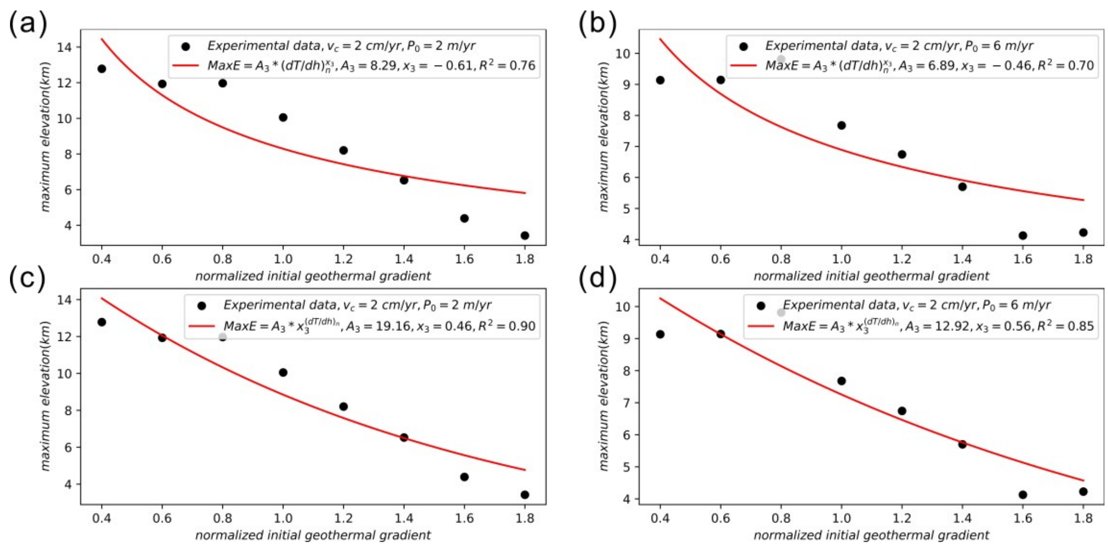

Figure 13. The relationships between the maximum elevations of orogenic wedges and initial geothermal gradients. Each black dot represents one numerical experiment. Experiments in (a) and (c) have a convergence rate and average precipitation of 2 cm/yr and 2 m/yr, respectively, while experiments in (b) and (d) have a convergence rate of 2 cm/yr and an average precipitation of 6 m/yr. The red solid lines represent the best-fit curves obtained through least-squares method using Equation (20) for (a) and (b), and Equation (21) for (b) and (d). The fitting results indicate that the exponential equation provides a better fit than the power-law equation, suggesting a higher probability of an exponential relationship between the maximum elevation of an orogenic wedge and the initial geothermal gradient.

According to our modelling results (Figure 5), it is conceivable that the relationship between the maximum elevation of an orogenic wedge and the initial temperature gradient may follow a similar pattern as its relationship with the average precipitation. In other words, under the condition of constant convergence rate and average precipitation, we may have:

$$MaxE \propto (dT/dh)_n{}^{x_3} \quad (19)$$

or

$$MaxE = A_3 (dT/dh)_n^{\ x_3} \quad (20)$$

where A_3 and x_3 are coefficients. $(dT/dh)_n$ is the initial temperature gradient normalized by average shallow crustal geothermal gradient (25 °C/km). However, when Equation (20) is used for fitting, the resultant goodness of fit is not satisfactory (Figure 13a and b). For two sets of experimental data with a convergence rate of 2 cm/yr and average precipitation of 2 m/yr and 6 m/yr, respectively, the corresponding R^2 are 0.76 and 0.70. This suggests that the relationship between the maximum elevation and the initial temperature gradient may not follow a power-law relationship. On the contrary, it is more likely to exhibit an exponential function relationship:

$$MaxE = A_3 x_3^{(dT/dh)_n} \quad (21)$$

When fitting the same dataset using Equation (21), we achieved significantly improved goodness of fit (the fitted values of x_3 are 0.46 and 0.56, with corresponding R^2 of 0.90 and 0.85, as depicted in Figure 13c and d). This indicates that Equation (21) is more likely to reveal the quantitative relationship between the maximum elevation and the initial temperature gradient compared to Equation (20).

Combining Equations (15), (17) and (21) gives:

$$MaxE \propto {P_0}^{x_1} {v_c}^{x_2} {x_3}^{\left(\frac{dT}{dh}\right)_n} \quad (22)$$

or

$$MaxE = A * {P_0}^{x_1} {v_c}^{x_2} {x_3}^{\left(\frac{dT}{dh}\right)_n} \quad (23)$$

similarly, A, x_1, x_2 and x_3 are coefficients. To unveil the combined effect of average precipitation, convergence rate, and initial temperature gradient on the topographic evolution, we conducted a least-squares fitting on the data from 212 experiments in this study (excluding the 20 experiments with zero precipitation) using Equation (23). The fitted values of $x_1 = -0.35$, $x_2 = 0.71$ and $x_3 = 0.46$ were obtained, with a corresponding R^2 of 0.82. The fitted values of x_1, x_2 and x_3 are sensitive to the dataset used. Statistical analysis of the above fitted values obtained from different datasets showed that the population standard deviations of the fitted values of x_1, x_2 and x_3 are 0.12, 0.16, and 0.047, respectively, none of which exceeds 33% of the absolute value of the mean of the fitted values, indicating that the coefficients are relatively stable. Based on Equation (23), we define the following parameter (E_F):

$$E_F = {P_0}^{-0.35} {v_c}^{0.71} 0.46^{(dT/dh)_n} \quad (24)$$

This parameter can be used to evaluate the combined effect of average precipitation, convergence rate and crustal thermal structure on the topographic evolution of an orogenic wedge. As shown in Figure 14, on the whole, the maximum elevation of the orogenic wedge increases with an increase in E_F. However, when E_F>0.45, the slope becomes gentler, indicating that the orogenic wedge may be in a critical state around $E_F \approx 0.45$. On either side of this critical state (E_F<0.45 or E_F>0.45), the evolution of an orogenic wedge seems to exhibit different patterns. This suggests that orogen is not simply a linear system (Phillips et al., 2003), and highly complex nonlinear mechanisms may be involved during its evolutionary process. Moreover, it is evident that most of the type A and B orogenic wedges are distributed on the left and right sides of line E_F=0.45, respectively, while type C orogenic wedges are distributed around this line. Type D orogenic wedges are primarily concentrated within the narrow band of 0.24<E_F<0.45. Admittedly, the four types of orogenic wedges cannot be perfectly identified through the value of E_F. This may be attributed to the fact that most experiments at the boundaries of two different types of orogenic wedges in Figure 7 are actually transitional types, and they were assigned to the category that best represents their most prominent features. This is inevitable and it may have introduced some degree of error. Nevertheless, our modelling results indicate that the tectonic and geomorphic evolution of the orogenic wedge is closely related to parameter E_F. Furthermore, we estimated the E_F of the eastern Himalayan syntaxis based on a convergence rate of 2.0 cm/yr (Guillot et al., 2003), an average precipitation of 2.0 m/yr (Anders et al., 2006; Bookhagen & Burbank, 2006) and a crustal geothermal gradient of 50 ℃/km (Craw et al., 2005). The result shows that the E_F (0.27) of the eastern Himalayan syntaxis is also situated within the specific range, implying that the tectonic and geomorphic evolution of the syntaxis is not solely influenced by a single factor but the result of the combined effects of multiple factors (Figure 14).

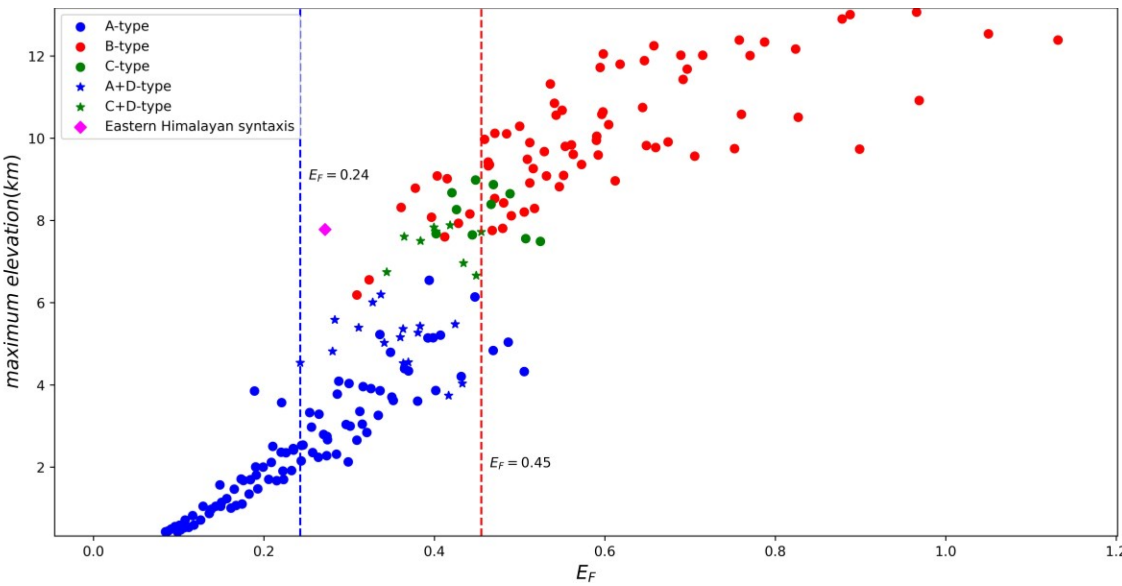

Figure 14. Plot of the maximum elevation of the orogenic wedges against E_F. The dots and stars represent the 200 experiments from Table S2 and S3 in Supporting Information S1 (20 experiments with average precipitation of 0 m/yr are excluded). The blue, red and green colors correspond to type A, B and C orogenic wedges, respectively. The stars represent orogenic wedges that exhibit similar structural features to the eastern Himalayan syntaxis (type D). Most of the type A and B orogenic wedges are distributed on the left and right sides of line $E_F = 0.45$, respectively, while type C orogenic wedges are distributed around this line. Type D orogenic wedges are primarily concentrated within the narrow band of $0.24 < E_F < 0.45$, and the eastern Himalayan syntaxis, depicted as a fuchsia diamond, is also situated within this specific range. On the whole, the maximum elevation of orogenic wedges is proportional to E_F, but the slope becomes gentler when $E_F > 0.45$. This suggests that orogenic wedges seem to be in a critical state when $E_F \approx 0.45$. Thus the evolution of an orogenic system should be non-linear.

5.4 The mechanism of the formation of the eastern Himalayan syntaxis

All the three classical models explaining the formation of syntaxis have undergone extensive testing through abundant field observations and numerical modeling studies (Bendick & Ehlers, 2014; Burg et al., 1998; Burg & Podladchikov, 1999; Burg & Schmalholz, 2008; Ding et al., 2001; Koons et al., 2002; Koptev et al., 2019; Nettesheim et al., 2018; Yang et al., 2023; Zeitler, Koons, et al., 2001; Zeitler et al., 2014; Zhang et al., 2004). Our modelling results indicate that the processes involved in the formation of syntaxis are more closely associated with those described by the tectonic aneurysm model (Figure 8 and 9), and we propose that the initiation of these processes requires the cooperation of tectonic forces, climatic forces and geothermal field (Figure 15).

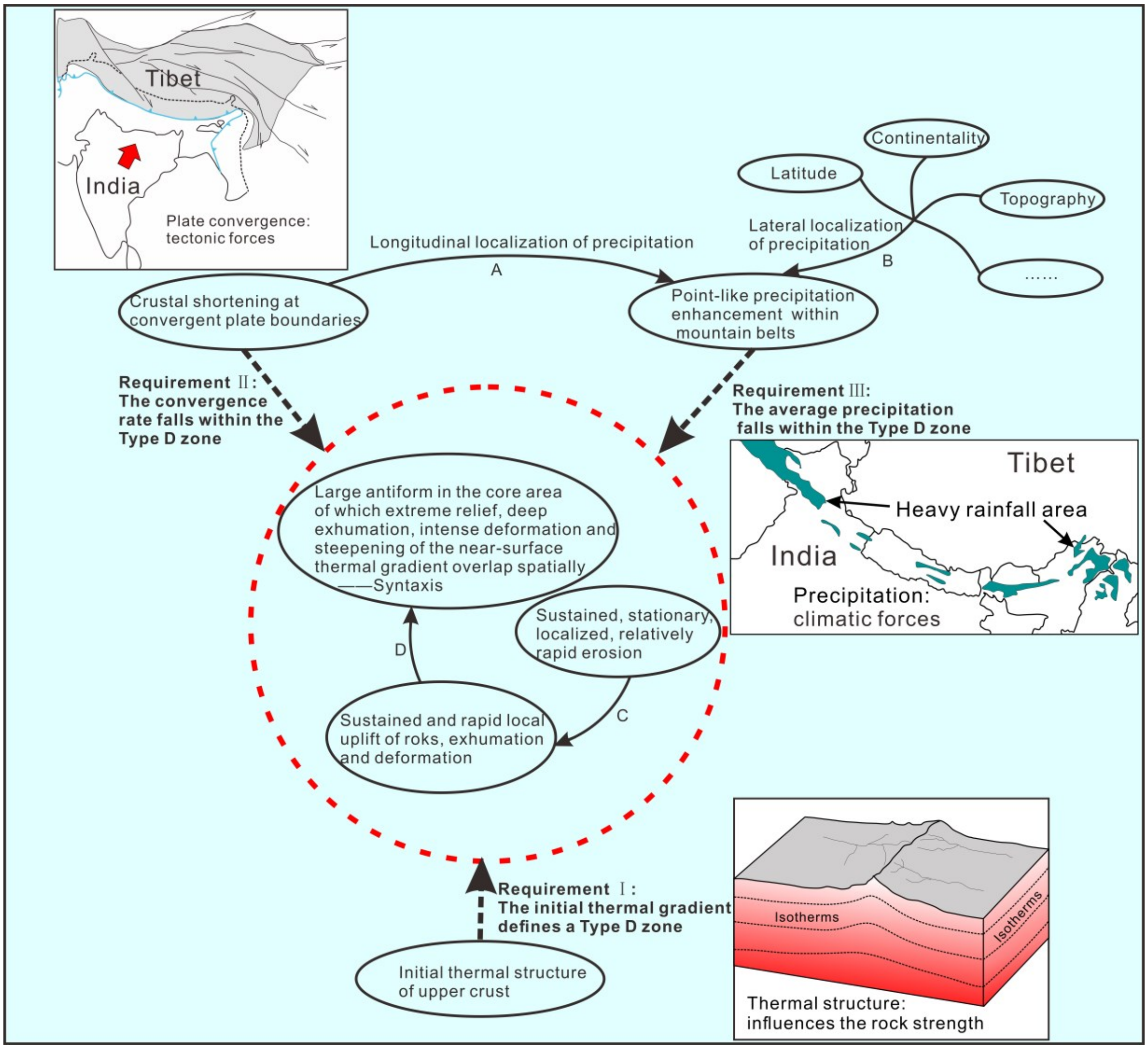

Figure 15. The proposed mechanism of the formation of the eastern Himalayan syntaxis. The elements outside the red dashed circle are the conditions for the formation of a syntaxis, while the elements inside the red dashed circle show the process of its formation. The formation of a syntaxis requires the combination of tectonic forces, climatic forces and crustal thermal structure. Once the convergence rate and the average precipitation fall within the Type D zone determined by the thermal structure of shallow crust, a sustained, stationary, localized and relatively rapid erosion process will be established on the windward flank of the orogenic wedge. This will further induce sustained and rapid uplift of rocks, exhumation and deformation, ultimately forming a syntaxis.

For a given crust, it may have a Type D zone, which is determined by its thermal structure (Figure 7). In addition, a certain degree of regional tectonic compression (or crustal shortening) and precipitation, including the resultant erosion, are also necessary. During the orogenesis, regional tectonic compression sets the initial conditions by raising Earth's surface. If moisture is transported into the region by the prevailing winds, it will lead to longitudinal (perpendicular to the strike of the mountain range) localization of precipitation (Anders et al., 2006; Berger & Spotila, 2008; Burbank et al., 2003; Reiners et al., 2003; Roe, 2005; Roe et al., 2002; Wratt et al., 2000) (Figure 15 path A, Figure 10a). At the same time, precipitation is also influenced by other factors such as latitude, continentality, and topographic features (Barry, 2008), which can lead to spatial heterogeneity of precipitation in the direction parallel to the strike of the mountain range, namely lateral localization of precipitation (Anders et al., 2006; Bookhagen & Burbank, 2006) (Figure 15 path B). The superposition of these two effects will lead to point-like precipitation enhancement within mountain belts. If the average precipitation and convergence rate fall within the Type D zone, a sustained, stationary, localized and relatively rapid erosion process will be established on the windward flank (Figure 9). This will further induce sustained and rapid uplift of rocks, exhumation and deformation (Figure 9, Figure 11, Figure 15 path C), ultimately leading to the formation of a large-scale antiform. At the core area of the antiform, extreme relief, deep exhumation, intense deformation and steepening of the near-surface thermal gradient overlap spatially. Additionally, the crustal material may experience low-P-high-T metamorphism and decompression melting during rapid uplifting and exhumation (Booth et al., 2009; Booth et al., 2004; Koons et al., 2002; Koons et al., 2013; Zeitler, Meltzer, et al., 2001) (Figure 17). Here, "sustained" means that the formation of a mature syntaxis needs a certain amount of time. According to our modelling, this process takes several million years. During this period, the average precipitation and convergence rate need to remain relatively stable (not falling outside the Type D zone). "Stationary" and "localized" mean that the position of the intense erosion zone on the windward flank do not undergo significant changes (Figure 9, Figure 11). "Relatively rapid" means that the erosional efficiency cannot be too fast (which would rapidly flatten the topography) nor too slow (which would cause continuous of deformation towards the foreland basin and lead to the displacement of the position of the intense erosion zone). Instead, it should be moderate to allow the majority of the material entering the orogenic wedge "flows out" through the narrow erosional window (Figure 11, Figure 16), so that this state can be maintained relatively stable over the long term (several million years).

In this context, the process of rock uplift triggered by erosion is governed by the universal principle that natural systems have the tendency towards dynamic equilibrium (Hack, 1975). The dynamic equilibrium of an orogen can be expressed as relatively stable states of material flux, topography, geotherm and exhumation (Willett & Brandon, 2002). In essence, it's about the equilibrium of temperature and pressure within the orogenic system. Rapid erosion can cause perturbations in the orogenic system, resulting in imbalances in temperature and pressure. To achieve a new state of equilibrium, the orogen will respond to the perturbations by undergoing rapid uplift, exhumation, deformation and steepening of geothermal gradients. Satellite rainfall estimates indicate that heaviest rainfall amounts within Himalayas occur closer to the major moisture source, the two ends of the Himalayan arc (Anders et al., 2006; Bookhagen & Burbank, 2006). Such precipitation localization effect might have resulted in the average precipitation and convergence rates at two ends of the Himalayan arc falling within their Type D zones, thereby promoting the development of syntaxes. The east-west rainfall gradient in the Himalayas is mainly influenced by the shape of Indian subcontinent, which has contributed to its stability since the onset of the Indian and east Asian monsoons (8-9 Ma) (Zhisheng et al., 2001). Meanwhile, the shortening rate of the Himalayas has remained relatively stable since 40 Ma

(Guillot et al., 2003), providing relatively stable tectonic and climatic conditions for the development of a mature syntaxis.

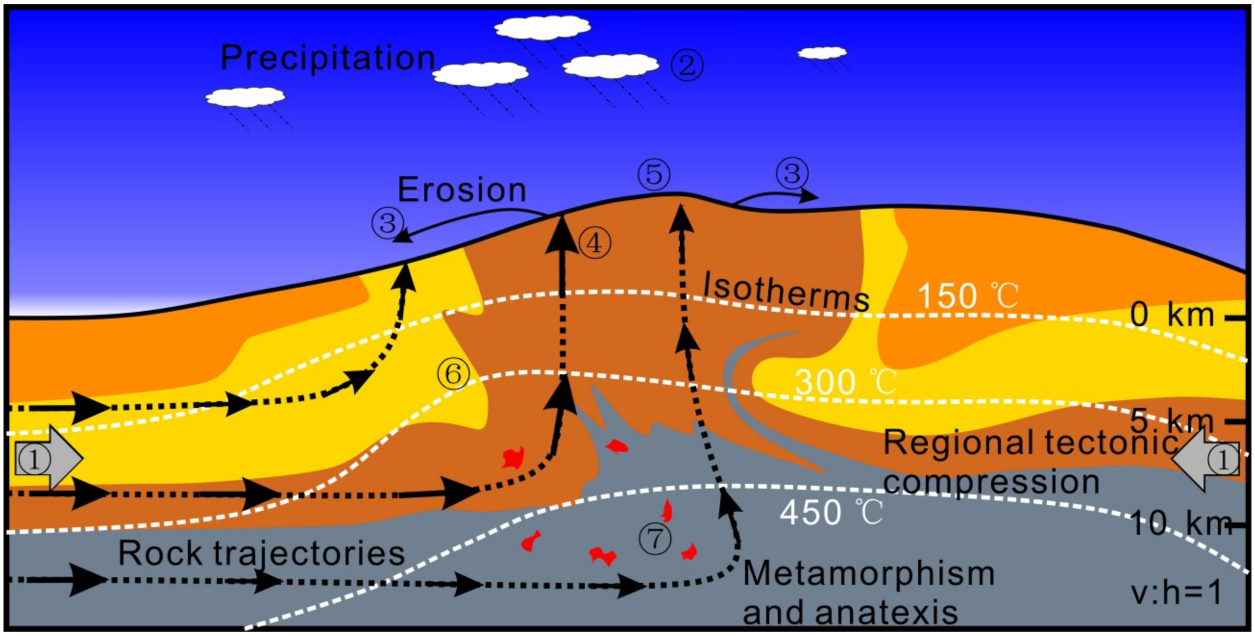

Figure 16. Geologic manifestation of a mature syntaxis. Once the convergence rate(①) and the average precipitation(②) fall within the Type D zone determined by the thermal structure of shallow crust, the formation process of a syntaxis will be initiated. Subsequently, a sustained, stationary, localized and relatively rapid erosion process(③) will be established on the windward flank of the orogenic wedge. This erosion process further induces sustained and rapid uplift of rocks, deep exhumation and intense deformation(④) within the intense erosion zone, forming large-scale antiform. Within the core of the antiform, extreme relief(⑤), deep exhumation, intense deformation and steepning of the near-surface thermal gradient(⑥) overlap spatially. During rapid uplifting and exhumation, crustal material may experience low-P-high-T metamorphism and decompression melting(⑦).

In model S034 and other type D models, there are no obvious low-viscosity channels observed near the intense erosion zone on the windward flank of the orogenic wedge (Figure 11). Therefore, we suspect that the positive feedback among erosion, heat advection, rock strength and deformation may not be necessary during the development of syntaxis. However, strain concentration and steepening of geothermal gradients will inevitably reduce rock viscosity in some degree (Ranalli, 1995; Turcotte & Schubert, 2014) so that the positive feedback is theoretically possible (Koons et al., 2002; Yang et al., 2023). In our models, the positive feedback was not observed possibly due to our model simplifications.

The complex interplay among climate, tectonics and surface processes in the orogen implies that orogen is best viewed as complex open system controlled by multiple factors (Pinter & Brandon, 1997). The system always evolves towards dynamic equilibrium and responds to changes in controlling factors in order to achieve a new state of equilibrium (Molnar, 2009). The response of the orogenic system to a specific factor also depends on the other controlling factors. Therefore, the evolution of an orogen is determined by a series of controlling factors (system inputs), none of which can be considered as the sole cause of the system's outcome. In mountain belts, once the convergence rate and the average precipitation fall within the Type D zone determined by the crustal thermal structure, syntaxis becomes the inevitable system's outcome under various physical laws, including conservation of mass, momentum and energy, rheology, orographic precipitation, surface processes, etc.

5 Conclusions

We presented results from numerical experiments that explore the interactions between climate, tectonics and surface processes, as well as the formation conditions and mechanisms of the eastern Himalayan syntaxis. In this study, we have tested three crucial controlling parameters: the convergence rate, average precipitation and initial geothermal gradient. Combined with field observations, we draw the following conclusions:

1. For a specific orogenic wedge, its tectonic and topographic evolution primarily relies on the relative strength of tectonic and climatic forces, rather than their respective magnitudes. When the tectonic forces are relatively stronger, the orogenic wedge tends to broaden, increase in elevation, and develop thrust faults. Conversely, when the tectonic forces are relatively weaker, the orogenic wedge tends to narrow, decrease in elevation, and develop folds.
2. For a specific orogenic wedge, there may exist a Type D zone in the in the $P_0 - v_c$ parameter space. This Type D zone is determined by the thermal structure of the crust, and its presence is the necessary condition for the development of a syntaxis.
3. Orogens are best viewed as complex open systems controlled by multiple factors. A syntaxis is the result of the combined effects of tectonic forces, climatic forces and geothermal field. In mountain belts, once the convergence rate and the average precipitation fall within the Type D zone, syntaxis becomes the inevitable system's outcome under various physical laws, including conservation of mass, momentum and energy, rheology, orographic precipitation, surface processes, etc.

Acknowledgments

This research has been funded by the National Natural Science Foundation of China (Grants Nos. 40472100, and 41472175). We are indebted to Prof. Taras Gerya for generously sharing the finite difference code used for thermo-mechanical calculations. We also express our gratitude to Daniel E. J. Hobley, Katherine R. Barnhart and their team for granting us access to landlab software for landscape evolution modelling.

Data Availability Statement

The finite difference code used for thermo-mechanical calculations can be found at www.cambridge.org/gerya2e. The landlab source code is found at https://github.com/landlab/landlab. Figures are plotted by MATLAB and Python.

References

Anders, A. M., Roe, G. H., Hallet, B., Montgomery, D. R., Finnegan, N. J., & Putkonen, J. (2006). Spatial patterns of precipitation and topography in the Himalaya. *Special Papers-Geological Society of America*, *398*, 39.

Avouac, J.-P., & Burov, E. (1996). Erosion as a driving mechanism of intracontinental mountain growth. *Journal of Geophysical Research: Solid Earth*, *101*(B8), 17747-17769.

Bahadori, A., Holt, W. E., Feng, R., Austermann, J., Loughney, K. M., Salles, T., . . . Flesch, L. M. (2022). Coupled influence of tectonics, climate, and surface processes on landscape evolution in southwestern North America. *Nature communications*, *13*(1), 4437.

Barnhart, K. R., Glade, R. C., Shobe, C. M., & Tucker, G. E. (2019). Terrainbento 1.0: a Python package for multi-model analysis in long-term drainage basin evolution. *Geoscientific Model Development*, *12*(4), 1267-1297.

Barnhart, K. R., Hutton, E. W., Tucker, G. E., Gasparini, N. M., Istanbulluoglu, E., Hobley, D. E., . . . Adams, J. M. (2020). Landlab v2. 0: A software package for Earth surface dynamics. *Earth Surface Dynamics*, *8*(2), 379-397.

Barros, A. P., & Lettenmaier, D. P. (1994). Dynamic modeling of orographically induced precipitation. *Reviews of geophysics*, *32*(3), 265-284.

Barry, R. (2008). Mountain weather and climate. Cambridge University Press. *New York*.

Beaumont, C., Jamieson, R. A., Nguyen, M., & Lee, B. (2001). Himalayan tectonics explained by extrusion of a low-viscosity crustal channel coupled to focused surface denudation. *Nature*, *414*(6865), 738-742.

Beaumont, C., Jamieson, R. A., Nguyen, M. H., & Medvedev, S. (2004). Crustal channel flows: 1. Numerical models with applications to the tectonics of the Himalayan ‐ Tibetan orogen. *Journal of Geophysical Research: Solid Earth*, *109*(B6).

Bendick, R., & Ehlers, T. A. (2014). Extreme localized exhumation at syntaxes initiated by subduction geometry. *Geophysical Research Letters*, *41*(16), 5861-5867.

Berger, A. L., Gulick, S. P., Spotila, J. A., Upton, P., Jaeger, J. M., Chapman, J. B., . . . Willems, B. A. (2008). Quaternary tectonic response to intensified glacial erosion in an orogenic wedge. *Nature geoscience*, *1*(11), 793-799.

Berger, A. L., & Spotila, J. A. (2008). Denudation and deformation in a glaciated orogenic wedge: The St. Elias orogen, Alaska. *Geology*, *36*(7), 523-526.

Bookhagen, B., & Burbank, D. W. (2006). Topography, relief, and TRMM ‐ derived rainfall variations along the Himalaya. *Geophysical Research Letters*, *33*(8).

Booth, A. L., Chamberlain, C. P., Kidd, W. S., & Zeitler, P. K. (2009). Constraints on the metamorphic evolution of the eastern Himalayan syntaxis from geochronologic and petrologic studies of Namche Barwa. *Geological Society of America Bulletin*, *121*(3-4), 385-407.

Booth, A. L., Zeitler, P. K., Kidd, W. S., Wooden, J., Liu, Y., Idleman, B., . . . Chamberlain, C. P. (2004). U-Pb zircon constraints on the tectonic evolution of southeastern Tibet, Namche Barwa area. *American journal of Science*, *304*(10), 889-929.

Bracciali, L., Parrish, R. R., Najman, Y., Smye, A., Carter, A., & Wijbrans, J. R. (2016). Plio-Pleistocene exhumation of the eastern Himalayan syntaxis and its domal ‘pop-up’. *Earth-Science Reviews*, *160*, 350-385.

Buiter, S. J. (2012). A review of brittle compressional wedge models. *Tectonophysics*, *530*, 1-17.

Burbank, D., Blythe, A., Putkonen, J., Pratt-Sitaula, B., Gabet, E., Oskin, M., . . . Ojha, T. (2003). Decoupling of erosion and precipitation in the Himalayas. *Nature*, *426*(6967), 652-655.

Burg, J.-P., Nievergelt, P., Oberli, F., Seward, D., Davy, P., Maurin, J.-C., . . . Meier, M. (1998). The Namche Barwa syntaxis: evidence for exhumation related to compressional crustal folding. *Journal of Asian Earth Sciences*, *16*(2-3), 239-252.

Burg, J.-P., & Podladchikov, Y. (1999). Lithospheric scale folding: numerical modelling and application to the Himalayan syntaxes. *International Journal of Earth Sciences*, *88*(2), 190-200.

Burg, J.-P., & Schmalholz, S. (2008). Viscous heating allows thrusting to overcome crustal-scale buckling: Numerical investigation with application to the Himalayan syntaxes. *Earth and Planetary Science Letters*, *274*(1-2), 189-203.

Burg, J. P., Davy, P., Nievergelt, P., Oberli, F., Seward, D., Diao, Z., & Meier, M. (1997). Exhumation during crustal folding in the Namche ‐ Barwa syntaxis. *Terra Nova*, *9*(2), 53-56.

Butler, R. W. (2019). Tectonic evolution of the Himalayan syntaxes: the view from Nanga Parbat. *Geological Society, London, Special Publications*, *483*(1), 215-254.

Butler, R. W. H., Casey, M., Lloyd, G. E., Bond, C. E., McDade, P., Shipton, Z., & Jones, R. (2002). Vertical stretching and crustal thickening at Nanga Parbat, Pakistan Himalaya: a model for distributed continental deformation during mountain building. *Tectonics*, *21*(4), 9-1-9-17.

Champagnac, J. D., Molnar, P., Sue, C., & Herman, F. (2012). Tectonics, climate, and mountain topography. *Journal of Geophysical Research: Solid Earth*, *117*(B2).

Champagnac, J. D., Valla, P. G., & Herman, F. (2014). Late-Cenozoic relief evolution under evolving climate: A review. *Tectonophysics*, *614*(1), 44-65.

Clift, P. D., Pandey, D. K., & Kulhanek, D. K. (2020). Climate–tectonic interactions in the eastern Arabian Sea. *Geological Magazine*, *157*(6), 829-833.

Crameri, F., Schmeling, H., Golabek, G., Duretz, T., Orendt, R., Buiter, S., . . . Tackley, P. (2012). A comparison of numerical surface topography calculations in geodynamic modelling: an evaluation of the 'sticky air'method. *Geophysical Journal International*, *189*(1), 38-54.

Craw, D., Koons, P., Zeitler, P., & Kidd, W. (2005). Fluid evolution and thermal structure in the rapidly exhuming gneiss complex of Namche Barwa–Gyala Peri, eastern Himalayan syntaxis. *Journal of Metamorphic Geology*, *23*(9), 829-845.

Cruz, L., Malinski, J., Wilson, A., Take, W., & Hilley, G. (2010). Erosional control of the kinematics and geometry of fold‐and‐thrust belts imaged in a physical and numerical sandbox. *Journal of Geophysical Research: Solid Earth*, *115*(B9).

Culling, W. (1963). Soil creep and the development of hillside slopes. *The Journal of Geology*, *71*(2), 127-161.

Dadson, S. J., Hovius, N., Chen, H., Dade, W. B., Hsieh, M.-L., Willett, S. D., . . . Stark, C. P. (2003). Links between erosion, runoff variability and seismicity in the Taiwan orogen. *Nature*, *426*(6967), 648-651.

Dahlen, F. (1990). Critical taper model of fold-and-thrust belts and accretionary wedges. *Annual Review of Earth and Planetary Sciences*, *18*(1), 55-99.

Dahlen, F., Suppe, J., & Clark, S. (1988). Mechanics, growth, and erosion of mountain belts. *Processes in continental lithospheric deformation*, *218*, 161-178.

Davy, P., & Lague, D. (2009). Fluvial erosion/transport equation of landscape evolution models revisited. *Journal of Geophysical Research: Earth Surface*, *114*(F3).

Ding, L., Zhong, D., Yin, A., Kapp, P., & Harrison, T. M. (2001). Cenozoic structural and metamorphic evolution of the eastern Himalayan syntaxis (Namche Barwa). *Earth and Planetary Science Letters*, *192*(3), 423-438.

Egholm, D., Nielsen, S., Pedersen, V., & Lesemann, J.-E. (2009). Glacial effects limiting mountain height. *Nature*, *460*(7257), 884-887.

Emanuel, K. A. (1994). *Atmospheric convection*. Oxford University Press on Demand.

Enkelmann, E., Ehlers, T., Zeitler, P., & Hallet, B. (2011). Denudation of the Namche Barwa antiform, eastern Himalaya. *Earth and Planetary Science Letters*, *307*(3-4), 323-333.

Fernandes, N. F., & Dietrich, W. E. (1997). Hillslope evolution by diffusive processes: The timescale for equilibrium adjustments. *Water Resources Research*, *33*(6), 1307-1318.

Finnegan, N. J., Hallet, B., Montgomery, D. R., Zeitler, P. K., Stone, J. O., Anders, A. M., & Yuping, L. (2008). Coupling of rock uplift and river incision in the Namche Barwa–Gyala Peri massif, Tibet. *Geological Society of America Bulletin*, *120*(1-2), 142-155.

Gerya, T. (2019). *Introduction to numerical geodynamic modelling*. Cambridge University Press.

Gong, J., Ji, J., Zhou, J., Tu, J., Sun, D., Zhong, D., & Han, B. (2015). Late Miocene thermal evolution of the eastern Himalayan syntaxis as constrained by biotite 40Ar/39Ar thermochronology. *The Journal of Geology*, *123*(4), 369-384.

Grujic, D., Coutand, I., Bookhagen, B., Bonnet, S., Blythe, A., & Duncan, C. (2006). Climatic forcing of erosion, landscape, and tectonics in the Bhutan Himalayas. *Geology*, *34*(10), 801-804.

Guillot, S., Garzanti, E., Baratoux, D., Marquer, D., Mahéo, G., & de Sigoyer, J. (2003). Reconstructing the total shortening history of the NW Himalaya. *Geochemistry, Geophysics, Geosystems*, *4*(7).

Hack, J. T. (1957). *Studies of longitudinal stream profiles in Virginia and Maryland* (Vol. 294). US Government Printing Office.

Hack, J. T. (1975). Dynamic equilibrium and landscape evolution. *Theories of landform development*, *1*, 87-102.

Herman, F., Seward, D., Valla, P. G., Carter, A., Kohn, B., Willett, S. D., & Ehlers, T. A. (2013). Worldwide acceleration of mountain erosion under a cooling climate. *Nature*, *504*(7480), 423-426.

Hilley, G., Strecker, M., & Ramos, V. (2004). Growth and erosion of fold‐and‐thrust belts with an application to the Aconcagua fold‐and‐thrust belt, Argentina. *Journal of Geophysical Research: Solid Earth*, *109*(B1).

Hobley, D. E., Adams, J. M., Nudurupati, S. S., Hutton, E. W., Gasparini, N. M., Istanbulluoglu, E., & Tucker, G. E. (2017). Creative computing with Landlab: an open-source toolkit for building, coupling, and exploring two-dimensional numerical models of Earth-surface dynamics. *Earth Surface Dynamics*, *5*(1), 21-46.

King, G. E., Herman, F., & Guralnik, B. (2016). Northward migration of the eastern Himalayan syntaxis revealed by OSL thermochronometry. *Science*, *353*(6301), 800-804.

Koons, P. (1995). Modeling the topographic evolution of collisional belts. *Annual Review of Earth and Planetary Sciences*, *23*(1), 375-408.

Koons, P., Zeitler, P., Chamberlain, C., Craw, D., & Meltzer, A. (2002). Mechanical links between erosion and metamorphism in Nanga Parbat, Pakistan Himalaya. *American journal of Science*, *302*(9), 749-773.

Koons, P. O., Zeitler, P. K., & Hallet, B. (2013). Tectonic Aneurysms and Mountain Building. In J. F. Shroder (Ed.), *Treatise on geomorphology* (pp. 318-349). Academic Press. https://doi.org/https://doi.org/10.1016/B978-0-12-374739-6.00094-4

Koptev, A., Ehlers, T. A., Nettesheim, M., & Whipp, D. M. (2019). Response of a rheologically stratified lithosphere to subduction of an indenter‐shaped plate: Insights into localized exhumation at orogen syntaxes. *Tectonics*, *38*(6), 1908-1930.

Lin, T.-H., Lo, C.-H., Chung, S.-L., Hsu, F.-J., Yeh, M.-W., Lee, T.-Y., . . . Liu, D. (2009). 40Ar/39Ar dating of the Jiali and Gaoligong shear zones: Implications for crustal deformation around the Eastern Himalayan Syntaxis. *Journal of Asian Earth Sciences*, *34*(5), 674-685.

Liu, Y., & Zhong, D. (1997). Petrology of high‐pressure granulites from the eastern Himalayan syntaxis. *Journal of Metamorphic Geology*, *15*(4), 451-466.

Molnar, P. (2003). Nature, nurture and landscape. *Nature*, *426*(6967), 612-613.

Molnar, P. (2009). The state of interactions among tectonics, erosion, and climate: A polemic. *GSA Today*, *19*(7), 44-45.

Molnar, P., & England, P. (1990). Late Cenozoic uplift of mountain ranges and global climate change: chicken or egg? *Nature*, *346*(6279), 29-34.

Montgomery, D. R., & Dietrich, W. E. (1992). Channel initiation and the problem of landscape scale. *Science*, *255*(5046), 826-830.

Mukhopadhyay, B., Acharyya, A., Bhattacharyya, D., Dasgupta, S., & Pande, P. (2011). Seismotectonics at the terminal ends of the Himalayan arc. *Geomatics, Natural Hazards and Risk*, *2*(2), 159-181.

NASEM. (2020). *A vision for NSF Earth sciences 2020-2030: Earth in time*. National Academies Press.

Nettesheim, M., Ehlers, T. A., Whipp, D. M., & Koptev, A. (2018). The influence of upper-plate advance and erosion on overriding plate deformation in orogen syntaxes. *Solid Earth*, *9*(6), 1207-1224.

Norton, K., & Schlunegger, F. (2011). Migrating deformation in the Central Andes from enhanced orographic rainfall. *Nature communications*, *2*(1), 1-7.

Peizhen, Z., Molnar, P., & Downs, W. R. (2001). Increased sedimentation rates and grain sizes 2–4 Myr ago due to the influence of climate change on erosion rates. *Nature*, *410*(6831), 891-897.

Phillips, C. L., Parr, J. M., Riskin, E. A., & Prabhakar, T. (2003). *Signals, systems, and transforms*. Prentice Hall Upper Saddle River.

Pinter, N., & Brandon, M. T. (1997). How erosion builds mountains. *Scientific American*, *276*(4), 74-79.

Ranalli, G. (1995). *Rheology of the Earth*. Springer Science & Business Media.

Raymo, M. E., & Ruddiman, W. F. (1992). Tectonic forcing of late Cenozoic climate. *Nature*, *359*(6391), 117-122.

Reiners, P. W., Ehlers, T. A., Mitchell, S. G., & Montgomery, D. R. (2003). Coupled spatial variations in precipitation and long-term erosion rates across the Washington Cascades. *Nature*, *426*(6967), 645-647.

Roe, G. H. (2005). Orographic precipitation. *Annu. Rev. Earth Planet. Sci.*, *33*, 645-671.

Roe, G. H., Montgomery, D. R., & Hallet, B. (2002). Effects of orographic precipitation variations on the concavity of steady-state river profiles. *Geology*, *30*(2), 143-146.

Roe, G. H., Stolar, D. B., & Willett, S. D. (2006). Response of a steady-state critical wedge orogen to changes in climate and tectonic forcing. *Special Papers-Geological Society of America*, *398*, 227.

Roe, G. H., Whipple, K. X., & Fletcher, J. K. (2008). Feedbacks among climate, erosion, and tectonics in a critical wedge orogen. *American journal of Science*, *308*(7), 815-842.

Royden, L. H., Burchfiel, B. C., & van der Hilst, R. D. (2008). The geological evolution of the Tibetan Plateau. *Science*, *321*(5892), 1054-1058.

Ruh, J. B., Kaus, B. J., & Burg, J. P. (2012). Numerical investigation of deformation mechanics in fold‐and‐thrust belts: Influence of rheology of single and multiple décollements. *Tectonics*, *31*(3).

Schmeling, H., Babeyko, A., Enns, A., Faccenna, C., Funiciello, F., Gerya, T., . . . Morra, G. (2008). A benchmark comparison of spontaneous subduction models—Towards a free surface. *Physics of the Earth and Planetary Interiors*, *171*(1-4), 198-223.

Schulte-Pelkum, V., Monsalve, G., Sheehan, A., Pandey, M., Sapkota, S., Bilham, R., & Wu, F. (2005). Imaging the Indian subcontinent beneath the Himalaya. *Nature*, *435*(7046), 1222-1225.

Seward, D., & Burg, J.-P. (2008). Growth of the Namche Barwa Syntaxis and associated evolution of the Tsangpo Gorge: Constraints from structural and thermochronological data. *Tectonophysics*, *451*(1-4), 282-289.

Simpson, G. (2004). Role of river incision in enhancing deformation. *Geology*, *32*(4), 341-344.

Smith, R., & Barstad, I. (2004). A Linear Theory of Orographic Precipitation. *Journal of The Atmospheric Sciences - J ATMOS SCI*, *61*, 1377-1391. https://doi.org/10.1175/1520-0469(2004)061<1377:ALTOOP>2.0.CO;2

Song, Z., Zhenhan, W., Xitao, Z., Jianping, L., & Hua, W. (2012). Middle-Late Pleistocene Glacial Lakes in the Grand Canyon of the Tsangpo River, Tibet. *Acta Geologica Sinica - English Edition*, *86*(1), 266-283. https://doi.org/https://doi.org/10.1111/j.1755-6724.2012.00627.x

Steer, P., Simoes, M., Cattin, R., & Shyu, J. B. H. (2014). Erosion influences the seismicity of active thrust faults. *Nature communications*, *5*(1), 1-7.

Stewart, R., Hallet, B., Zeitler, P., Malloy, M., Allen, C. M., & Trippett, D. (2008). Brahmaputra sediment flux dominated by highly localized rapid erosion from the easternmost Himalaya. *Geology*, *36*(9), 711-714.

Stolar, D. B., Willett, S. D., & Roe, G. H. (2006). Climatic and tectonic forcing of a critical orogen. *Special Papers-Geological Society of America*, *398*, 241.

Tapponnier, P., Zhiqin, X., Roger, F., Meyer, B., Arnaud, N., Wittlinger, G., & Jingsui, Y. (2001). Oblique stepwise rise and growth of the Tibet Plateau. *Science*, *294*(5547), 1671-1677.

Tomkin, J. H., & Roe, G. H. (2007). Climate and tectonic controls on glaciated critical-taper orogens. *Earth and Planetary Science Letters*, *262*(3-4), 385-397.

Tu, J.-Y., Ji, J.-Q., Sun, D.-X., Gong, J.-F., Zhong, D.-L., & Han, B.-F. (2015). Thermal structure, rock exhumation, and glacial erosion of the Namche Barwa Peak, constraints from thermochronological data. *Journal of Asian Earth Sciences*, *105*, 223-233.

Turcotte, D., & Schubert, G. (2014). Geodynamics.

Valla, P. G., Sternai, P., & Fox, M. (2021). How climate, uplift and erosion shaped the Alpine topography. *Elements: An International Magazine of Mineralogy, Geochemistry, and Petrology*, *17*(1), 41-46.

Vogt, K., Matenco, L., & Cloetingh, S. (2017). Crustal mechanics control the geometry of mountain belts. Insights from numerical modelling. *Earth and Planetary Science Letters*, *460*, 12-21. https://doi.org/https://doi.org/10.1016/j.epsl.2016.11.016

Vogt, K., Willingshofer, E., Matenco, L., Sokoutis, D., Gerya, T., & Cloetingh, S. (2018). The role of lateral strength contrasts in orogenesis: A 2D numerical study. *Tectonophysics*, *746*, 549-561.

Wang, P., Scherler, D., Liu-Zeng, J., Mey, J., Avouac, J.-P., Zhang, Y., & Shi, D. (2014). Tectonic control of Yarlung Tsangpo Gorge revealed by a buried canyon in Southern Tibet. *Science*, *346*(6212), 978-981.

Whipp Jr, D. M., Beaumont, C., & Braun, J. (2014). Feeding the "aneurysm": Orogen‐parallel mass transport into Nanga Parbat and the western Himalayan syntaxis. *Journal of Geophysical Research: Solid Earth*, *119*(6), 5077-5096.

Whipple, K. X. (2009). The influence of climate on the tectonic evolution of mountain belts. *Nature geoscience*, *2*(2), 97-104.

Whipple, K. X. (2014). Can erosion drive tectonics? *Science*, *346*(6212), 918-919.

Whipple, K. X., & Meade, B. J. (2004). Controls on the strength of coupling among climate, erosion, and deformation in two‐sided, frictional orogenic wedges at steady state. *Journal of Geophysical Research: Earth Surface*, *109*(F1).

Whipple, K. X., & Meade, B. J. (2006). Orogen response to changes in climatic and tectonic forcing. *Earth and Planetary Science Letters*, *243*(1-2), 218-228.

Whipple, K. X., & Tucker, G. E. (1999). Dynamics of the stream‐power river incision model: Implications for height limits of mountain ranges, landscape response timescales, and research needs. *Journal of Geophysical Research: Solid Earth*, *104*(B8), 17661-17674.

Willett, S. D. (1999). Orogeny and orography: The effects of erosion on the structure of mountain belts. *Journal of Geophysical Research: Solid Earth*, *104*(B12), 28957-28981.

Willett, S. D. (2006). *Tectonics, climate, and landscape evolution* (Vol. 398). Geological Society of America.

Willett, S. D., & Brandon, M. T. (2002). On steady states in mountain belts. *Geology*, *30*(2), 175-178.

Willett, S. D., Schlunegger, F., & Picotti, V. (2006). Messinian climate change and erosional destruction of the central European Alps. *Geology*, *34*(8), 613-616.

Wolf, S. G., Huismans, R. S., Braun, J., & Yuan, X. (2022). Topography of mountain belts controlled by rheology and surface processes. *Nature*, 1-6.

Wratt, D., Revell, M., Sinclair, M., Gray, W., Henderson, R., & Chater, A. (2000). Relationships between air mass properties and mesoscale rainfall in New Zealand's Southern Alps. *Atmospheric Research*, *52*(4), 261-282.

Xiangjiang, W. F. J. J. Y., & Dalai, T. J. Z. (2017). Quantitative research on temporal and spatial coupling of precipitation potential energy and erosion intensity in Himalayas. *Chinese Journal of Geology*, *52*(1), 1-14.

Yang, J., Cao, W., Yuan, X., & Yang, J. (2023). Erosion-Driven Isostatic Flow and Crustal Diapirism: Analytical and Numerical Models With Implications for the Evolution of the Eastern Himalayan Syntaxis, Southern Tibet. *Tectonics*, *42*(8), e2022TC007717. https://doi.org/https://doi.org/10.1029/2022TC007717

Yang, R., Herman, F., Fellin, M. G., & Maden, C. (2018). Exhumation and topographic evolution of the Namche Barwa Syntaxis, eastern Himalaya. *Tectonophysics*, *722*, 43-52.

Yao, T., Li, Z., Yang, W., Guo, X., Zhu, L., Kang, S., . . . Yu, W. (2010). Glacial distribution and mass balance in the Yarlung Zangbo River and its influence on lakes. *Chinese Science Bulletin*, *55*(20), 2072-2078.

Ye, Y., Wu, L., Cowgill, E., Tian, Y., Lin, X., Xiao, A., & Chen, H. (2022). Long-lagged (~ 19 Myr) response of accelerated river incision to rock uplift on the northern margin of the Tibetan Plateau. *Earth and Planetary Science Letters*, *591*, 117608.

Yin, A. (2006). Cenozoic tectonic evolution of the Himalayan orogen as constrained by along-strike variation of structural geometry, exhumation history, and foreland sedimentation. *Earth-Science Reviews*, *76*(1-2), 1-131.

Yu, X., Ji, J., Gong, J., Sun, D., Qing, J., Wang, L., . . . Zhang, Z. (2011). Evidences of rapid erosion driven by climate in the Yarlung Zangbo (Tsangpo) Great Canyon, the eastern Himalayan syntaxis. *Chinese Science Bulletin*, *56*(11), 1123-1130. https://doi.org/10.1007/s11434-011-4419-x

Yu, X., Ji, J., Wang, F., & Zhong, D. (2017). Intensified climate-driven exhumation along the South Himalayan Front since one million years ago. *Journal of Asian Earth Sciences*, *136*, 50-57.

Yuan, X. P., Braun, J., Guerit, L., Rouby, D., & Cordonnier, G. (2019). A New Efficient Method to Solve the Stream Power Law Model Taking Into Account Sediment Deposition. *Journal of Geophysical Research: Earth Surface*, *124*(6), 1346-1365. https://doi.org/https://doi.org/10.1029/2018JF004867

Zeitler, P. K., Koons, P. O., Bishop, M. P., Chamberlain, C. P., Craw, D., Edwards, M. A., . . . Khattak, M. U. K. (2001). Crustal reworking at Nanga Parbat, Pakistan: Metamorphic consequences of thermal‐mechanical coupling facilitated by erosion. *Tectonics*, *20*(5), 712-728.

Zeitler, P. K., Meltzer, A. S., Brown, L., Kidd, W. S., Lim, C., & Enkelmann, E. (2014). Tectonics and topographic evolution of Namche Barwa and the easternmost Lhasa block, Tibet. In *Toward an improved understanding of uplift mechanisms and the elevation history of the Tibetan Plateau* (Vol. 507, pp. 23-58). Geological Society of America Special Papers.

Zeitler, P. K., Meltzer, A. S., Koons, P. O., Craw, D., Hallet, B., Chamberlain, C. P., . . . Bishop, M. (2001). Erosion, Himalayan geodynamics, and the geomorphology of metamorphism. *GSA Today*, *11*(1), 4-9.

Zhang, H., Hou, Z., Rolland, Y., & Santosh, M. (2022). The cold and hot collisional orogens: Thermal regimes and metallogeny of the Alpine versus Himalayan-Tibetan belts. *Ore Geology Reviews*, *141*, 104671.

Zhang, J., Ji, J., Zhong, D., Ding, L., & He, S. (2004). Structural pattern of eastern Himalayan syntaxis in Namjagbarwa and its formation process. *Science in China Series D: Earth Sciences*, *47*(2), 138-150.

Zhang, Z., Zhao, G., Santosh, M., Wang, J., Dong, X., & Liou, J. (2010). Two stages of granulite facies metamorphism in the eastern Himalayan syntaxis, south Tibet: Petrology, zircon geochronology and implications for the subduction of Neo‐Tethys and the Indian continent beneath Asia. *Journal of Metamorphic Geology*, *28*(7), 719-733.

Zhisheng, A., Kutzbach, J. E., Prell, W. L., & Porter, S. C. (2001). Evolution of Asian monsoons and phased uplift of the Himalaya–Tibetan plateau since Late Miocene times. *Nature*, *411*(6833), 62-66.

References From the Supporting Information

Anders, A. M., Roe, G. H., Hallet, B., Montgomery, D. R., Finnegan, N. J., & Putkonen, J. (2006). Spatial patterns of precipitation and topography in the Himalaya. *Special Papers-Geological Society of America*, *398*, 39.

Bittner, D., & Schmeling, H. (1995). Numerical Modelling of Melting Processes and Induced Diapirism In the Lower Crust. *Geophysical Journal International*, *123*(1), 59-70. https://doi.org/10.1111/j.1365-246X.1995.tb06661.x

Bookhagen, B., & Burbank, D. W. (2006). Topography, relief, and TRMM‐derived rainfall variations along the Himalaya. *Geophysical Research Letters*, *33*(8).

Burg, J.-P., & Gerya, T. V. (2005). The role of viscous heating in Barrovian metamorphism of collisional orogens: thermomechanical models and application to the Lepontine Dome in the Central Alps. *Journal of Metamorphic Geology*, *23*(2), 75-95. https://doi.org/https://doi.org/10.1111/j.1525-1314.2005.00563.x

Clauser, C., & Huenges, E. (1995). Thermal conductivity of rocks and minerals. *Rock physics and phase relations: a handbook of physical constants*, *3*, 105-126.

Gerya, T. (2019). *Introduction to numerical geodynamic modelling*. Cambridge University Press.

Gerya, T. V., & Yuen, D. A. (2003). Rayleigh–Taylor instabilities from hydration and melting propel 'cold plumes' at subduction zones. *Earth and Planetary Science Letters*, *212*(1), 47-62. https://doi.org/https://doi.org/10.1016/S0012-821X(03)00265-6

Pinkerton, H., & Stevenson, R. J. (1992). Methods of determining the rheological properties of magmas at sub-liquidus temperatures. *Journal of Volcanology and Geothermal Research*, *53*(1), 47-66. https://doi.org/https://doi.org/10.1016/0377-0273(92)90073-M

Ranalli, G. (1995). *Rheology of the Earth*. Springer Science & Business Media.

Schmidt, M. W., & Poli, S. (1998). Experimentally based water budgets for dehydrating slabs and consequences for arc magma generation. *Earth and Planetary Science Letters*, *163*(1), 361-379. https://doi.org/https://doi.org/10.1016/S0012-821X(98)00142-3

Turcotte, D., & Schubert, G. (2014). Geodynamics.

Journal of Geophysical Research: Solid Earth

Supporting Information for

Numerical Modelling of Coupled Climate, Tectonics and Surface Processes on the Eastern Himalayan Syntaxis

Xueyun Lu[1], Jingtao Lai[2], Lining Wang[3,4], Jianqing Ji[1], Dalai Zhong[5]

[1]Key Laboratory of Orogenic Belts and Crustal Evolution, School of Earth and Space Sciences, Peking University, Beijing 100871, China

[2]Earth Surface Process Modelling, GFZ German Research Centre for Geosciences, 14473 Potsdam, Germany

[3]Research Institute of Petroleum Exploration & Development, PetroChina, Beijing 100083, China

[4]Key Laboratory of Basin Structure & Hydrocarbon Accumulation, CNPC, Beijing 100083, China

[5]Institute of Geology and Geophysics, Chinese Academy of Sciences, Beijing 100029, China

Contents of this file

Introduction

This supporting information provides supplemental Texts S1 and S2 describing the visco-elasto-plastic rheology of rocks and the partial melting model included in our thermomechanical model, respectively. Text S3 presents the details regarding the selection of parameters α_P and β_P in the orographic precipitation model (Equation (9) in the main text). Supplemental Figure S1 shows the testing results of the sensitivity of predicted precipitation to the parameters α_P and β_P based on the orographic precipitation model. Supplemental Table S1 presents the material properties used in the numerical experiments. Tables S2 to S4 are numerical experiment summaries in this study.

Text S1. Visco-elasto-plastic rheology

The deformation behavior of rocks in this study is considered visco-elasto-plastic, and the bulk deviatoric strain rate $\dot{\varepsilon}'_{ij}$ can be decomposed into three respective components:

$$\dot{\varepsilon}'_{ij} = \dot{\varepsilon}'_{ij(viscous)} + \dot{\varepsilon}'_{ij(elastic)} + \dot{\varepsilon}'_{ij(plastic)} \quad (1)$$

while

$$\dot{\varepsilon}'_{ij(viscous)} = \frac{1}{2\eta_{cr}}\sigma'_{ij} \quad (2)$$

$$\dot{\varepsilon}'_{ij(elastic)} = \frac{1}{2\mu}\frac{\widehat{D}\sigma'_{ij}}{Dt} \quad (3)$$

$$\dot{\varepsilon}'_{ij(plastic)} = 0\ for\ \sigma_{\mathrm{II}} < \sigma_{yield} \quad (4)$$

$$\dot{\varepsilon}'_{ij(plastic)} = \chi\frac{\partial G_{plastic}}{\partial\sigma'_{ij}} = \chi\frac{\sigma'_{ij}}{2\sigma_{\mathrm{II}}}\ for\ \sigma_{\mathrm{II}} = \sigma_{yield} \quad (5)$$

where μ is the shear modulus, $\frac{\widehat{D}\sigma'_{ij}}{Dt}$ is the objective co-rotational time derivative of the deviatoric stress component σ'_{ij}, $G_{plastic}$ is the plastic flow potential, σ_{yield} is the plastic yield strength for a given rock, $\sigma_{\mathrm{II}} = \sqrt{\frac{1}{2}\sigma'^{2}_{ij}}$ is the second invariant of the deviatoric stress tensor, χ is the plastic multiplier, η_{cr} is the viscosity for viscous creep of rocks (ductile flow), and it depends on temperature, pressure and strain rate(Ranalli, 1995):

$$\eta_{cr} = \frac{\dot{\varepsilon}_{\mathrm{II}}^{(1-n)/n}}{A_D^{1/n}} e^{\frac{E_a+PV_a}{nRT}} \quad (6)$$

where $\dot{\varepsilon}_{\mathrm{II}} = \sqrt{\frac{1}{2}\dot{\varepsilon}_{ij}^{2}}$ is the second invariant of the strain rate tensor, A_D, n, E_a and V_a are experimentally determined flow law parameters, which represent material constant, stress exponent, activation energy and activation volume, respectively. R is the gas constant.

The plasticity is implemented using the following yield criterion (Gerya, 2019):

$$\sigma_{yield} = \sigma_c + \gamma_{int}P \quad (7)$$

It is assumed that the local plastic strength of rocks depends on the dynamic pressure (P). σ_c is the compressive strength, and its relationship with the material cohesion(c) is given by $\sigma_c = c\cos(\varphi)$. Here φ is the angle of internal friction. $\gamma_{int} = \sin(\varphi)$ is the internal friction coefficient.

Text S2. Partial melting

The thermomechanical model accounts for partial melting of the various lithologies by using experimentally obtained P-T dependent wet solidus and dry liquidus curves. In this simple partial melting model, the volumetric fraction of melt M at a certain pressure is assumed to increase linearly with temperature according to the relations (Burg & Gerya, 2005; Gerya & Yuen, 2003):

$$M = 0\ at\ T \le T_{solidus}$$

$$M = \frac{(T - T_{solidus})}{(T_{liquidus} - T_{solidus})}\ at\ T_{liquidus} < T < T_{solidus} \quad (8)$$

$$M = 1\ at\ T \ge T_{liquidus}$$

where $T_{solidus}$ and $T_{liquidus}$ are the wet solidus and dry liquidus temperatures of the considered rock, respectively. For the rocks with partial melt fraction M greater than 0.1, their effective viscosity η_e is calculated according to the following formula (Bittner & Schmeling, 1995; Pinkerton & Stevenson, 1992):

$$\eta_e = \eta_0 exp\left[2.5 + (1 - M)\left(\frac{1 - M}{M}\right)^{0.48}\right] \quad (9)$$

here η_0 is an empirical parameter depending on rock types. For partially molten mafic rocks, it can be set to $10^{13}\ Pa\ s$ (i.e.,$1 \times 10^{14} \leq \eta_e \leq 2 \times 10^{15}\ Pa\ s\ for\ 0.1 \leq M \leq 1$), and for felsic rocks, $\eta_0 = 5 \times 10^{14}\ Pa\ s$(i.e.,$6 \times 10^{15} \leq \eta_e \leq 8 \times 10^{16}\ Pa\ s\ for\ 0.1 \leq M \leq 1$) can be adopted (Bittner & Schmeling, 1995).

For the partially molten rocks, their effective density (ρ_e) is then calculated from:

$$\rho_e = \rho_{solid}\left(1 - M + M\frac{\rho_{0(molten)}}{\rho_{0(solid)}}\right) \quad (10)$$

where $\rho_{0(solid)}$ and $\rho_{0(molten)}$ are the standard densities of solid and molten rock, respectively. ρ_{solid} is the density of solid rocks at given pressure (P) and temperature (T), and it's computed as:

$$\rho_{solid} = \rho_r[1 + \beta(P - P_r)] \times [1 - \alpha(T - T_r)] \quad (11)$$

where α is thermal expansion, β is compressibility, ρ_r is the density of a specific material at reference pressure P_r (typically $10^5\ Pa$) and temperature T_r (273 K).

The effect of latent heating due to equilibrium melting/crystallization are accounted for by increasing the effective heat capacity($C_{P(eff)}$) and the thermal expansion(α_{eff}) of partially melting/crystallization rocks($0 < M < 1$), calculated as (Burg & Gerya, 2005):

$$C_{P(eff)} = C_p + Q_L\left(\frac{\partial M}{\partial T}\right)_{P=const} \quad (12)$$

$$\alpha_{eff} = \alpha + \rho\frac{Q_L}{T}\left(\frac{\partial M}{\partial P}\right)_{T=const} \quad (13)$$

where C_p is the heat capacity of the solid rock and Q_L is the latent heat of melting of the rock.

Text S3. The selection of parameters α_P and β_P

To gain better insight into and select reasonable values for the parameters α_P and β_P, we firstly tested the sensitivity of predicted precipitation to the parameters α_P and β_P based on Equation (9) in the main text (Figure S1). From the testing results, it can be observed that this model (Equation (9) in the main text) is capable to capture the primary characteristics of the pattern of orographic precipitation, especially the local precipitation enhancement on the windward side and the rain shadow on the leeward side. However, it tends to overestimate the precipitation in the inland areas on the right side (leeward side) of the mountain ranges. This is largely due to the fact that in this model, the distinction between the windward and leeward sides is determined solely by the sign of the topographic slope. However, for most cases of simulating convergent plate boundary settings, the areas on both sides of the convergence center are usually vast plains where the erosional potential approaches zero. Therefore, the impact on erosion patterns due to this deficiency could not be significant. For a specific terrain topography, when keeping β_P fixed and gradually increasing α_P, the overall predicted precipitation increases, but the spatial pattern of precipitation remains relatively stable (Figure S1a). When keeping α_P fixed and gradually increasing β_P, the model predicts an enhanced localization of precipitation on the windward side, but the average precipitation intensity over a large area remains relatively stable (Figure S1b). However, regardless of the values of α_P and β_P, the location with the maximum precipitation on the windward side remains unchanged. Therefore, the parameter β_P reflects the sensitivity of precipitation to changes in elevation and slope, while α_P is related to the average precipitation on a large scale. If we assume that the average precipitation over the low-lying plains in front of the mountain ranges (with near-zero elevation and slope) is P_0 , which can also represent the average precipitation on a large scale (or over the entire model domain), then

$$\alpha_P = \frac{P_0}{e_{sat}(T_0)} \quad (14)$$

where $e_{sat}(T_0)$ is the saturation vapor pressure at sea level. Thus, Equation (9) in the main text can be rewritten as

$$P = \left(\frac{P_0}{e_{sat}(T_0)} + \beta_P S\right) e_{sat}(T) \quad (15)$$

In the eastern Himalayan syntaxis, Anders et al. (2006) obtained the values of α_P and β_P through regression analysis, which are approximately 0.014 and 0.216, respectively. These set of values produced prediction that successfully captures the main characteristics of the current precipitation in the eastern Himalayan syntaxis, but failed to predict the maximum precipitation totals (the predicted value $P_{\max\_pred} = 3.5\ m/yr$, and the actual value $P_{\max\_actu} = 6\ m/yr$). To address this limitation, let's assume that the pattern of precipitation in the eastern Himalayan syntaxis strictly follows the model described in Equation (9) in the main text. We also assume the existence of true α_P and β_P in the syntaxis. The parameter values estimated by Anders et al. (2006) are denoted as $\alpha_P{}'$ and $\beta_P{}'$. Furthermore, let's consider that at the location where the maximum precipitation happens, the elevation, the topographic slope and the corresponding saturation vapor pressure are h_1, S_1, and $e_{sat}(h_1)$, respectively, then

$$P_{\max\_actu} = \alpha_P e_{sat}(h_1) + \beta_P S_1 e_{sat}(h_1) \quad (16)$$

Based on the above discussion, for a specific topography, the location with maximum precipitation remains relatively stable. Therefore, we have

$$P_{\max\_pred} = \alpha_P{}' e_{sat}(h_1) + \beta_P{}' S_1 e_{sat}(h_1) \quad (17)$$

Assuming $k_0 = P_{\max\_actu}/P_{\max\_pred}$, by combining equations (16) and (17), we obtain $\alpha_P = k_0\alpha_P{}' = 0.024$ and $\beta_P = k_0\beta_P{}' = 0.370$. Here, $\alpha_P = 0.024$ corresponds to precipitation of 1.019 m/yr in the low-lying plain in front of the mountain range (P_0). This predicted value is closer to the actual value in the eastern Himalayan syntaxis region compared to the estimated value of 0.594 m/yr using $\alpha_P = 0.014$ (Anders et al., 2006; Bookhagen & Burbank, 2006), indicating that such a correction is reasonable.

In this study, α_P is calculated based on various given average precipitation P_0 and Equation (14), while β_P is set to 0.370. The variation in the average precipitation intensity across the entire mountain range is achieved by adjusting the value of P_0.

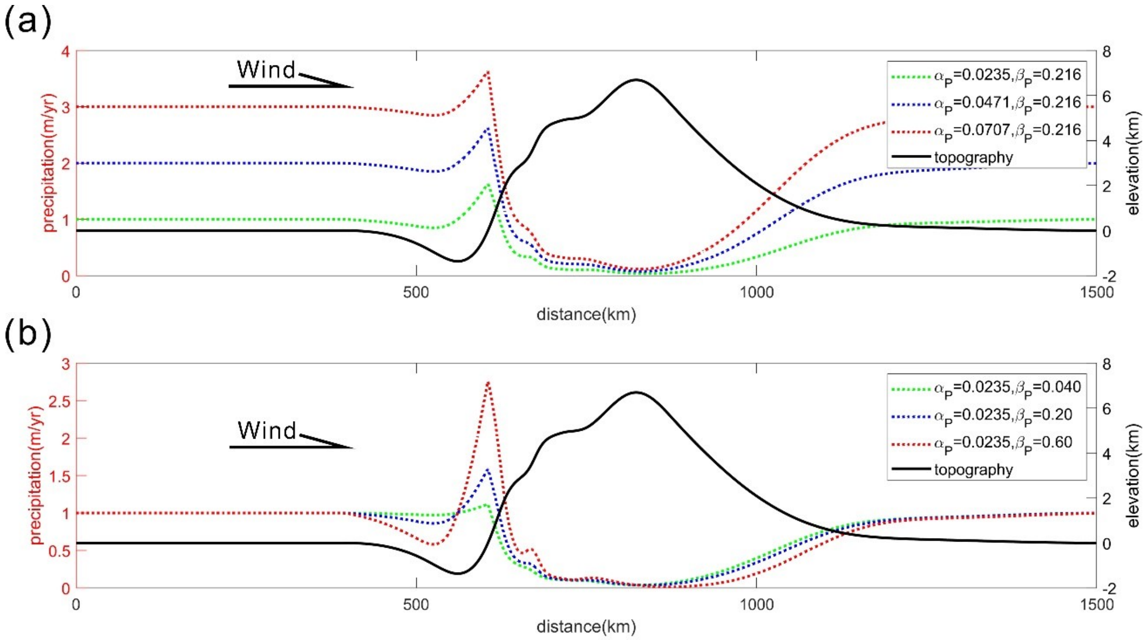

Figure S1. Sensitivity of predicted precipitation to the parameters α_P and β_P based on Equation (9) in the main text. (a) shows the predicted precipitation with fixed β_P and varying α_P, while (b) shows the predicted precipitation with fixed α_P and varying β_P. The solid black line represents the topography of an assumed mountain range, while the dashed green, blue, and red lines represent the predicted precipitation based on the topography and the orographic precipitation model as described in Equation (9) in the main text. It's assumed that the moisture-laden winds arrive from the left in both (a) and (b).

Table S1. Material properties used in the numerical experiments.

Properties	Sediments	Normal rock sequence	Decollement layer	Backstop
Flow law	Wet quartzite	Wet quartzite	Wet quartzite	quartzite
A_D(MPa^{-n} s^{-1})	3.2×10^{-4}	3.2×10^{-4}	3.2×10^{-4}	6.7×10^{-6}
n	2.3	2.3	2.3	2.4
Ea(kJ mol^{-1})	154	154	154	156
Va(cm^3)	0	0	0	0
$\rho_{0\ (solid)}$ (kg m^{-3})	2700	2700	2700	2700
$\rho_{0\ (molten)}$ (kg m^{-3})	2400	2400	2400	2400
σ_c(Pa)	$1\times10^{7-6}$	$1\times10^{7-6}$	$1\times10^{5-4}$	$1\times10^{7-6}$
γ_{int}	0.20-0.10	0.30-0.15	0.10-0.05	0.40-0.20
μ(GPa)	10	10	10	10
k(W $m^{-1}K^{-1}$, at T_K)	0.64+807/(T+77)	0.64+807/(T+77)	0.64+807/(T+77)	0.64+807/(T+77)

$T_{solidus}$(K, at P_{MPa})	889+17900/(P+54)+ 20200/(P+54)^2 at P<1200 MPa, 831+0.06P at P>1200 MPa	889+17900/(P+54)+ 20200/(P+54)^2 at P<1200 MPa, 831+0.06P at P>1200 MPa	889+17900/(P+54)+ 20200/(P+54)^2 at P<1200 MPa, 831+0.06P at P>1200 MPa	889+17900/(P+54)+ 20200/(P+54)^2 at P<1200 MPa, 831+0.06P at P>1200 MPa
$T_{liquidus}$(K, at P_{MPa})	1262+0.09P	1262+0.09P	1262+0.09P	1262+0.09P
Q_L(kJ kg^{-1})	300	300	300	300
H_r(μWm^{-3})	2.0	2.0	2.0	2.0
C_p(J kg^{-1}K^{-1})	1000	1000	1000	1000
α(K^{-1})	3×10^{-5}	3×10^{-5}	3×10^{-5}	3×10^{-5}
β(Pa^{-1})	1×10^{-11}	1×10^{-11}	1×10^{-11}	1×10^{-11}

Note. A_D, n, E_a and V_a are the flow law parameters, corresponding to material constant, stress exponent, activation energy, and activation volume, respectively (Ranalli, 1995). $\rho_{0(solid)}$ and $\rho_{0(molten)}$ are the standard densities of solid and molten rock, respectively. Strain weakening is applied within a plastic strain interval of 0–1, at which the compressive strength(σ_c) and internal friction coefficient(γ_{int}) decrease gradually. Q_L and H_r are the latent and radioactive heat production, respectively, μ is the shear modulus (Bittner & Schmeling, 1995; Turcotte & Schubert, 2014), k is thermal conductivity (Clauser & Huenges, 1995), $T_{solidus}$ and $T_{liquidus}$ are the wet solidus and dry liquidus temperatures of the considered rock, respectively (Schmidt & Poli, 1998), C_p is isobaric heat capacity, α is thermal expansion, β is compressibility.

Table S2. Numerical experiment summary with an initial geothermal gradient of 30 ℃/km.

Convergence rate (cm/yr) / Average precipitation (m/yr)	0.5	1.0	1.5	2.0	2.5	3.0	3.5	4.0	4.5	5.0
0	S001	S002	S003	S004	S005	S006	S007	S008	S009	S010
2	S011	S012	S013	S014	S015	S016	S017	S018	S019	S020
4	S021	S022	S023	S024	S025	S026	S027	S028	S029	S030
6	S031	S032	S033	S034	S035	S036	S037	S038	S039	S040
8	S041	S042	S043	S044	S045	S046	S047	S048	S049	S050
10	S051	S052	S053	S054	S055	S056	S057	S058	S059	S060
12	S061	S062	S063	S064	S065	S066	S067	S068	S069	S070
14	S071	S072	S073	S074	S075	S076	S077	S078	S079	S080
16	S081	S082	S083	S084	S085	S086	S087	S088	S089	S090
18	S091	S092	S093	S094	S095	S096	S097	S098	S099	S100
20	S101	S102	S103	S104	S105	S106	S107	S108	S109	S110

Table S3. Numerical experiment summary with an initial geothermal gradient of 25 ℃ /km.

Average precipitation (m/yr) \ Convergence rate (cm/yr)	0.5	1.0	1.5	2.0	2.5	3.0	3.5	4.0	4.5	5.0
0	S111	S112	S113	S114	S115	S116	S117	S118	S119	S120
2	S121	S122	S123	S124	S125	S126	S127	S128	S129	S130
4	S131	S132	S133	S134	S135	S136	S137	S138	S139	S140
6	S141	S142	S143	S144	S145	S146	S147	S148	S149	S150
8	S151	S152	S153	S154	S155	S156	S157	S158	S159	S160
10	S161	S162	S163	S164	S165	S166	S167	S168	S169	S170
12	S171	S172	S173	S174	S175	S176	S177	S178	S179	S180
14	S181	S182	S183	S184	S185	S186	S187	S188	S189	S190
16	S191	S192	S193	S194	S195	S196	S197	S198	S199	S200
18	S201	S202	S203	S204	S205	S206	S207	S208	S209	S210
20	S211	S212	S213	S214	S215	S216	S217	S218	S219	S220

Table S4. Additional numerical experiments with a convergence rate of 2 cm/yr.

Average precipitation (m/yr) \ Initial geothermal gradient(°C/km)	10	15	20	35	40	45
2	ST01	ST02	ST03	ST04	ST05	ST06
6	ST07	ST08	ST09	ST10	ST11	ST12

References

Anders, A. M., Roe, G. H., Hallet, B., Montgomery, D. R., Finnegan, N. J., & Putkonen, J. (2006). Spatial patterns of precipitation and topography in the Himalaya. *Special Papers-Geological Society of America*, *398*, 39.

Bittner, D., & Schmeling, H. (1995). Numerical Modelling of Melting Processes and Induced Diapirism In the Lower Crust. *Geophysical Journal International*, *123*(1), 59-70. https://doi.org/10.1111/j.1365-246X.1995.tb06661.x

Bookhagen, B., & Burbank, D. W. (2006). Topography, relief, and TRMM‐derived rainfall variations along the Himalaya. *Geophysical Research Letters*, *33*(8).

Burg, J.-P., & Gerya, T. V. (2005). The role of viscous heating in Barrovian metamorphism of collisional orogens: thermomechanical models and application to the Lepontine Dome in the Central Alps. *Journal of Metamorphic Geology*, *23*(2), 75-95. https://doi.org/https://doi.org/10.1111/j.1525-1314.2005.00563.x

Clauser, C., & Huenges, E. (1995). Thermal conductivity of rocks and minerals. *Rock physics and phase relations: a handbook of physical constants*, *3*, 105-126.
Gerya, T. (2019). *Introduction to numerical geodynamic modelling*. Cambridge University Press.
Gerya, T. V., & Yuen, D. A. (2003). Rayleigh–Taylor instabilities from hydration and melting propel 'cold plumes' at subduction zones. *Earth and Planetary Science Letters*, *212*(1), 47-62. https://doi.org/https://doi.org/10.1016/S0012-821X(03)00265-6
Pinkerton, H., & Stevenson, R. J. (1992). Methods of determining the rheological properties of magmas at sub-liquidus temperatures. *Journal of Volcanology and Geothermal Research*, *53*(1), 47-66. https://doi.org/https://doi.org/10.1016/0377-0273(92)90073-M
Ranalli, G. (1995). *Rheology of the Earth*. Springer Science & Business Media.
Schmidt, M. W., & Poli, S. (1998). Experimentally based water budgets for dehydrating slabs and consequences for arc magma generation. *Earth and Planetary Science Letters*, *163*(1), 361-379. https://doi.org/https://doi.org/10.1016/S0012-821X(98)00142-3
Turcotte, D., & Schubert, G. (2014). Geodynamics.